



Virginia Commonwealth University  
VCU Scholars Compass

---

Theses and Dissertations

Graduate School


---

2019

## Engineering of Earth-Abundant Electrochemical Catalysts

Dylan D. Rodene  
*Virginia Commonwealth University*

Follow this and additional works at: <https://scholarscompass.vcu.edu/etd>

 Part of the [Catalysis and Reaction Engineering Commons](#), and the [Other Engineering Science and Materials Commons](#)

© The Author

---

Downloaded from

<https://scholarscompass.vcu.edu/etd/6106>

This Dissertation is brought to you for free and open access by the Graduate School at VCU Scholars Compass. It has been accepted for inclusion in Theses and Dissertations by an authorized administrator of VCU Scholars Compass. For more information, please contact [libcompass@vcu.edu](mailto:libcompass@vcu.edu).

© Dylan D. Rodene 2019

All Rights Reserved

# **Engineering of Earth-Abundant Electrochemical Catalysts**

A dissertation submitted in partial fulfillment of the requirements for  
the degree of Doctor of Philosophy at Virginia Commonwealth University.

By

Dylan D. Rodene

Bachelor of Science in Chemical & Life Sciences Engineering, Virginia Commonwealth  
University, 2014

Advisor: Dr. Ram B. Gupta

Associate Dean for Faculty Research Development | Professor of Chemical & Life Science  
Engineering, Department of Chemical & Life Science Engineering

Virginia Commonwealth University  
Richmond, Virginia

December 2019

## Acknowledgements

The completion of any research for my dissertation would not have been possible without numerous contributions from my colleagues and mentors. I would like to thank all of them for their involvement throughout each stage of my research.

I would like to express my sincere gratitude to my research advisor, Dr. Ram B. Gupta, for his continuous support of my Ph. D. study and research. Without his guidance and interest in research field's specific to my interests, I would not be setup with a skillset to pursuit a career path of my choosing. I would like to extend a special thank you to Dr. Indika U. Arachchige, who pushed me beyond what was expected, and in the process, he has taught me how to form scientific research plans and vastly improve my scientific writing. I would like to thank Dr. Christina Tang for encouragement, moral support, and insightful comments whenever I needed them. I would like to thank Dr. Thomas Roper for allowing us to study a project together for a research plan that I proposed. I would like to thank Dr. Umit Ozgur for the few interaction we have had and for use of his Xe light source, even if I do not use it often, I show it off regularly to visiting guests.

I would like to thank my fellow peers of science that I have become friends with: Dr. Emmanuel Nyankson, Dr. Sushil K. Saraswat, Miss Ebtesam H. Eladgham, Mr. Matthew Glace, Dr. Jo-Ann Jee, Dr. Narendar Gade, Dr. Muslum Demir, and Dr. Memhet Gonen, Ms. Jethrine Mugumya, and Ms. Katelyn Shell. I would like to thank Dr. Hani El-Kaderi and his students: Ahmed A. Abdelkader, Ahmed Alzharani, Shamara K. Weeraratne, and Nazgol Norouzi, for their shared time and work with lithium half cells. I would also like to thank everyone in the Chemistry and Chemical Engineering laboratories that I have interacted with regularly throughout my Ph.D. career. There are also a few special people that I would like to give extra thanks too: Mr. Jamison T. Lancaster, Dr. Qiang Yan and Dr. Justine L. Drobitch, thank you for your support throughout my

Ph.D. career. Lastly, I would like to thank my parents, Julie and Ken Bitner, for raising me in such a way to help bring out my greatest potential. Thank you to any and all who have ever helped me along the way, I have not forgotten you. If you are ever in need, I will gladly help in any way I can.

## Table of Contents

|  |      |
|--|------|
| Acknowledgements.....  | iii  |
| List of Figures.....   | viii |
| Abstract.....  | xii  |
| Chapter I. Introduction of Electrocatalysis.....   | 1    |
| 1.1 Introduction of Electrocatalysis.....  | 2    |
| 1.2 Fundamentals of Electrocatalysis for Water Splitting.....  | 4    |
| 1.3 Fundamentals of Photocatalysis and Photoelectrodes.....  | 8    |
| 1.4 Recent Advancements in Semiconductor Materials for Photoelectrochemical Water Splitting for Hydrogen Production Using Visible Light.....                             | 12   |
| 1.5 Photo-remediation Application – Advancements in Crude Oil Spill Remediation Research after the Deepwater Horizon Oil Spill.....                                      | 15   |
| 1.6 Dissertation Objectives and Arrangement.....   | 17   |
| Chapter II. Water Splitting Electrochemical Techniques.....  | 20   |
| 2.1 Water Splitting – Experimental Techniques.....   | 21   |
| 2.1.1 Experimental Startup Procedure.....  | 26   |
| 2.1.2 Data Analysis.....   | 28   |
| 2.1.3 GAMRY FRAMEWORK.....   | 35   |
| 2.2 Material Characterization.....   | 35   |
| Chapter III. Reduction of Water – Crystal Structure and Composition-Dependent Electrocatalytic Activity of Ni-Mo Nanoalloys for Water Splitting to Produce Hydrogen..... | 38   |
| 3.1 INTRODUCTION.....  | 39   |
| 3.2 EXPERIMENTAL SECTION.....  | 42   |
| 3.2.1 Materials.....   | 42   |
| 3.2.2 Synthesis of Cubic Ni <sub>1-x</sub> Mo <sub>x</sub> Alloy NPs.....  | 42   |
| 3.2.3 Synthesis of Hexagonal Ni <sub>1-x</sub> Mo <sub>x</sub> Alloy NPs.....  | 43   |
| 3.2.4 Isolation and Purification of NPs.....   | 44   |
| 3.2.5 Physical Characterization.....   | 45   |
| 3.2.6 Fabrication of Working Electrodes.....   | 46   |
| 3.2.7 Electrochemical Measurements.....  | 47   |
| 3.3 RESULTS AND DISCUSSION.....  | 48   |

|   |     |
|---|-----|
| 3.3.1 Synthesis of Ni <sub>1-x</sub> Mo <sub>x</sub> alloy NPs .....  | 48  |
| 3.3.2 Electrocatalytic activity of Ni <sub>1-x</sub> Mo <sub>x</sub> alloy NPs for HER.....   | 64  |
| 3.4 Conclusion .....  | 74  |
| Chapter IV. Reduction of Water – Stable and Efficient Electrocatalytic Hydrogen Production<br>Cathodes: Phase, Morphology, and Composition Dependent NiMoP.....                                       | 76  |
| 4.1 INTRODUCTION .....  | 77  |
| 4.2 EXPERIMENTAL SECTION .....  | 79  |
| 4.2.1 Materials. ....   | 79  |
| 4.2.2 Synthesis of Spherical Ni <sub>2-x</sub> Mo <sub>x</sub> P and Ni <sub>12-x</sub> Mo <sub>x</sub> P <sub>5</sub> Alloy NPs. ....  | 80  |
| 4.2.3 Synthesis of Hetero-Structured Ni <sub>2-x</sub> Mo <sub>x</sub> P and Ni <sub>12-x</sub> Mo <sub>x</sub> P <sub>5</sub> Alloy NPs. ....  | 80  |
| 4.2.4 Synthesis of Hollow Ni <sub>2-x</sub> Mo <sub>x</sub> P and Ni <sub>12-x</sub> Mo <sub>x</sub> P <sub>5</sub> Alloy NPs. ....   | 81  |
| 4.2.5 Isolation and Purification of NPs. ....   | 82  |
| 4.2.6 Physical Characterization.....  | 82  |
| 4.2.7 Preparation of Working Electrodes.....  | 83  |
| 4.2.8 Electrochemical Measurements. ....  | 83  |
| 4.3 RESULTS AND DISCUSSION .....  | 84  |
| 4.3.1 Synthesis of Ni <sub>2-x</sub> Mo <sub>x</sub> P and Ni <sub>12-x</sub> Mo <sub>x</sub> P <sub>5</sub> alloy NPs .....  | 84  |
| 4.3.2 Electrocatalytic activity of Ni–Mo–P alloy NPs for HER.....   | 86  |
| 4.4 CONCLUSIONS.....  | 93  |
| Chapter V. Conclusions and Future Directions .....  | 94  |
| 5.1 DISSERTATION CONCLUSION .....   | 95  |
| 5.2 FUTURE DIRECTIONS .....   | 98  |
| REFERENCES .....  | 100 |
| Appendix.....   | 107 |
| Appendix A1. Organic Oxidation – Tailoring the Photocatalytic Activity of Cerium Oxide and<br>Zinc Oxide Modified Graphitic Carbon Nitride Nano-Composites Towards Indigo Carmine<br>Degradation..... | 108 |
| A.1 INTRODUCTION .....  | 109 |
| A.2 EXPERIMENTAL SECTION .....  | 110 |
| A.2.1 Fabrication of Working Electrodes. ....   | 110 |
| A.2.2 Photoelectrochemical Measurements.....  | 111 |
| A.3 RESULTS AND DISCUSSIONS .....   | 111 |
| A.3.1 Photoelectrochemical Catalyst Characterization .....  | 111 |

|   |     |
|---|-----|
| A.4 CONCLUSION .....  | 113 |
| Appendix A2. Organic Chlorination – Electrochemical Chlorination of Heterocyclic Pyridones<br>..... | 114 |
| A2.1 INTRODUCTION .....   | 116 |
| A2.2 EXPERIMENTAL SECTION .....   | 117 |
| A2.2.1 Materials.....   | 117 |
| A2.2.2 Synthesis of 1-(2,2-Dimethoxyethyl)-4(1H)-Pyridinone.....                                    | 118 |
| A2.2.3 Electrochemical Characterization .....   | 118 |
| A2.2.4 Simple Electrochemical Chlorination H-Cell .....   | 119 |
| A2.2.5 Electrochemically-Generated Chlorine Gas Facilitated Cell .....                              | 120 |
| A2.2.6 GC-MS Analysis and LLE Substrate Isolation .....   | 122 |
| A2.2.7 NMR and TLC Plate Isolation .....  | 123 |
| A2.2.8 LC-MS Analysis .....   | 123 |
| A2.3 RESULTS AND DISCUSSION .....   | 124 |
| A2.3.1 Substrate Selection, System Constraints and Characterization.....                            | 124 |
| A2.3.2 GC-MS Characterization Conversion for Compound A and B .....                                 | 128 |
| A2.3.3 Gas Cell Experiments.....  | 133 |
| A2.3.4 LC-MS Characterization and Conversion Rates for Compounds A, B and C .....                   | 135 |
| A2.3.5 Limitations of this work .....   | 139 |
| A2.4 CONCLUSION .....   | 139 |
| VITA .....  | 141 |
| PUBLICATIONS.....   | 141 |
| PRESENTATIONS.....  | 142 |
| PROPOSALS .....   | 143 |



# List of Figures

|   |    |
|---|----|
| <b>Figure 1.1</b> Inverse correlation of abundance and price of chemical elements. The arrows depict elements of interest for this work compared to platinum. <sup>8</sup> .....  | 3  |
| <b>Figure 1.2</b> A volcano plot showing the bulk exchange current density versus the bond adsorption strength of metal-hydride intermediates for transition metals, PGMs are located at the peak. ....   | 5  |
| <b>Figure 1.3</b> Polarization curves showing a beneficial effect for a nano-electrocatalyst on a Ti substrate versus a bulk electrocatalyst, Pt is displayed as a reference material .....   | 8  |
| <b>Figure 1.4</b> Schematic of solar adsorption for (a) a bare, (b) an electrodeposited and (c) a drop casted film on a silicon substrate-based electrode for the HER. CoP TMPs compared to Pt surface loadings of loaded with 0.05, 0.10, and 0.20 mg/cm <sup>2</sup> coatings on Si indicate improved kinetics while higher loadings limit the overall current density, likely from shadowing. .... | 11 |
| <b>Figure 1.5</b> An inverse correlation between the band gaps of common photo-absorbers and the solar spectrum is shown. Common photo-absorbers are used as substrates for photoelectrodes in photoelectrochemical water splitting applications. The band edge alignment must straddle the water splitting redox potentials. <sup>22,23</sup> .....  | 15 |
| <b>Figure 1.6</b> A depiction of photons from the sun exciting electrons from the valance band to the conduction band of a photocatalyst for oil spill remediation. <sup>24</sup> .....   | 17 |
| <b>Figure 2.1</b> A depiction of the electrode fabrication process to form a Ti substrate-based working electrode and an FTO on glass substrate-based working electrode with a deposited electrocatalyst and photocatalyst films, respectively. ....  | 23 |
| <b>Figure 2.2</b> Use of a potentiostat in electrochemical engineering: CE, WE, REF, are counter electrode, working electrode, reference electrode, respectively. The electrolysis of water occurs when electrons are supplied to the cathode to perform the HER (Equation 1.1) and removed from the anode to perform the OER (Equation 1.2). Here, the WE is depicted as an anode. ....              | 24 |
| <b>Figure 2.3</b> Polarization curve highlighting the non-faradaic and faradaic regions of interest when determining the voltage window against V vs RHE and V vs Hg/HgO. The value for the thermodynamic value of the hydrogen evolution reaction is displayed with a dashed line. The figure compares polarization curve plotted against a reference electrode and then corrected to the RHE.....   | 28 |
| <b>Figure 2.4</b> Over-potentials at $-10 \text{ mA cm}^{-2}$ are taken from the polarization curve of an electrocatalyst working electrode and subtracted by the thermodynamic value.....  | 29 |
| <b>Figure 2.7</b> Tafel plots for Pt-based electrocatalysts and Ni <sub>1-x</sub> Mo <sub>x</sub> alloy NP electrocatalysts in alkaline media from Chapter 3. The inlay describes how the linear portion is taken to be plotted separately and that it can be extrapolated to determine the exchange current densities of the catalysts.....  | 32 |
| <b>Figure 3.1</b> A depiction of the electrode fabrication process to produce Ni <sub>1-x</sub> Mo <sub>x</sub> alloy NP working electrodes. The alloy NPs drop-casted on Ti substrates are annealed at 450 °C under 5% H <sub>2</sub> /Ar atmosphere, attached to an insulated Cu wire using silver paint, and further coated with epoxy to template the electrodes.....                             | 47 |
| <b>Figure 3.2</b> Powder X-ray diffraction patterns of [A] cubic and [B] hexagonal Ni <sub>1-x</sub> Mo <sub>x</sub> alloy NPs produced with varying Mo concentrations: (a) x = 0.011, (b) x = 0.036, (c) x = 0.066, (d) x  |    |

= 0.087, (e)  $x = 0.012$ , (f)  $x = 0.015$ , and (g)  $x = 0.019$ . The vertical gray line shown in A corresponds to cubic Ni structure (JCPDS # 01-070-0989) whereas the vertical gray line shown in B represents hexagonal Ni (JCPDS # 01-089-7129) structure. The diffraction peaks corresponding to hexagonal and cubic  $\text{Ni}_{1-x}\text{Mo}_x$  impurities are shown in \* and #, respectively. 51

**Figure 3.3** Powder X-ray diffraction patterns (zoomed in to display the most intense peak) of [A] cubic and [B] hexagonal  $\text{Ni}_{1-x}\text{Mo}_x$  alloy NPs with varying Mo concentration: (a)  $x = 0.011$ , (b)  $x = 0.036$ , (c)  $x = 0.066$ , (d)  $x = 0.087$ , (e)  $x = 0.012$ , (f)  $x = 0.015$ , and (g)  $x = 0.019$ . The vertical gray line shown in A corresponds to (111) plane in cubic Ni structure (JCPDS # 01-070-0989) whereas the vertical gray line shown in B represents (101) plane in hexagonal Ni (JCPDS # 01-089-7129) structure. The diffraction peaks corresponding to hexagonal and cubic  $\text{Ni}_{1-x}\text{Mo}_x$  impurities are shown in \* and #, respectively. .... 52

**Figure 3.4** Low resolution TEM images of cubic  $\text{Ni}_{1-x}\text{Mo}_x$  alloy NPs with varying elemental composition: [A]  $x = 0.011$  ( $18.4 \pm 2.9$  nm), [B]  $x = 0.018$  ( $24.9 \pm 5.4$  nm), [C]  $x = 0.036$  ( $22.1 \pm 4.5$  nm), [D]  $x = 0.066$  ( $29.9 \pm 4.8$  nm), [E]  $x = 0.087$  ( $28.9 \pm 5.4$  nm) and [F]  $x = 0.114$  ( $42.9 \pm 6.8$  nm). Insets in (C) and (D) show high resolution images of single particles with lattice fringes of 2.060 and 2.093 Å, corresponding to an expanded (111) plane of cubic Ni. .... 55

**Figure 3.5** Size histograms of cubic  $\text{Ni}_{1-x}\text{Mo}_x$  alloy NPs with varying elemental composition: [A]  $x = 0.011$ , [B]  $x = 0.018$ , [C]  $x = 0.036$ , [D]  $x = 0.066$ , [E]  $x = 0.087$  and [F]  $x = 0.114$ . .... 56

**Figure 3.6** High resolution TEM images of cubic  $\text{Ni}_{1-x}\text{Mo}_x$  alloy NPs with varying elemental composition: [A]  $x = 0.036$ , [B]  $x = 0.066$ , [C]  $x = 0.087$  and [D]  $x = 0.114$  showing lattice fringes of 2.060, 2.070, 2.076, and 2.093 Å, respectively. These values correspond to an expanded (111) plane in face-centered-cubic Ni. .... 57

**Figure 3.7** High resolution TEM images of cubic  $\text{Ni}_{1-x}\text{Mo}_x$  alloy NPs with varying elemental composition: [A]  $x = 0.066$ , [B]  $x = 0.087$  and [C]  $x = 0.114$  along with [D-F] their zoomed-in images showing the edge of the particles. With increasing Mo concentration, formation of an amorphous surface coating was noticed. .... 58

**Figure 3.8** Low resolution TEM images of hexagonal  $\text{Ni}_{1-x}\text{Mo}_x$  alloy NPs with varying elemental composition: [A]  $x = 0.012$  ( $23.6 \pm 5.3$  nm), [B]  $x = 0.015$  ( $19.3 \pm 4.7$  nm) and [C]  $x = 0.019$  ( $23.4 \pm 3.7$  nm) along with corresponding [D-F] size histograms, respectively. .... 59

**Figure 3.9** Low resolution TEM images of [A] cubic ( $47.9 \pm 10.1$  nm), [B] hexagonal ( $46.9 \pm 6.7$  nm) Ni nanocrystals. [C] HRTEM image of cubic Ni NPs showing lattice fringes of 2.030 Å assigned for (111) plane. .... 60

**Figure 3.10** Ni2p and Mo3d XPS spectra of [A,C] cubic  $\text{Ni}_{0.913}\text{Mo}_{0.087}$  and [B,D] hexagonal  $\text{Ni}_{0.990}\text{Mo}_{0.010}$  alloy NPs annealed at 450 °C for 2 h under 5%  $\text{H}_2/\text{Ar}$  atmosphere. In all spectra, solid black lines are experimental data, colored lines are fitted deconvolutions with dash lines representing the doublets, and the solid red lines are spectral envelopes. .... 62

**Figure 3.11** XPS survey spectrum of the annealed  $\text{Ni}_{0.913}\text{Mo}_{0.087}$  alloy NPs. .... 63

**Figure 3.12** Ni2p and Mo3d XPS spectra of [A,C] cubic  $\text{Ni}_{0.934}\text{Mo}_{0.066}$  and [B, D] hexagonal  $\text{Ni}_{0.990}\text{Mo}_{0.010}$  alloy NPs comparing differences in spectra between the as-synthesized and annealed samples. In all spectra, the green (as-synthesized) and black (annealed) lines represent experimental data and red and brown lines correspond to spectral envelopes. .... 64

**Figure 3.13** Representative FT-IR spectra of cubic  $\text{Ni}_{0.913}\text{Mo}_{0.087}$  alloy NPs (a) before and (b) after annealing at 450 °C for 2 h under 5%  $\text{H}_2/\text{Ar}$  atmosphere. As-synthesized NPs show

characteristic peaks corresponding to alkyl stretching (C-H) at 2850 and 2920  $\text{cm}^{-1}$  that can originate from both oleylamine and octadecene ligands. In addition, a broad stretching vibration corresponding to N-H bonds is observed at  $\sim 3100\text{-}3000 \text{ cm}^{-1}$ , suggesting the presence of oleylamine ligands bound to alloy NP surface. Annealed samples show no peaks corresponding to alkyl and alkylamine, consistent with the removal of octadecene and oleylamine from the NP surface. .... 65

**Figure 3.14** Low resolution TEM images of cubic  $\text{Ni}_{0.934}\text{Mo}_{0.066}$  and hexagonal  $\text{Ni}_{0.990}\text{Mo}_{0.010}$  alloy NPs annealed at 450 °C for 2 h under 5%  $\text{H}_2/\text{Ar}$  atmosphere. These images show no significant change in morphology of prior to and after annealing. .... 66

**Figure 3.15** [A] A representative EDAX spectrum of the annealed, cubic  $\text{Ni}_{0.913}\text{Mo}_{0.087}$  alloy NPs. [B] The STEM image and elemental maps of Mo L (red), Ti K (green), and Ni K (blue) recorded from a large area of cubic  $\text{Ni}_{0.913}\text{Mo}_{0.087}$  alloy NPs, showing the elemental distribution. .... 67

**Figure 3.16** PXRD pattern of cubic  $\text{Ni}_{0.913}\text{Mo}_{0.087}$  alloy NPs annealed at 450 °C for 2 h under 5%  $\text{H}_2/\text{Ar}$  atmosphere. The vertical black line corresponds to cubic Ni structure (JCPDS # 01-070-0989). .... 68

**Figure 3.17** [A] Polarization curves and [B] Tafel plots of Ti foil, commercial Pt disc and Pt/C electrocatalysts, and  $\text{Ni}_{1-x}\text{Mo}_x$  alloy NP electrocatalysts for alkaline HER. Data were recorded at 25 °C under nitrogen atmosphere with continuous stirring. .... 70

**Figure 3.18** A plot illustrating the effect of Mo content on the magnitude of the over-potential for  $\text{Ni}_{1-x}\text{Mo}_x$  alloy NPs at current densities of [A] -10 and [B] -20  $\text{mA}/\text{cm}^2$ . Two dashed lines represent the standard HER activity obtained for Pt-based electrodes under alkaline conditions. .... 71

**Figure 3.19** Plots illustrating the stability of  $\text{Ni}_{0.934}\text{Mo}_{0.066}$  alloy NPs for alkaline HER. [A] Polarization curve for before (solid line) and after (dashed line) 9 h of a constant polarization at a current density of -20  $\text{mA}/\text{cm}^2$ . [B] The change in the over-potential over time. .... 74

**Figure 4.1** Summarizing the synthesis of the electrocatalysts from SEM-EDAX measurements of the elemental composition distribution between Ni, Mo, and P where: circles and squares indicate the  $\text{Ni}_2\text{P}$  and  $\text{Ni}_{12}\text{P}_5$  phases, respectively; blue, red, and black denote solids, hollows, and hetero-structured, respectively. .... 82

**Figure 4.2** TEM images depicting the differences in morphology produced from the three different synthesis methods for the  $\text{Ni}_{2-x}\text{Mo}_x\text{P}$  NPs. .... 85

**Figure 4.3** XRD patterns utilized to determine the  $\text{Ni}_2\text{P}$  (top row) and  $\text{Ni}_{12}\text{P}_5$  (bottom row) parent crystal phases. The stacked XRD patterns are the result of samples being synthesized with varying Mo content. The baseline behavior of the top right and top middle patterns are a result of using a different XRD instrument and will be repeated on one instrument. .... 86

**Figure 4.4** Polarization curves of  $\text{Ni}_{1-x}\text{Mo}_x$  alloy NP from chapter 3, binary  $\text{Ni}_2\text{P}$ , and ternary  $\text{Ni}_{2-x}\text{Mo}_x\text{P}$  and  $\text{Ni}_{12-x}\text{Mo}_x\text{P}_5$  electrocatalysts for alkaline HER. Data were recorded at 25 °C under Ar bubbling with continuous stirring. .... 87

**Figure 4.5** Over-potential at  $-10 \text{ mA}/\text{cm}^2$  plotted against percent composition for Mo and P, respectively. .... 89

**Figure 4.6** Plots illustrating the stability of  $\text{Ni}_{1.87}\text{Mo}_{0.13}\text{P}$  NPs for alkaline HER. [A] The polarization curve before (solid line) and after (dashed line) 10 h of a constant applied current at

|   |     |
|---|-----|
| –10 mA/cm <sup>2</sup> . [B] Change in over-potential per 10 h of –10 mA/cm <sup>2</sup> , applied without ohmic correction. ....   | 92  |
| <b>Figure A.1</b> XRD patterns for cerium and zinc oxide carbon nitride composites with 0.136 mol% precursor ratios. ....   | 110 |
| <b>Figure A.2</b> Transient photocurrent of g-C <sub>3</sub> N <sub>4</sub> , CeO <sub>2</sub> /g-C <sub>3</sub> N <sub>4</sub> , ZnO/g-C <sub>3</sub> N <sub>4</sub> and their physical mixture under the excitation of 365 nm UV light radiation in 0.1 M Na <sub>2</sub> SO <sub>4</sub> and the correlation to indigo carmine degradation. ....   | 112 |
| <b>Figure A2.1</b> A visual depiction of a [A] simple electrochemical H-cell and [B] fashioned gas-generating electrochemical cell, utilized to chlorinate organic substrates dispersed in 0.5 M HCl (orange). The blue represents 0.5 M HCl without any organic substrate. Gas generation is depicted by bubbles: chlorine (green), hydrogen (light blue), nitrogen (yellow), and the mixture of gases (dark blue). ....   | 122 |
| <b>Figure A2.2</b> The chemical structures for the [A-C] heterocyclic substrates and [D-F] major chlorinated products: [A] n-methyl-2-pyridone, [B] 1-(2,2-dimethoxyethyl)-4(1 <i>H</i> )-pyridinone, [C] 1,6-dimethyl-4-oxo-1,4-dihydropyridine-3-carboxylic acid, [D] 3-chloro-1-methyl-2(1 <i>H</i> )-pyridone, 5-chloro-1-methyl-2(1 <i>H</i> )-pyridone, and 3,5-dichloro-1-methyl-2(1 <i>H</i> )-pyridone; [E] 3,5-dichloro-1-(2,2-dimethoxyethyl)-4(1 <i>H</i> )-pyridinone; and [F] 5-chloro-1,6-dimethyl-4-oxo-1,4-dihydropyridine-3-carboxylic acid. ....   | 126 |
| <b>Figure A2.3</b> Cyclic voltammogram for 0.5 M HCl with (solid) and without (dashed) 10 mM 2MP at 0.1 V/sec. ....   | 128 |
| <b>Figure A2.4</b> [A-E] GC-MS chromatographs depicting the conversion of compound A to form chlorinated products over time (0–40 min) at 2.5–3.0 V. The SM (5.12 min) was observed to decrease over time forming major and minor products. [F] GC-MS peak area-based conversion for 2MP highlighting the major products. Each data point represents an independent experiment, i.e., no sub-sampling. ....   | 130 |
| <b>Figure A2.5</b> Chromatographs for [A] compound A without byproducts, [F] compound A with byproducts and [K] compound B conversion products. MS spectra correlating to the observed chromatograph peaks of [B-E] 2MP (5.12 min, 109 m/z), 2MP-Cl (5.77 min, 143 m/z), 2MP-Cl' (6.23 min, 143 m/z), 2MP-2-Cl (6.80 min, 177 m/z); [G-J] 2MP-OH-Cl (5.94 min, 161 m/z), 2MP-OH-Cl' (6.09 min, 161 m/z), 2MP-2-Cl-OH (7.00 min, 195 m/z), 2MP-2-Cl-OH' (7.17 min, 195 m/z); [L-O] 4P (9.80 min, 183 m/z), 4P-Cl (11.10 min, 217 m/z), 4P-2-Cl (12.68 min, 253 m/z), and an unknown minor byproduct (13.55 min, 297 m/z), respectfully. .... | 132 |
| <b>Figure A2.6</b> GC chromatographs for the conversion of compounds A and B via an [A, B] H-cell and a [C, D] gaseous-cell, respectively. ....   | 135 |
| <b>Figure A2.7</b> Conversion of compound B in 0.5 M HCl at [A] 6.0V (25.99 mg), [B] 7.5V (27.53 mg), and [C] 10.0V (28.18 mg). Conversion of 1,6-dimethyl-4-oxo-1,4-dihydropyridine-3-carboxylic acid (compound C) at [D] 6.0V (6.72 mg). Data was collected from the peak areas found on LC-MS without an extraction procedure, all results are shown as %SM. ....  | 138 |

# Abstract

## ENGINEERING OF EARTH-ABUNDANT ELECTROCHEMICAL CATALYSTS

By Dylan D. Rodene, Ph.D.

A dissertation submitted in partial fulfillment of the requirements for the degree of Doctor of Philosophy at Virginia Commonwealth University.

Virginia Commonwealth University, 2019.

Advisor: Dr. Ram B. Gupta, Associate Dean for Faculty Research Development and Professor of Chemical & Life Science Engineering, Department of Chemical & Life Science Engineering

Alternative energy research into hydrogen production via water electrolysis addresses environmental and sustainability concerns associated with fossil fuel use. Renewable-powered electrolyzers are foreseen to produce hydrogen if energy and cost requirements are achieved. Electrocatalysts reduce the energy requirements of operating electrolyzers by lowering the reaction kinetics at the electrodes. Platinum group metals (PGMs) tend to be utilized as electrocatalysts but are not readily available and are expensive.  $\text{Ni}_{1-x}\text{Mo}_x$  alloys, as low-cost and earth-abundant transition metal nanoparticles (NPs), are emerging as promising electrocatalyst candidates to replace expensive PGM catalysts in alkaline media. Pure-phase cubic and hexagonal  $\text{Ni}_{1-x}\text{Mo}_x$  alloy NPs with increasing Mo content (0–11.4%) were synthesized as electrocatalysts for the hydrogen evolution reaction (HER). In general, an increase in HER activity was observed with

increasing Mo content. The cubic alloys were found to exhibit significantly higher HER activity in comparison to the hexagonal alloys, attributed to the higher Mo content in the cubic alloys. However, the compositions with similar Mo content still favored the cubic phase for higher activity. To produce a current density of  $-10 \text{ mA/cm}^2$ , the cubic and hexagonal alloy NPs require over-potentials ranging from  $-62$  to  $-177 \text{ mV}$  and  $-162$  to  $-242 \text{ mV}$ , respectively. The cubic alloys exhibited over-potentials that rival commercial Pt-based electrocatalysts ( $-68$  to  $-129 \text{ mV}$  at  $-10 \text{ mA/cm}^2$ ). The cubic  $\text{Ni}_{0.934}\text{Mo}_{0.066}$  alloy NPs showed the highest alkaline HER activity of the electrocatalysts studied and therefore a patent application was submitted.

Bulk Ni–Mo phases have been known as electrocatalysts for the HER for decades, while recently transition metal phosphides (TMPs) have emerged as stable and efficient PGM alternatives. Specifically,  $\text{Ni}_2\text{P}$  has demonstrated good HER activity and improved stability for both alkaline and acidic media. However,  $\text{Ni}_2\text{P}$  electrocatalysts are a compromise between earth-abundance, performance (lower than Ni–Mo and PGMs) and stability. For the first time Ni–Mo–P electrocatalysts were synthesized with varying atomic ratios of Mo as electrocatalysts for alkaline HER. Specific phases, compositions and morphologies were studied to understand the intrinsic properties of TMPs leading to high HER activity. The  $\text{Ni}_{1.87}\text{Mo}_{0.13}\text{P}$  and  $\text{Ni}_{10.83}\text{Mo}_{1.17}\text{P}_5$  NPs were shown to be stable for 10 h at  $-10 \text{ mA cm}^{-2}$  with over-potentials of  $-96$  and  $-82 \text{ mV}$  in alkaline media, respectively. The  $\text{Ni}_{1.87}\text{Mo}_{0.13}\text{P}$  and  $\text{Ni}_{10.83}\text{Mo}_{1.17}\text{P}_5$  NPs exhibited an improved performance over the synthesized  $\text{Ni}_2\text{P}$  sample ( $-126 \text{ mV}$  at  $-10 \text{ mA cm}^{-2}$ ), likely a result of the overall phosphorous content and hetero-structured morphologies. A strong correlation between phase dependence and the influence of Mo on HER activity needs to be further investigated.

Furthermore, understanding the intrinsic properties of electrocatalysts leading to high water splitting performance and stability can apply electrocatalysts in other research applications, such

as photoelectrochemical (PEC) water splitting, water remediation and sustainable chemical processing applications. Contributions to photocatalytic water remediation and electrochemical chlorinated generation to halogenate pyridone-based molecules are reported. Electrochemical techniques were developed and reported herein to aid in understanding electrochemical performance, chemical mechanisms and the stability of electrocatalysts at the electrode-electrolyte interfaces.

## **Chapter I. Introduction of Electrocatalysis**



## 1.1 Introduction of Electrocatalysis

Increasing global population and standards of living are contributing to growing energy demands and rising CO<sub>2</sub> levels associated with the burning of fossil fuels.<sup>1</sup> Relying on finite fossil resources for energy is resulting in air quality deterioration, global warming, and sustainability issues.<sup>1</sup> Solar energy is abundant, however, it requires an energy carrier. Hydrogen, as an energy carrier, can be generated by solar or wind powered electrolyzers and then converted back into energy via fuel cells. Electrolyzers require a highly active and stable cathode material for the hydrogen evolution reaction (HER). Acid-based electrolyzers are desirable for high HER activity and compatibility in applications that require a proton exchange membrane (PEM) and, therefore, a more compact design.<sup>2</sup> However, most active non-platinum group metals (PGMs) catalysts degrade in acid. Therefore, hydrogen is produced in alkaline media. Hydrogen generation via electrolysis requires electrolyzers to operate with minimal energy input over long lifecycles of operation.

Clean alternatives to solve the energy crisis are proposed to utilize devices powered by electrocatalysis and photocatalysis. However, materials available for energy conversion devices include costly, scarce, intrinsically limited, and/or have poor stability. PGMs, the most commonly used electrocatalysts, have good intrinsic properties including inertness, stability and kinetic efficiency as compared to the most earth-abundant materials.<sup>3</sup> However, the use of PGMs are not commercially viable in scalable energy conversion devices due to scarcity and expenses.<sup>4-7</sup> PGMs are located in the top-left corner of a price verses abundance plot, depicting that PGMs are not commercially desirable to elements that are magnitudes more abundant, specifically, nickel (Ni), molybdenum (Mo), and phosphorous (P) (Figure 1.1). Therefore, to reduce the use of PGMs, earth-abundant catalysts with improved performance and stability similar to PGMs need to be developed.

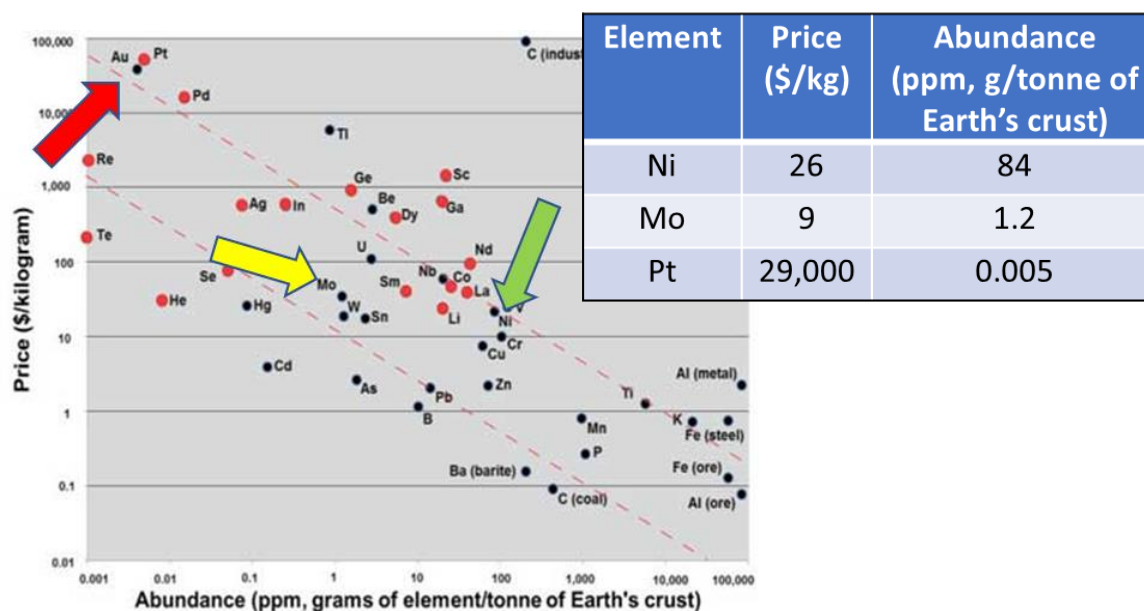
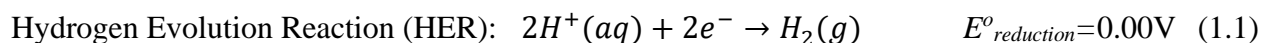


Figure 1.1 Inverse correlation of abundance and price of chemical elements. The arrows depict elements of interest for this work compared to platinum.<sup>8</sup>

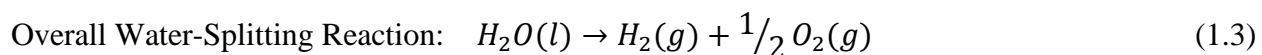
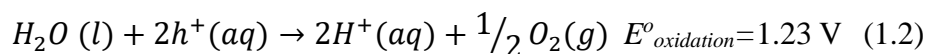
Electrocatalysts are also implemented to solve intrinsic limitations by functionalization of semiconductor surfaces for photocatalyst applications. Electrocatalysts and photocatalysts have applications beyond water splitting, such as water remediation and chemical processing. For example, in electrochemical water treatment processes, complete conversion of benzene and phenol to CO<sub>2</sub> was observed.<sup>9,10</sup> Current industrial production of chlorine is done electrochemically, and new chemical synthesis reactions are being proposed electrochemically as well. Furthermore, earth-abundant electrocatalysts such as Ni–Mo alloys and transition metal phosphides (TMPs) are foreseen to improve the efficiency of both electrolyzers and photocatalysts for all suggested applications.

## 1.2 Fundamentals of Electrocatalysis for Water Splitting

Hydrogen is plentiful across the planet; however, it is not found naturally in a pure form but exists bounded in molecular compounds, mainly water. Therefore, water splitting via an alternative energy driven device is foreseeable to supply clean and sustainable hydrogen.<sup>11</sup> Overall, water splitting is thermodynamically unfavorable, requiring more energy input than that recovered. Hydrogen production from water proceeds via two half reactions: the hydrogen evolution reaction (HER) and the oxygen evolution reaction (OER). The two half reactions and overall water splitting reaction in acidic media are given below:



Oxygen Evolution Reaction (OER):



The activity of an HER catalyst depends on the pH of the supporting electrolyte; alkaline media forms hydrogen atoms from the dissociation of water molecules, while acidic media forms hydrogen atoms from the discharge of protons. Alkaline media typically lowers or decreases the materials activity, however, some materials have shown good stability and high performance.

The thermodynamic energy requirement to produce hydrogen from water is 0 V vs. RHE. However practically, the required energy is greater than 0 V vs. RHE due to inherent kinetic limitations of the materials facilitating the reactions, which is expressed as over-potentials. Materials that have a high electrochemical stability with low kinetic limitations for a given reaction are considered as electrocatalysts. For example, platinum (Pt) exhibit lower over-potentials than

stainless steel and graphite for the HER. The kinetics, including over-potential and Tafel slope, of the HER is characteristic/relevant to the electrocatalyst, indicating an ability to perform efficient reactant binding, intermediate mobility, product formation and removal.<sup>3</sup> The exchange current density is a parameter that describes the intrinsic rate of electron transfer between an analyte (i.e., 2 M KOH) and the electrode. Also, the exchange current density contributes to the Tafel equation and is used to compare current dependence of electrolytic processes with respect to over-potential. Figure 1.2 illustrates the correlation between the exchange current density of bulk transition metals and their bonding energies to adsorb and form hydrogen intermediates; a Goldilocks bond range is desired to readily form hydrogen without irreversibly adhering hydrogen to the catalyst.<sup>12</sup> Therefore, for water splitting to be feasible, earth-abundant catalysts with the same stability and kinetic performance as PGMs were attempted to be developed. This work stresses progress towards the discovery of new electrocatalysts to replace PGMs in hydrogen generation, implementing electrocatalysts on the cathode of a three-electrode cell acting as an electrolyzer.

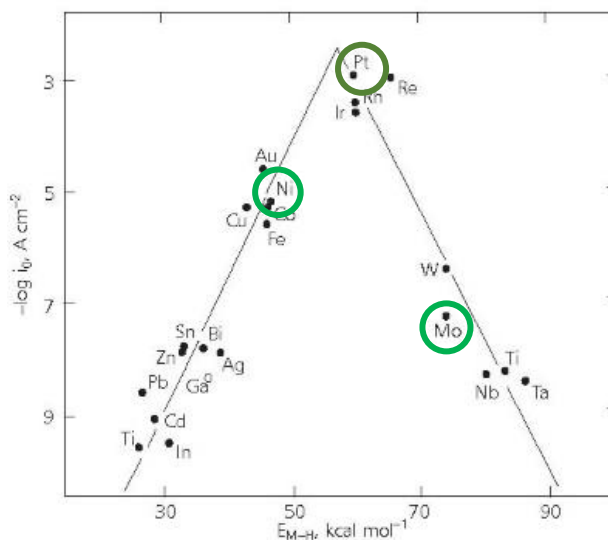


**Figure 1.2** A volcano plot showing the bulk exchange current density versus the bond adsorption strength of metal-hydride intermediates for transition metals, PGMs are located at the peak.<sup>12</sup>

The surface of an electrode can be selected, replaced, and modified to be active for a desired reaction in a similar way to heterogeneous catalysis. The primary difference is that the driving force for an electrocatalyst to perform a chemical reaction is through an applied electrical potential, instead of temperature. The applied bias can further increase the local concentrations of reactive species at the surface, supply the necessary energies of reactions, and amplify the reaction.

We can inform the design of electrocatalysts for the HER from well-established hydrodesulfurization (HDS) catalytic processes to remove sulfur impurities from hydrocarbon fuels.<sup>13</sup> Well-known catalysts for HDS are theorized to be regulated by the same reaction rate determining mechanisms as the HER. The reaction rates for both processes are thought to be controlled by the reversible and dissociative binding of hydrogen molecules to the surface of the catalyst.<sup>13</sup> Therefore, known HDS catalysts as Ni–Co, Ni–Mo, Fe–Ni, etc. and their phosphonate forms are considered to be strong candidates for HER studies due to the synergistic effect and enhanced electronic structure. The theory behind the increased binding kinetics of the TMPs results from Mo and P atoms adding electronegativity to the Ni catalysts. Furthermore, the surface activity can be tuned for ternary TMPs with the additional an extra element incorporated into stable crystal phases, straining the lattice structure and surface. The concentration of Mo incorporated into nickel and nickel phosphide crystal phases is a key factor in controlling conductivity, reactant binding properties and surface activity.

Ni–Mo alloys have long been investigated as HER catalysts and have consistently shown competitively low over-potentials. The elemental composition of the electrocatalyst inherently alters the electrocatalytic performance while potentially aiding in areas such as stability, especially when dealing with ternary compositions. As a binary alloy, Ni–Mo, suffers from acid electrolyte stability, while metal composites, such as MoC<sub>2</sub>, have shown good acid stability.<sup>2,14,15</sup> Recently,

transition metal phosphides (TMPs) as earth-abundant materials have shown promising electrocatalytic properties for the hydrogen evolution reaction (HER).<sup>13</sup> As electrocatalysts, TMPs show low over-potentials (~134 mV, Ni<sub>2</sub>P) and good stability for the HER under relevant current densities (10 mA/cm<sup>2</sup>).<sup>13,16</sup> Ni<sub>2</sub>P nanoparticles (NPs) were shown to exhibit high stability and relatively high performance under most conditions, including in acidic electrolytes.<sup>13</sup> Ternary Ni composites composed of Mo and C have shown both good activity and acid stability.<sup>2</sup> Specifically, Ni<sub>2-x</sub>Mo<sub>x</sub>P is a potential ternary TMP of interest to understand synergistic effects of combining these elements, owing to high performance of Ni–Mo and the stability of composites.

Electrocatalyst inefficiencies can be reduced by synthesizing a phase-pure crystalline nano-scale material. In general, the efficiency of the material can be increased by increasing the ratio of surface area to bulk, allowing for more surface reaction sites. The nano-scale also can mitigate defect sites present in multi-phase materials.<sup>17</sup> On the other hand, the surface of the material is considered to be a defect, and increasing the surface area ratio thus increases the surface defects. Therefore, there is plausibly an optimum particle size for each material to achieve a satisfactory crystallinity while maintaining a high reactive surface area. In general, the nano-scale has been shown to be beneficial in the electrocatalytic activity of the transition metal phosphides (TMPs), as seen in Figure 1.3.<sup>13,18</sup> By fundamentally understanding what makes a good electrocatalyst, one can rationally design alternatives to PGMs for specific electrochemical applications.

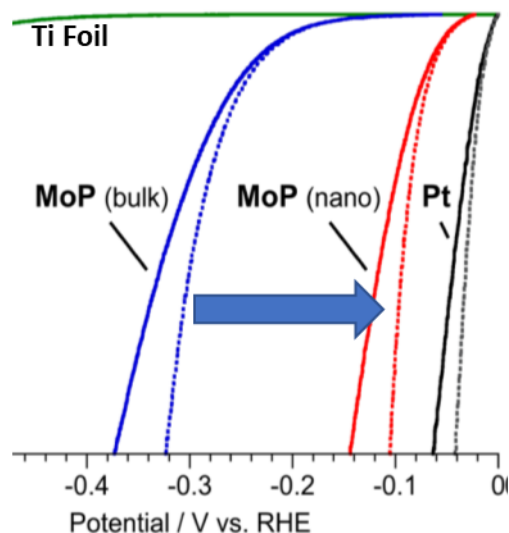


**Figure 1.3** Polarization curves showing a beneficial effect for a nano-electrocatalyst on a Ti substrate versus a bulk electrocatalyst, Pt is displayed as a reference material.<sup>13,18</sup>

When expanding electrochemistry and electrocatalysis to other reactions beyond water splitting, a better understanding of the fundamental chemistry occurring in electrochemical system can be gained. The electrolyte and other components of the solvent system may certainly contribute to the reaction performance instead of being a spectator or conducting agent. For example, the remediation of organic pollutants may be influenced by the electrolyte, solvent system, applied bias, and electrodes. Each electrochemical component can maintain a respective role in the reaction mechanism to facilitate existing and new chemistries.

### 1.3 Fundamentals of Photocatalysis and Photoelectrodes

Photocatalysis utilizes a semiconductor material to convert light in electrical energy. Free electron-hole pairs are generated when incident light (photons with associated energies exceeding the band gap of the photocatalyst) excites an electron ( $e^-$ ) from the valance band (VB) of a

semiconductor (photocatalyst, WE) to the conduction band (CB), leaving behind holes ( $h^+$ ) in the VB. A material with a band gap exceeding 1.23 eV is needed to facilitate water splitting thermodynamically. However, in application a band gap should significantly exceed this value due to kinetic over-potentials and likely miss-aligned band edges. The band gap of a semiconductor material is inversely proportional to the wavelengths of the solar spectrum that the specific material can absorb (Figure 1.4, 1.5). Therefore, the band gap of a material plays a vital role in the solar-to-hydrogen (STH) conversion efficiency. A large band gap material only absorbs high energy photons, this is a considerable drawback due to lower amounts of high energy photons available in the solar spectrum, limiting absorption to the UV region. Narrower band gap materials will absorb more photons of the solar spectrum, into the visible spectrum, producing a lower voltage but higher current.

Photocatalyst particles or substrates can be made into electrodes to be evaluated using a photoelectrochemical (PEC) technique (Figure 1.4, 1.5). All of the same principles established in electrocatalytic water splitting still apply to photo-electrochemical (PEC) applications. However, a portion of the voltage is now supplied via the semiconductor material absorbing photons. Furthermore, for PEC water splitting, applying an external voltage can aid to align band edges to match redox reaction potentials, record photovoltages, or supply excess energy for materials with small band gaps or that are kinetic limited.<sup>19</sup> Photocatalysts and photoelectrodes are typically functionalized by an active material to improve the overall performance.<sup>19</sup> The functionalization of a semiconductor exhibits similar fundamental principles to that of a good electrocatalyst, specifically to facilitate a reaction at the electrolyte-electrode interface without kinetic barriers and to aid in stability. Alternatively, the functionalization of a photocatalyst is also aimed at improving



the electronic structure of the semiconductor to improve the photo absorption and the energetics of electron-hole pair generation.

The desired characteristics of an efficient solar water splitting electrode are listed as follows:

- 1) the surface of the catalyst must readily adsorb reactants and desorb products while rapidly converting intermediate species,
- 2) the charge transfer between the surface of the electrode to the reactants occur spontaneously, to minimize kinetic energy losses resulting in excess over-potential,<sup>19</sup>
- 3) the catalyst must be stable in the desirable reaction media under an applied potential and photo-irradiation,
- 4) the catalyst must generate a sufficient photo-voltage by absorbing a broad range of solar irradiation,
- 5) the catalyst must have a proper band gap, and the band gap edges must be suitable for each water splitting half reaction,
- 6) the catalyst must efficiently use photo-generated electrons and holes, and
- 7) the catalyst must be inexpensive.

Implementing an electrocatalyst layer on the surface of a photoelectrode will aid to improve or satisfy the criteria listed above. Figure 1.4 depicts how an electrocatalyst coating would be utilized on a photoelectrode and the movement of electrons. Points 1–3 are the definition and drive to develop and implement electrocatalysts. In regards to points 2 and 4, functionalization can aid in charge transfer kinetics to eliminate excessive over-potentials, reactions can become feasible by decreasing the external bias required. Specific to point 3, an electrocatalyst will facilitate surface

reactions, meaning the stability of the photocatalyst can be increased. Specific to points 5–7, utilizing electrocatalysts allows the use of more common photocatalysts instead of exotic materials because requirements of the photocatalyst are reduced, therefore photo-generated electron-hole separation can be readily achieved.<sup>20</sup> Furthermore, cost can be reduced by limiting expensive materials to loadings 0.05, 0.10, and 0.20 mg/cm<sup>2</sup>.<sup>21</sup> By dissecting a PEC electrode into two parts, the electrocatalyst coating and the bulk photocatalyst, allows for the photocatalyst to remain as a relatively inexpensive optimized photo-absorber while the coating can be presented as an optimized electrocatalyst, instead of requiring the photo-absorber to perform both functions.

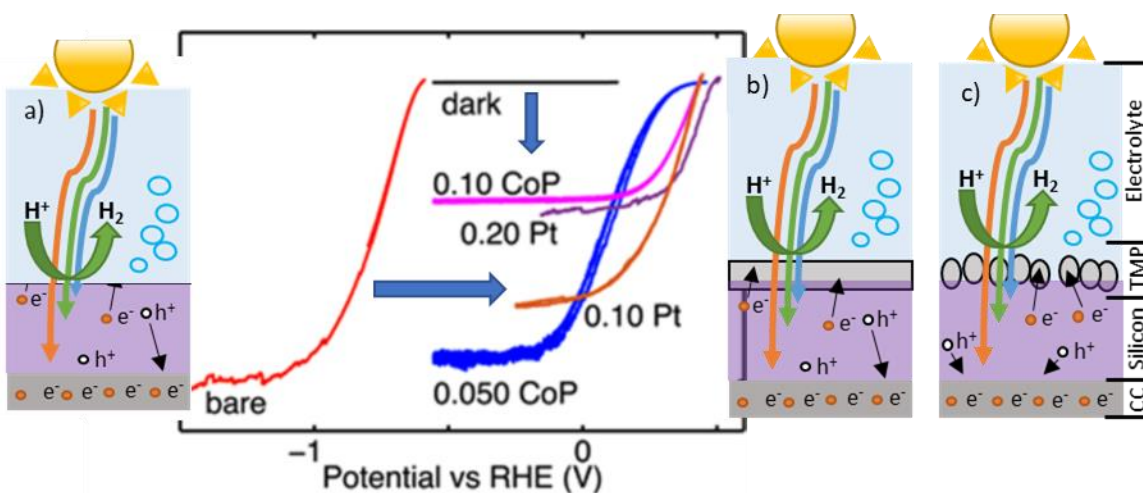


**Figure 1.4** Schematic of solar adsorption for (a) a bare, (b) an electrodeposited and (c) a drop casted film on a silicon substrate-based electrode for the HER. CoP TMPs compared to Pt surface loadings of loaded with 0.05, 0.10, and 0.20 mg/cm<sup>2</sup> coatings on Si indicate improved kinetics while higher loadings limit the overall current density, likely from shadowing.<sup>21</sup>

## **1.4 Recent Advancements in Semiconductor Materials for Photoelectrochemical Water Splitting for Hydrogen Production Using Visible Light**

We have published this work in-depth as: Saraswat, Sushil Kumar; Rodene, Dylan D.; Gupta, Ram B., Recent advancements in semiconductor materials for photoelectrochemical water splitting for hydrogen production using visible light, *Renewable & Sustainable Energy Reviews* (2018), 89, 228-248. <https://doi.org/10.1016/j.rser.2018.03.063>., and provides an in-depth review of photoelectrochemical (PEC) water splitting while highlighting the importance of stable and efficient photocatalysts and electrocatalysts.<sup>22</sup> The article provides a holistic view of the technology and has been cited by >40 publications in one year alone. The key point in this work are:

Water splitting technology directly stores solar energy into the chemical bonds of diatomic hydrogen to be used as a clean fuel without producing any unwanted side reactions, byproducts or environmentally polluting compounds. Semiconductor materials are needed for a photoelectrochemical (PEC) device to catalytically convert photons from sunlight into chemical energy. Materials implemented in a device for sustainable hydrogen production are required to be inexpensive, highly photo-active, chemically stable, environmentally sustainable, and have a high solar-to-hydrogen conversion efficiency. Although many semiconductor composites and nanostructures have been examined, thus far, no material satisfies all criteria of an implementable photocatalyst, as many materials do not show necessary energy conversion efficiency. Materials that depicted high efficiency, often rely on the ultraviolet portion of the solar spectrum, which does not contain a large enough number of photons for the industrial utilization of PEC water splitting

technologies. Focus should be shifted towards the visible spectrum for hydrogen production. Recent advancements in the activity of visible light semiconductors are examined in this published work to include both platinum and non-platinum group materials.

Abundant solar light PEC water splitting using semiconductor photocatalysts is a promising technology for the production of renewable hydrogen energy. Over the last decade, a number of studies were conducted to develop semiconductor photocatalysts that can efficiently use visible light for hydrogen production. Several recent achievements demonstrated that the impact of catalyst preparation and PEC conditions play a vital role in the water splitting process. Although numerous recent innovations, including elemental doping and alloying, Z-scheme compositions, optical modifications, and surface modifications, have enhanced hydrogen production under visible light irradiation, the overall efficiency remains low. For this reason, we need to emphasize on visible range photo-absorbers to increase solar to hydrogen (STH) conversion efficiencies. STH conversion efficiencies have ranged from <1% to 14% for visible light irradiation, with only a few studies reporting >7%. Without consideration of visible range photo-absorbers, STH efficiencies are low, mainly because the UV-active photocatalysts exhibit a low light harvesting capability.

Nanostructure architecture is a prominent tool to supplement the material and junction design to optimize the band structure for enhanced solar water splitting. The hierarchical nano/micro-structures optimized for high current conditions, surface area, charge carriers, and light absorption have received a lot of focus and will continue to be of focus in the immediate future. **An industrially viable future direction of interest would consist of incorporating new functionalizing materials instead of platinum group metals to produce more sustainable and cost effective photocatalysts composites. Incorporating different electrocatalysts as new**

**functionalizing materials can highlight alternative properties to improve a photocatalyst's solar efficiency.**

**A suggested direction of research would be to move away from materials that have been repeatedly modified and tested.** Though those materials are great for proof of concept studies, their efficiencies have repeatedly come up short. Therefore, another option would be to develop new materials and composites, either from promising new studies in literature, including some materials reviewed within the published manuscript, or with the aid of computational work. Modeling and mechanistic studies are of huge importance moving forward and can be extremely challenging. For example, modeling turn-over frequency (TOF) for new materials and new composites. **Understanding and optimizing the mechanism at the electrode-electrolyte interface is key to improving the photo-electrochemical water splitting system beyond utilizing past experimental results.** Therefore, interfacial studies of in situ systems and characterization of electrodes before and after PEC testing should be included. Another notable area of focus would be to develop a standard methodology to evaluate photo-corrosion or catalyst stability, this will help eliminate a number of materials that simply do not have reasonable stability for commercialization.

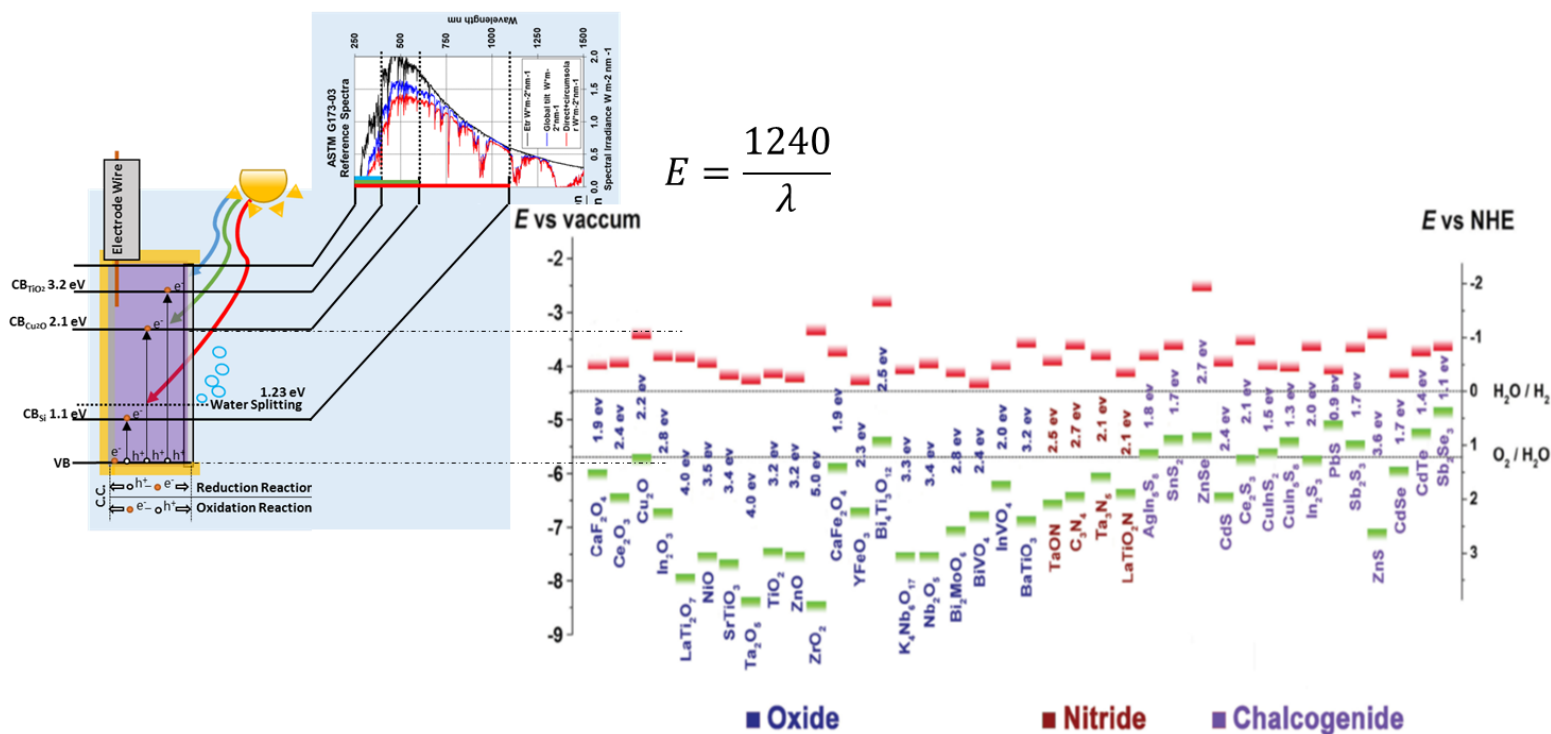


**Figure 1.5** An inverse correlation between the band gaps of common photo-absorbers and the solar spectrum is shown. Common photo-absorbers are used as substrates for photoelectrodes in photoelectrochemical water splitting applications. The band edge alignment must straddle the water splitting redox potentials.<sup>22,23</sup>

## 1.5 Photo-remediation Application – Advancements in Crude Oil Spill Remediation Research after the Deepwater Horizon Oil Spill

We have published this work in depth as: Nyankson, E., Rodene, D. & Gupta, R.B. *Water Air Soil Pollution* (2016) 227: 29. <https://doi.org/10.1007/s11270-015-2727-5>, and allows for a transition away from alternative energy applications and provides a review of oil spill remediation approaches.<sup>24</sup> Currently, use of chemicals or sorbents are implemented to clean up oil spill disasters but come with limitations. More recently, research has shown that a formulation of

dispersants and nano-technology can 100% remediate oil spills by utilizing naturally occurring products. However, if dispersant formulations are not able to be implemented for a handful of reasons, immobilized photocatalysis remediation are the next proposed solution for future remediation scenarios. Highlights from the published manuscript are given:

“An estimated 4.9 million barrels of crude oil and natural gases was released into the Gulf of Mexico during the Deepwater Horizon oil spill of 2010. The Deepwater Horizon oil spill affected the aquatic species in the Gulf of Mexico, vegetation, and the human population along the coast. To reduce the effect of the spilled oil on the environment, different remediation strategies such as chemical dispersant, and mechanical booms and skimmers were utilized. Over 2.1 million gallons of dispersants was applied to minimize the impact of the spilled oil. However, environmental and human toxicity issues arose due to the perceived toxicity of the dispersant formulations applied. After the Deepwater Horizon oil spill, various studies have been conducted to find alternative and environmentally benign oil spill response strategies. Current trends in oil spill sorbent and dispersant formulation research are presented. Furthermore, strategies to formulate environmentally benign dispersants, as well as the possible use of photoremediation, are highlighted” within the published manuscript. The key aspect of photoremediation is that the energy harvested from photons to generate free radicals proceed to oxidize organic pollutants (Figure 1.6). Furthermore, a photoelectrochemical water remediation study is shown in appendix

A1, where graphitic carbon nitride modified with metal oxides is studied for the degradation of indigo carmine.

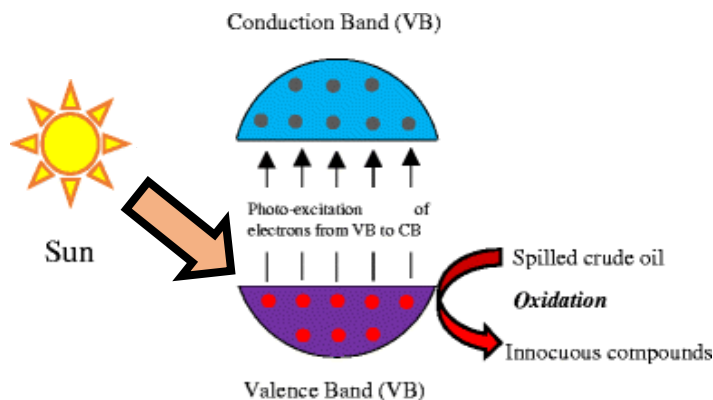


**Figure 1.6** A depiction of photons from the sun exciting electrons from the valance band to the conduction band of a photocatalyst for oil spill remediation. <sup>24</sup>

## 1.6 Dissertation Objectives and Arrangement

**Chapter 2** provides the understanding of how to conduct, collect, and analyze electrochemical water splitting data for electrocatalysts. Earth-abundant electrocatalysts were developed (**Chapters 3, 4**) to potentially rival the hydrogen evolution reaction (HER) activity of platinum group metals (PGMs). Electrodes were formed from earth-abundant unary, binary and ternary nickel-based alloy and composite NPs to electrochemically study the performance of the electrocatalysts for the HER (**Chapters 3, 4**). In addition to the reported experimental work for water splitting electrocatalysts, electrocatalysts can be implemented in applications beyond water splitting electrolyzers, such as photocatalytic and photoelectrochemical (PEC) water remediation applications (**Appendix A1**) and electrochemically driven reactions (**Appendix A2**).

More specifically, **Chapter 3** studies the effect of tuning composition and phase of  $\text{Ni}_{1-x}\text{Mo}_x$  alloy NPs as electrocatalysts for the HER. Furthermore, electrocatalytic performance and stability



in alkaline media was studied. A fundamental understanding of the performance of a  $\text{Ni}_{1-x}\text{Mo}_x$  alloy NPs was gained. Characterization methods of each electrocatalyst was performed for the phase-pure transition metal alloy NPs. The synergistic effects of a binary composite were shown to improve electrochemical activity over unary materials. Furthermore, changing the phase and composition of earth-abundant electrocatalysts plays a vital role in optimizing HER performance.

Building off of the importance of stable and efficient photocatalysts and electrocatalysts, **Chapter 4**, expands on the experimental knowledge gained in **Chapter 3** to develop stable and efficient ternary composite electrocatalysts for the HER. Transition metal phosphides were synthesized in a similar way to that from literature.<sup>13,16,18,25</sup> Various ratios of Mo atoms were incorporated into  $\text{Ni}_2\text{P}$  and  $\text{Ni}_{12}\text{P}_5$  crystal lattices to increase the electrocatalytic activity of the NPs. The addition of phosphide changes the electronegativity of the catalysts and is thought to improving electrochemical stability.  $\text{Ni}_2\text{P}$  was utilized as a standard to compare to synthesized ternary TMP catalysts.  $\text{Ni}_2\text{P}$  has shown consistent performance over other TMPs for electrocatalytic water splitting in our experiments and literature.<sup>13,16,18,25</sup> Furthermore, literature has shown it to be a top candidate in HER performance.<sup>3,16,18,26</sup> TMPs thus far have shown good electrochemical stability. The composition is a key factor in controlling the surface activity. A colloidal synthesis method was employed to control the size, shape and crystallinity of the catalyst NPs. This work developed environmentally-benign materials to replace PGMs for energy solution applications. The inclusion of Mo into the binary TMP matrix created a brand new type of electrocatalysts, specifically  $\text{Ni}_{2-x}\text{Mo}_x\text{P}$  and  $\text{Ni}_{12-x}\text{Mo}_x\text{P}_5$  NPs.

**Appendix A1** expands upon what a water remediation catalyst would look like experimentally. Carbon nitride has a near visible band gap and can be synthesized from earth-abundant urea. To help aid with electron-hole separation and generation. Carbon nitride was

produced as a composite to incorporate low percentages of cerium and zinc oxide into the bulk material. The efficiency of the composites was studied for degradation of a model dye and common water pollutant from fertilizer.

**Appendix A2**, having covered water splitting and remediation, electrocatalysis can be utilized for electrochemically driven syntheses. Electrochemically driven conversion of pyridine-based molecules was studied and a chlorine gas reaction mechanism was found to produce halogenated pyridine-based substrates. There is little literature available on chemistries that functionalize pyridine-based molecules (typically found as constituents in complex molecules). Electrochemistry can be often used as a manner for organic synthesis and commercial chemical production but is not commonly implemented for more than a handful of cases. Here, it was established that electrochemically generated reactive chlorine species will directly react with an organic molecule. Furthermore, the reactive chlorine species generation is controlled directly by the electrochemical input, being able to immediately stop the reaction if desired. Knowledge of electrochemical mechanisms and synthesis routes can expand the electroorganic synthesis field.

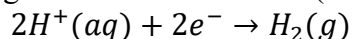
In summary, earth-abundant electrocatalysts were developed and characterized for water splitting (HER), reviews and perspectives were given for PEC water splitting, water remediation and electrochemically driven chlorination syntheses were performed.

## **Chapter II. Water Splitting Electrochemical Techniques**

## 2.1 Water Splitting – Experimental Techniques

Nanotechnology has emerging as an important tool to enhance catalysis.<sup>27,28</sup> In a reaction system, an easy way to study catalyst nanoparticles is by suspending them directly into a solution as a slurry.<sup>11</sup> In this case, there is limited control over the reaction kinetics occurring on the surface of the catalyst. Mainly, mixing, temperature, reactant concentrations and light (if photoactive) are the only controllable parameters; furthermore, conversion of the reaction products is the only indication of the catalyst performance. As an alternate to traditional methods of controlling reactions, electrochemistry can provide a rather immediate response to switching a reaction on and off while aiding in gathering insight into reaction kinetics and chemical pathways, selectivity and mechanisms. For use in electrochemistry, the catalytic particles need to be physically immobilized to a conductive surface, which is connected to a potentiostat that supplies electrons and record measurements. Therefore, some common catalytic systems will not be applicable or will need to be modified to perform electrocatalysis. In this work, I will examine immobilizing the electrochemically active catalysts (electrocatalysts) onto the surface of a Ti or FTO substrate (electrode). Furthermore, reactions are studied by applying a bias and collecting current from the electrocatalyst loaded electrode surface. For every electron produced or consumed at the interface, a current response is measured, correlating to an equivalent amount of reaction products formed.

Hydrogen Evolution Reaction (HER):



$$10\text{mA} = \frac{0.01\text{C}}{1\text{sec}} * \frac{1e^- \text{ charge}}{1.602 \times 10^{-19}\text{C}} * \frac{1\text{mol } e^-}{6.022 \times 10^{23}\text{ } e^-} * \frac{1\text{mol } H_2}{2\text{mol } e^-} \quad (2.1)$$

$$10\text{mA} = 3.11 \times 10^{-6}\text{ moles } H_2/\text{min}$$

The performance of an electrocatalyst material depends on a number of factors, therefore, multiple benchmarking preparation methods were conducted to determine an effective method to

determine accurate performances of the electrocatalysts. The WEs were coated with electrocatalyst suspension (10 mg/mL isopropanol) via drop casting followed by an annealing step to aid in substrate-catalyst adhesion.<sup>13,16,25</sup> Drop casting was performed on titanium (Ti) foil and fluorinated tin oxide (FTO) on glass substrates. In this study, the substrates were typically coated with relatively high loadings of electrocatalysts (110  $\mu\text{L}$  for Ti foil), due to the experimental performance measured providing less fluctuations and higher consistent values between electrocatalysts prepared on multiple WEs. For Ti foil, annealing with 5%  $\text{H}_2/\text{Ar}$  at 450  $^\circ\text{C}$  for 2 h is essential to reduce the surface  $\text{TiO}_2$  layer, which passivates the catalyst film from the electrode. For FTO, if any of the surface remains exposed during testing, the electrocatalyst layer will separate from the electrode. Electrodes were constructed from electrocatalyst modified substrates that were attached to a copper wire via silver paint, to make an ohmic contact and allow for electron transfer between the WE and the CE across the potentiostat, and then insulated by a two-part epoxy (9462 Hysol, Figure 2.1). Note, because of adhesion problems with the FTO surface, an amount of the two-part epoxy is used to strengthen the joint made by Ag paint and allowed to set before insulating the rest of the electrode. Again, electrode preparation methods may influence the behavior, stability and reproducibility of the electrode.

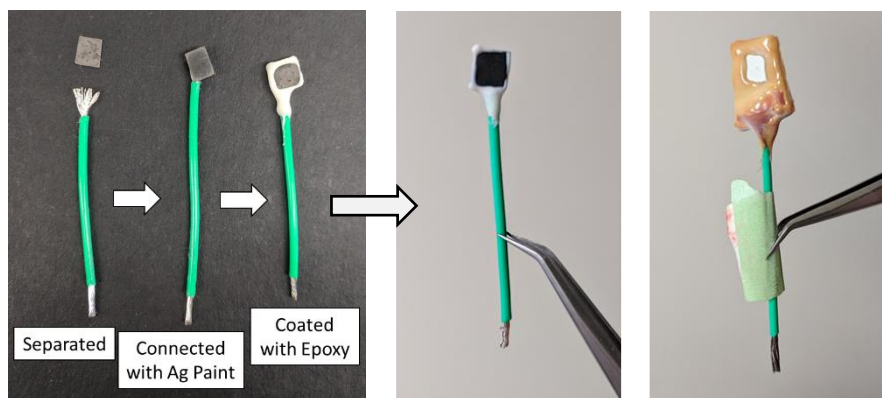


**Figure 2.1** A depiction of the electrode fabrication process to form a Ti substrate-based working electrode and an FTO on glass substrate-based working electrode with a deposited electrocatalyst and photocatalyst films, respectively.

Studying electrocatalysts under an applied bias can further provide insight into the fundamentals of catalysis.<sup>29</sup> Typically, the performance of an electrocatalyst is gained via a potentiostat (an instrument that measures and maintains current, potential, etc.) connected to a three-electrode cell (Figure 2.2), where chemical interactions are recorded at the working electrode (WE). The oxidative and reductive reactions on the surface of the electrodes are driven by an applied bias (potential, V), and for any given electrochemical reaction to occur on the WE, an opposing reaction needs to occur on the counter/auxiliary electrode (CE). The WE and CE each perform one half reaction, corresponding to an independent oxidation or reduction reaction. If current is not observed, neither half reaction is occurring at the working and counter electrodes, respectively. Consequently, when reactions are occurring on both electrodes, a current is observed which is considered to be directly proportional to the extent of reaction (Figure 2.2). The WE and CE work together, even though the catalytic being studied is on the WE. Since this holds true, the CE should be an ideal electrode to facilitate the corresponding half reaction and not hinder the

reaction being studied at the WE. The CE is considered ideal when acting as an electrocatalyst or by compensating possible kinetic limitations with a significantly larger area than the WE. For example, an over-dipped graphite rod can provide a similar performance as a Pt wire for the CE. Furthermore, the CE should have a greater surface area than the WE and reference electrode (REF), as to not limit the reaction kinetics on the WE and to make sure that current is not forced through the REF, respectively.<sup>29</sup> The REF is utilized to correct for variations in voltage and serve as a point of reference for the cell.

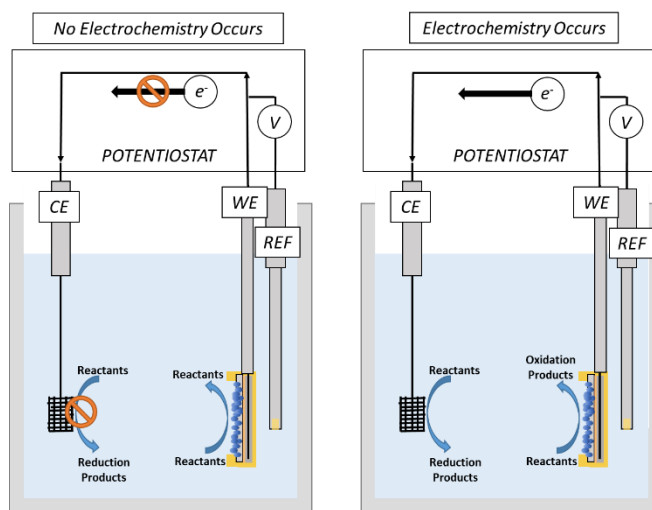


**Figure 2.2** Use of a potentiostat in electrochemical engineering: CE, WE, REF, are counter electrode, working electrode, reference electrode, respectively. The electrolysis of water occurs when electrons are supplied to the cathode to perform the HER (Equation 1.1) and removed from the anode to perform the OER (Equation 1.2). Here, the WE is depicted as an anode.

It is important to note that sacrificial agents are often used to facilitate the HER, lowering the over-potential required by replacing the OER with the decomposition of an alcohol, which subsequently has a more thermodynamically favorable redox potential, requiring less energy to produce hydrogen.<sup>30</sup> Small concentrations (e.g., mM level) of alcohols are enough to act as a

sacrificial agent and shift the system, therefore, a high purity electrolyte is needed to truly study the true water splitting half reactions and not various side reactions resulting from contaminants. Water splitting herein, is performed without any sacrificial agents to provide true performance.

If an electrochemical reaction is diffusion limited then fundamental studies can be performed to determine the non-diffusion-limited performance by utilizing a rotating disk electrode (RDE). However, water splitting is not a diffusion limiting process owing to reactants being present in excess and the use of significant pH levels. Therefore, stirring speeds have less impact on the water splitting half reactions other than clearing residual bubbles formed at the surface of the electrodes. A two-cell system can be utilized to compartmentalize electrochemical reactions at the WE and CE via a diffusion limited frit. This slows intermixing of oxidation and reduction reactants and products. Furthermore, the corresponding reactions may be chosen to help facilitate desired oxidation and reduction reaction or add an alternative value-added reaction.

Photocatalysts as a slurry suspension suffer in application because generation of both the oxidative and reductive products occur simultaneously on the surface of individual particles, which presents complications such as a higher probability of back reactions, a lower electron-hole separation probability, and the mixing of products requiring further separation. Furthermore, voltage and current across a particle cannot be easily measured. Therefore, photoelectrochemical (PEC) testing of photocatalysts as photoelectrodes, is suggested to separate the two half reactions and supply numerous benefits, including suppressing the back reaction of  $H_2$  and  $O_2$  to  $H_2O$ , the separation of the gaseous products simplified and the catalyst is immobilized for long term use. The experimental setup for solar PEC utilizes a potentiostat connected to an optically transparent three-electrode electrochemical cell irradiated by a light source.



### 2.1.1 Experimental Startup Procedure

Electrochemical analytical techniques were developed. Electrochemical measurements were performed by using a Gamry 5000P system. All measurements are conducted in 2 M KOH alkaline media using a three-electrode cell with alkaline/HgO (1 M NaOH) reference electrodes, with an over dipped graphite rod counter electrode. Polarization data was obtained at a sweep rate of 5 mV/s while rapidly stirring the solution with a magnetic stir bar. Long-term electrochemical stability measurements were performed by chronopotentiometry, by applying a constant overpotential current of  $-20 \text{ mA/cm}^2$  for an extended period of time, typically 10 hr. A clean Pt disc was run as a standard after the samples, to not contaminate the solution with Pt ions.

All of the potentials are reported against the reversible hydrogen electrode (RHE) by using the Nernst equation:

$$E_{RHE} = E_{Ag/AgCl} + E_{Ag/AgCl}^o + 0.05916 * pH \quad (2.2)$$

where  $E_{Ag/AgCl(1MKOH)}^o$ ,  $E_{Hg/HgO(1M NaOH)}^o$ , and  $E_{Hg/HgCl(sat. KCl)}^o$ , is 0.1976, 0.098, and 0.241 V at 25°C, respectively. The Nernst equation is utilized to calculate the potential window against the reference electrodes listed in specific electrolytes. For example, to find 0.0 V vs RHE in alkaline media (2 M KOH, pH 14),  $E_{Hg/HgO} = -0.926 \text{ V vs Hg/HgO}$ . 0.0 V vs RHE serves as the zero point where the HER is thermodynamically expected to initiate. Next, a maximum point should be calculated. 400 mV is considered a high overpotential and suffices for an upper limit for the active materials being tested. From the Nernst equation, the upper limit of the potential window is found to be,  $-1.326 \text{ V vs Hg/HgO}$ . Now voltage can be swept from the lower limit to the upper limit to form a polarization curve to monitor the HER reaction kinetics. The overpotential is calculated by

subtracting the thermodynamic redox potential from the potential at a given current density readily facilitating the reaction.

Reference electrodes are chosen to match reaction conditions where typically alkaline media utilizes an Hg/HgOH (1 M NaOH) and acidic media utilizes an SCE (Hg/HgCl, sat. KCl) or an Ag/AgCl (1–4.2 M KCl) reference electrode. For water splitting, common electrolytes are 2 M KOH  $\rightarrow$  pH = 14, and 0.5 M H<sub>2</sub>SO<sub>4</sub>  $\rightarrow$  pH = 0, which allow for good ionic conductivity and reaction mechanisms. Electrolytes of pH values, such as buffer solutions, not equal to 0 or 14 pH can be used, however, an added kinetic loss is created from the reactants having to be generated at the electrodes prior to reacting. Therefore, the true kinetics of the electrocatalysts are not measured at neutral pH values. The RHE can be experimentally determined by measuring the OCP with a clean Pt mesh electrode in electrolyte solution with hydrogen gas bubbled (however this was not performed in this work).

The Nernst equation is modified to calculate for the standard hydrogen electrode (SHE) as:

$$E_{RHE} = E_{Ag/AgCl} + E_{Ag/AgCl}^o \quad (2.3)$$

where  $E_{Ag/AgCl(1MKOH)}^o$ ,  $E_{Hg/HgO(1M NaOH)}^o$ , and  $E_{Hg/HgCl(sat. KCl)}^o$ , is still 0.1976, 0.098, and 0.241 V at 25°C, respectively. However, the SHE does not account for pH. Therefore, only the RHE is accounted for herein.

Again, three potential are of interest when setting up an electrochemical water splitting experiment: -0.4, 0.0, and 0.1 V vs RHE. Where -0.4 V is the maximum expected overpotential for lower performing samples, 0.0 V is the thermodynamic redox potential for the HER and the minimal potential expect, and 0.1 V is a non-faradic value where no reaction is expected to occur.

Non-faradaic means that if potential is cycled, any current response, i.e., reactions observed, are reversible. At a potential that produces hydrogen, a current response is observed only for the cathodic sweep indicating that the reaction is faradaic and irreversible.

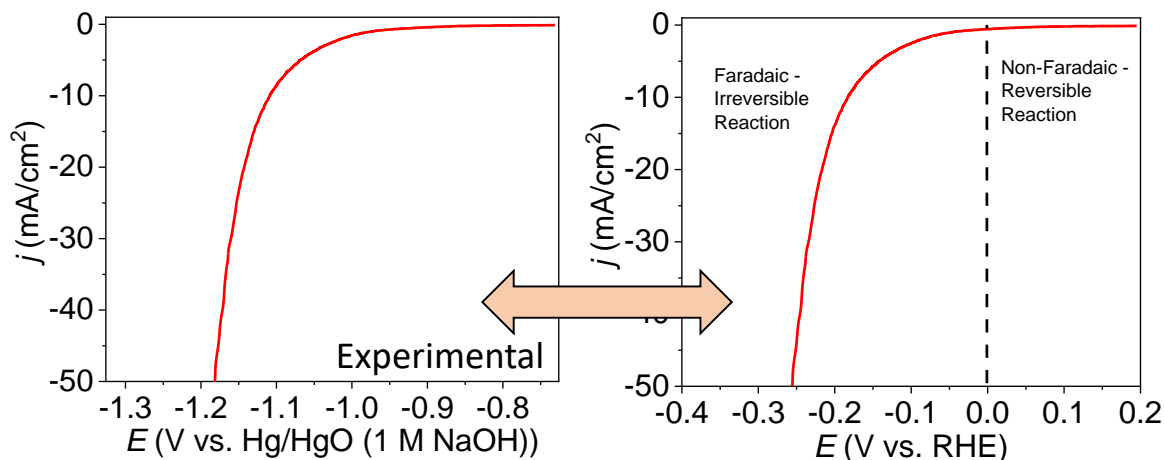


**Figure 2.3** Polarization curve highlighting the non-faradaic and faradaic regions of interest when determining the voltage window against V vs RHE and V vs Hg/HgO. The value for the thermodynamic value of the hydrogen evolution reaction is displayed with a dashed line. The figure compares polarization curve plotted against a reference electrode and then corrected to the RHE.

### 2.1.2 Data Analysis

The y-axis of the polarization curves (Figure 2.4) is current density, reported in literature as mA cm<sup>-2</sup>. The value for cm<sup>2</sup> is determined by the exposed nominal or geometric area of an electrode surface. For example, the Ti foil electrodes are cut and pressed to be 0.4 by 0.5 cm, giving a 0.2 cm<sup>2</sup> area. From a polarization curve of current density vs. potential, over-potentials

are extracted by taking the potential value at a given current density. Current densities of  $-10 \text{ mA cm}^{-2}$  and  $-20 \text{ mA cm}^{-2}$  are typical to report for a renewable-powered device application.

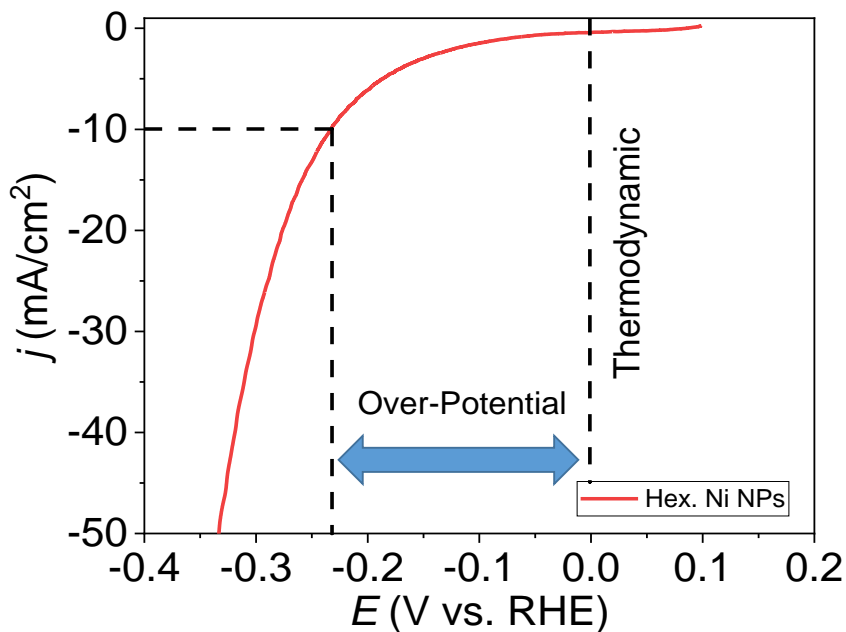


**Figure 2.4** Over-potentials at  $-10 \text{ mA cm}^{-2}$  are taken from the polarization curve of an electrocatalyst working electrode and subtracted by the thermodynamic value.

The kinetic limitations (over-potentials) for each electrocatalyst determine the hydrogen production efficiency. The total thermodynamic water splitting value of 1.23 V divided by 1.23 V plus the over-potential for the cathode, will give a cathodic efficiency, assuming 100% faradaic efficiency where all electricity is converted into moles of hydrogen. Furthermore, the efficiency of the cell is calculated as the thermodynamic value over the total energy input to obtain a specific current density. The total efficiency given by an power balance would be equivalent to the total power input to obtain hydrogen gas with a heating value of 286 kJ/mol H<sub>2</sub>, equation 2.1 multiplied by mV to obtain power, total efficiency of thermodynamic 1.23 V over total volts (dependent on the over-potentials of both electrodes), and an ideal PGM fuel cell to recover 70% efficiency back.

General efficiency requirements are less than approximately 150 and 350 mV over-potentials for the HER and the OER, respectively.<sup>3,31</sup>

A roughness factor of the surface of the electrodes can be approximated using a method adapted from determining an electrochemical double layer ( $C_{DL}$ , ECDL) capacity for an ECDL capacitor. An ECDL capacitor behavior is observed electrochemically by performing cyclic voltammetry (CV) across a non-faradic potential window, i.e, from 0.05 to 0.15 V vs RHE. The formula to calculate the electrochemical surface area (ECSA) from the ECDL is given here:

$$i_C = \nu C_{DL} \quad ; \quad ECSA = C_{DL}/C_s \quad (2.4)$$

where  $i_C$  is current,  $\nu$  is scan rate,  $C_s$  is general specific capacitance. The general specific capacitance is difficult to establish for non-ideal crystal alloys and is primarily a physic calculation performed for a specific material in a specific media. Research groups have given these values for similar electrocatalysts to Ni–Mo.<sup>3</sup> Nonetheless, the ECDL can be used to compare similar compositions as a *roughness factor* approximation, where the magnitude of the ECDL is directly proportional to the magnitude of the ECSA.  $C_{DL}$  is found by plotting  $i_C$  (the middle point of the cathodic and anodic sweeps) at multiple  $\nu$  (0.005, 0.010, 0.025, 0.050, 0.100, 0.200, 0.400, 0.800 V/s) and taking the slope. Furthermore, performing repeated CVs over a non-faradaic region acts to clean the active sites on the surface of the electrode of unreacted intermediates and products.

Ohmic correction on LSV data is performed by the Gamry Framework software via the current interruption method pre-experiment (Figure 2.6). The ohmic correction for  $iR$  drop matches the data collected from performing the current interruption method and determining ohmic drop experimentally post-experiment utilizing the  $V_{oc}$ .

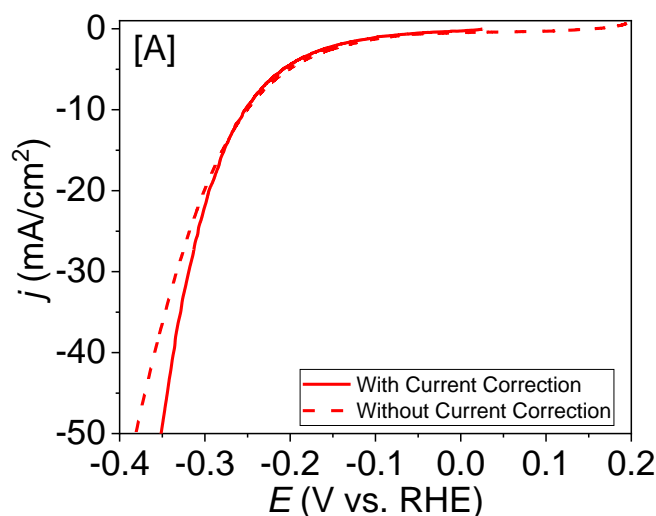


**Figure 2.6** An example polarization curve to show data with and without iR compensation.

The electrochemical mechanism for the HER on the surface of the working electrode can be determined by manipulating the polarization data to create Tafel plots (Figure 2.7). The polarization curves manipulated and plotted as over-potential vs  $\log(\text{current density})$  near a at a specific current density ( $-10 \text{ mA cm}^{-2}$ ). The linear portion at the specific current density is utilized to fit the Tafel equation given:

$$\eta = A \cdot \ln(i / i_0) \quad (2.5)$$

where  $\eta$  is the over-potential,  $A$  is the Tafel slope (V),  $i$  is the current density ( $\text{A/m}^2$ ), and  $i_0$  is the exchange current density ( $\text{A/m}^2$ ). The slope of the linear portion of the Tafel plots is the Tafel slope and the x-intercept of a line extrapolated from the Tafel equation gives the exchange current density. The Tafel slope indicates which rate determining mechanism is occur for the HER and the values are describes as either Tafel, Heyrovsky, and/or Volmer mechanisms at 30, 40, and 120 mV/dec, respectively.<sup>32,33</sup> If values are found between these, then the rate determining step is

assumed to be a combination of the respective mechanisms. The exchange current density describes the intrinsic rates of electron transfer between an analyte (i.e., 2 M KOH) and the conducting electrode. In general, the lower the Tafel slope, exchange current density, and over-potential yields the best electrocatalysts.

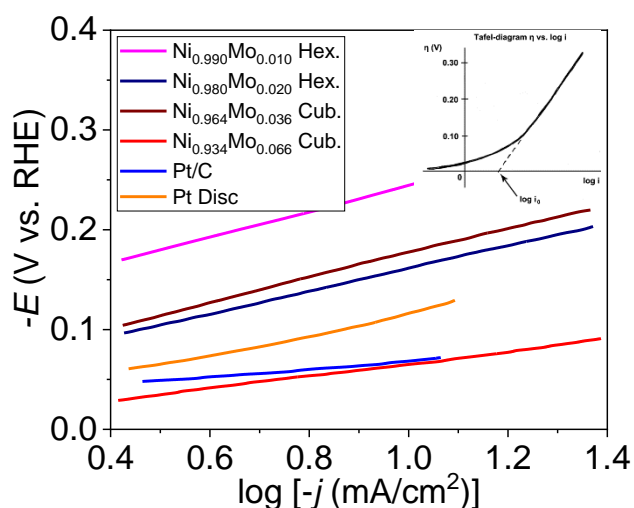


**Figure 2.7** Tafel plots for Pt-based electrocatalysts and Ni<sub>1-x</sub>Mo<sub>x</sub> alloy NP electrocatalysts in alkaline media from Chapter 3. The inlay describes how the linear portion is taken to be plotted separately and that it can be extrapolated to determine the exchange current densities of the catalysts.

The stability of HER electrocatalysts is important for any practical applications. As a conventional approach for *short-term stability*, a constant current density is galvanostatically maintaining to electrocatalyst working electrodes for 10 to 24 h at either  $-10$  and  $-20$  mA cm<sup>-2</sup> without ohmic correction. Polarization curves before and after stability testing are shown in Figure 2.8A. Figure 2.8B shows deviations in the recorded voltage over time. Any short-term stability test should retain  $\sim 95\%$  efficiency.

As an alternative to LSV polarization curves, stepping through different current densities ( $-2$ ,  $-5$ ,  $-10$ , and  $-20$  mA cm<sup>-2</sup>) and holding the current over short time period (0.5–3 min) can provide *short-term performance*.<sup>3</sup> However, this method is not as desirable as running LSV owing to the Tafel analysis cannot be performed,  $iR$  compensation has to be accounted for post-experiment, and it is not commonly reported.

Accelerated degradation study as a *long-term electrochemical stability* measurement can be conducted by cyclic voltammetric cycling from  $+0.005$  V to  $-0.140$  V without accounting for any uncompensated resistance. The upper limit changes based on the electrocatalyst, however,  $-0.140$  V is a strong approximation for an active electrocatalyst. Polarization curves would be taken initially and after 400 cycles. This method emphasizes a material that oxidizes irreversibly or dissolves into solution, potentially lowering stability for even some PGMs.

Overall, stability protocols should be developed in-depth for earth-abundant materials to obtain *true stability*, with a robust electrochemical cell and electrode design. The electrode and cell design should be similar to a water splitting electrolyzer (flow cell) that can run for a few hundred hours with a 75–90 % retention of efficiency and remain  $<150$  mV at  $-10$  mA/cm<sup>2</sup>. Ti foil electrodes would result in particle desorption from the surface after a certain number of hours, resulting in an increasing in over-potential due to the reduced irregular mass loading of the electrode. Therefore, Ti foil-based electrodes would struggle to give true stability after long periods of time.



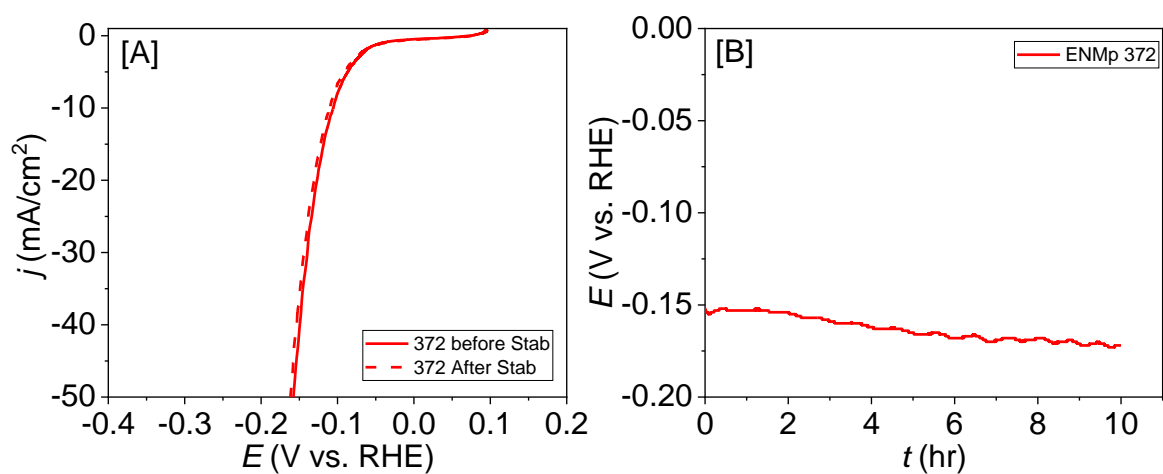


**Figure 2.8** Plots illustrating the stability of Ni<sub>1.87</sub>Mo<sub>0.13</sub>P NPs for alkaline HER. [A] The polarization curve before (solid line) and after (dashed line) 10 h of a constant applied current at  $-10 \text{ mA cm}^{-2}$ . [B] Change in over-potential per 10 h of  $-10 \text{ mA cm}^{-2}$ , applied without ohmic correction as seen in Chapter 4.

### 2.1.3 GAMRY FRAMEWORK

Experiment → Sequence Wizard

CV x 8 for roughness factor and gentle cleaning of active sites

CV 3 cycles at each scan rate

RHE = -0.4 V

SCE = -0.641

Initial -0.091

Limit1 -0.091

Limit2 -0.191

Final -0.091

Scan rate 5, 10, 25, 50, 100, 200, 400, 800

Step size 2

IRCOMP Current Interruption method

User Prompt

Turn on Stirring and reinsert Ar bubbling

LSV x 4 for polarization curves, LSV3 not iR compensated

Initial -0.041

Final -0.641

Scan rate 5

Step size 2

CP x 1 for stability

-0.002 A for -10 mA/cm<sup>2</sup> or -0.004 A for -20 mA/cm<sup>2</sup>

36000 sec for 10 hours

Stop

Reopen the sequence wizard and run the same sequence without CP to get performance after stability

## 2.2 Material Characterization

- Powder X-ray diffraction (PXRD) patterns were collected on a PANalytical MPD X'pert Pro diffractometer operating at 40 kV and 40 mA, equipped with Cu K $\alpha$  radiation ( $\lambda = 1.5418 \text{ \AA}$ ) and calibrated with a Si standard. Scans are performed over a  $2\theta$  range of 15-85°. XRD patterns are analyzed via the associated software package.

- Scanning electron microscope (SEM, Hitachi SU-70 FE-SEM) at 5 kV acceleration voltage under a vacuum atmosphere and a working distance of 5 mm was utilized to examine the morphology of materials.
- Transmission electron microscopy (TEM) images can be collected. Transmission electron microscopy (TEM) images were acquired using a Zeiss Libra 120 TEM microscope equipped with a Gatan ultrascan 4000 camera operating at 120 kV; or a JOEL JEM-1400 PLUS TEM microscope equipped with a Gatan OneView digital camera operating at 120 kV. Samples were prepared by drop casting 10  $\mu$ L of alloy NPs dispersed in toluene onto carbon-coated Cu grids, followed by solvent evaporation.
- High-resolution TEM images were recorded on a FEI Model Titan 8300 electron microscope equipped with a Gatan Model 794 multiscan camera operating at 300 kV located at UVA. Samples were prepared by drop casting 10  $\mu$ L of alloy NPs dispersed in toluene onto carbon-coated Cu grids, followed by solvent evaporation.
- Energy dispersive spectra (EDS) were recorded using a Hitachi Model FE-SEM Su-70 scanning electron microscope (SEM) operating at 20 keV with an in-situ EDAX detector. The powder samples were pressed onto an Al stub using double-sided carbon tape purchased from Ted Pella Inc. The atomic percentages were obtained from the EDS analysis of multiple individually prepared samples, and the averaged values were obtained from 5 individual measurements for each sample.
- The composition of alloys was investigated by a Varian VISTA-MPX inductively coupled plasma–optical emission spectrometer (ICP-OES). The samples were digested in acids (HCl: HNO<sub>3</sub> = 3: 1) for ICP-OES, which were further diluted with milli-Q filtered water prior to analysis.

- A Thermofisher ESCALAB 250 instrument equipped with Al K $\alpha$  radiation was utilized to record X-ray photoelectron spectra (XPS) of alloy NPs. The powder samples were drop-casted onto Ti foils and annealed in 5% H<sub>2</sub>/Ar gas mixture at 450 °C for 2 h prior to XPS. High-resolution spectra were collected with a pass energy of 26.00 eV, 20 ms per step, and multiple sweeps depending on the counts observed for the Mo3d and Ni2p regimes.
- Fourier Transform Infrared Spectroscopy (FT-IR) was used to observe surfactants. A Nicolet 670 FT-IR equipped with a single reflection diamond ATR attachment was employed to collect infrared spectra of the NPs.

## **Chapter III. Reduction of Water – Crystal Structure and Composition-Dependent Electrocatalytic Activity of Ni-Mo Nanoalloys for Water Splitting to Produce Hydrogen**

Adapted from *ACS Appl. Energy Mater.* **2019**, 2, 10, 7112-7120

DOI: 10.1021/acsaem.9b01043

Electrocatalytic water splitting presents an exciting opportunity to produce environmentally benign fuel to power human activities and reduce reliance on fossil fuels. Transition metal nanoparticles (NPs) and their alloys are emerging as promising candidates to replace expensive platinum group metal (PGM) catalysts. Herein, we report the synthesis of distinct crystal phases and compositions of  $\text{Ni}_{1-x}\text{Mo}_x$  alloy NPs as low-cost, earth-abundant electrocatalysts for the hydrogen evolution reaction (HER) in alkaline medium. Phase-pure cubic and hexagonal Ni and  $\text{Ni}_{1-x}\text{Mo}_x$  alloy NPs, with sizes ranging from 18–43 nm and varying Mo composition (~0–11.4%), were produced by a low-temperature colloidal chemistry method. As-synthesized NPs show spherical to polygonal morphologies and a systematic shifting of Bragg reflections to lower  $2\theta$  angles with increasing Mo, suggesting the growth of homogeneous alloys. XPS analysis indicates the dominance of metallic Ni(0) and Mo(0) species in the core of the alloy NPs as well as the presence of higher valent  $\text{Ni}^{n+}$  and  $\text{Mo}^{n+}$  surface species, stabilized by surfactant ligands. The cubic alloys exhibit significantly higher HER activity in comparison to the hexagonal alloys. For a current density of  $-10 \text{ mA/cm}^2$ , the cubic alloys demonstrate over-potentials of  $-62$  to  $-177 \text{ mV}$  compared to  $-162$  to  $-242 \text{ mV}$  for the hexagonal alloys. The over-potentials of cubic alloys are comparable to the commercial Pt-based electrocatalysts for which the over-potentials range from  $-68$  to  $-129 \text{ mV}$  at  $-10 \text{ mA/cm}^2$ . In general, a decrease in over-potential and an increase in HER activity was observed with increasing concentration of Mo (up to 6.6%) for the cubic alloys. The cubic  $\text{Ni}_{0.934}\text{Mo}_{0.066}$  alloy NPs exhibit the highest activity as alkaline electrocatalysts.

### 3.1 INTRODUCTION

Increasing energy demands and growing environmental concerns are causing concerns over the use of fossil fuels.<sup>1,26</sup> Material science solutions for current energy technologies are being

heavily researched for our society to help transition into the large scale implementation of renewable energies.<sup>13</sup> Renewable hydrogen as an energy carrier and chemical reagent is a foreseeable energy supplement to fossil fuels. Promising methods to produce hydrogen include electrochemical water splitting utilizing renewable electricity or direct water splitting via photocatalysis, both of which will require inexpensive high-performance electrocatalysts.<sup>32</sup>

Current state-of-the-art electrocatalysts and photocatalysts for water splitting reactions typically incorporate platinum group metals (PGMs) as the primary or secondary catalyst(s) for the hydrogen evolution reactions (HER). The single-element cathodic earth-abundant electrocatalysts, such as Ni, Mo, Co, W, and Fe, typically exhibit high over-potentials (>150 mV) and low stability (<48 h) compared to PGM catalysts (~70 mV and >100 h, respectively).<sup>3,34</sup> To improve HER performance, synergistic effects of alloying earth-abundant metals are being studied.<sup>12,13,35–37</sup> Specifically, the binding energies of binary alloys can be tuned by manipulating the atomic ratio to achieve an optimal electrocatalyst surface affinity for the reactants and products. The correlation of exchange current densities to metal-hydrogen bond strengths for electrocatalysts (volcano plots) indicate a goldilocks region for the surface affinity of electrocatalysts.<sup>4,12,13,38</sup> To further aid with the HER, the growth of nanostructured catalysts has been utilized to produce high surface area, high energy faceted crystals, and unique crystal phases that are typically inaccessible as bulk materials.<sup>13,39</sup> Both Ni and Mo are earth-abundant and significantly less expensive than PGMs (Pt, Mo, and Ni are about \$29,000/kg, \$26/kg, and \$9/kg, respectively).<sup>40</sup> However, prior reports on Ni<sub>1-x</sub>Mo<sub>x</sub> alloys rarely referenced the crystal phases and to complicate this further, stoichiometric quantities are often described instead of true crystal phases.<sup>2,41</sup> For instance, the stoichiometric ratios reported for Ni<sub>1-x</sub>Mo<sub>x</sub> alloys have been ascribed to mixtures of Ni, Mo, Ni<sub>4</sub>Mo, and Ni<sub>3</sub>Mo alloys and/or amorphous materials.<sup>3,35,41–43</sup> Thus, a systematic study on crystal

structure or phase-dependent HER activity of  $\text{Ni}_{1-x}\text{Mo}_x$  alloys has not been properly elucidated. Electrocatalytic water splitting can be carried out in both acidic and alkaline media.<sup>2,4,26,34,37,44,45</sup> Acidic media are compatible with proton exchange membranes developed by the fuel cell industry and usually provide a higher energy conversion efficiency.<sup>3,13,15,22,32,44-47</sup> The differences in half reaction mechanisms and charge carrier mobilities at both electrode interfaces, in acidic and alkaline media, suggest higher HER activity under acidic conditions.<sup>22</sup> Recent studies contradict this trend and show high HER performance in alkaline medium.<sup>34,48-51</sup> For instance, an over-potential of 30 mV was observed for an electrodeposited Ni-Mo film in 1 M NaOH at -10 mA/cm<sup>2</sup>.<sup>34</sup> Furthermore, transition metal-based catalysts are thought more stable in alkaline media, owing to an alternate hydrogen formation mechanism and bulkier OH<sup>-</sup> ion diffusion.<sup>22</sup> Non-PGM transition metal electrocatalysts, including Ni, Mo, and Cu, have a noted low stability in acidic media.<sup>3</sup> For example, the over-potential of an electrodeposited Ni-Mo film in an acidic medium increased by ~50 mV after 20 h of constant polarization, and when the potential was cycled from -0.3 to 0.9 V vs. RHE, a full degradation and dissolution was observed after 2000 cycles.<sup>3,34,41</sup> Therefore, alkaline medium can provide the benefits of added stability and plausible high performance for  $\text{Ni}_{1-x}\text{Mo}_x$  NPs as HER catalysts. However, a systematic study on the HER activity of distinct crystal phases and compositions of  $\text{Ni}_{1-x}\text{Mo}_x$  alloy NPs has yet to be elucidated.

Herein, a colloidal synthesis method was developed to produce phase-pure cubic and hexagonal  $\text{Ni}_{1-x}\text{Mo}_x$  alloy NPs with varying compositions of Mo ( $x = 0-11.4\%$ ) for alkaline HER. The crystal structures and compositions of the  $\text{Ni}_{1-x}\text{Mo}_x$  alloy NPs were tuned by varying the reaction temperature, heating rate, and concentration of the precursors and octadecene (ODE) and oleylamine (OLA) surfactants and solvents. It was found that the cubic alloys show higher catalytic activity for HER when compared to the hexagonal alloys. In general, HER activity increases with



increasing Mo content up to 6.6% for the cubic alloys, followed by a decrease at 8.7% and 11.4%. The cubic  $\text{Ni}_{0.934}\text{Mo}_{0.066}$  alloy NPs displayed the highest activity as alkaline HER electrocatalysts, rivalling commercial PGM catalysts. This work further explores variations in the surface species of the electrocatalysts to gain a fundamental understanding of what material physical properties (e.g. crystal structure, composition, morphology, and surface states) lend to modification of the HER performance.

## 3.2 EXPERIMENTAL SECTION

**3.2.1 Materials.** Nickel acetylacetonate ( $\text{Ni}(\text{acac})_2$ ), molybdenum hexacarbonyl ( $\text{Mo}(\text{CO})_6$ ), Octadecene (ODE; 90%) and KOH (reagent grade, 90%) were purchased from Acros Organics. Oleylamine (OLA primary amine, 70%), Pt on graphitized carbon (Pt/C, 20 wt.%), and Ti foil (thickness 0.25 mm, 99.7%) were purchased from Sigma-Aldrich. Graphite rods (6.15 mm x 102 mm, 99.9995%) were purchased from Alfa Aesar. Isopropyl alcohol (certified ACS Plus) was purchased from Fisher Scientific. PELCO colloidal Ag paint was purchased from Ted Pella Inc. Henkel Loctite Hysol 9462 epoxy adhesive was purchased from Ellsworth Adhesives. PTFE insulated stranded Ag-plated Cu wire (Chemical-Resistant Wire) was purchased from McMaster-Carr. A Pt (2 mm disc) working electrode and a Hg/HgO reference electrode filled with 1 M NaOH solution were purchased from CH Instruments. OLA and ODE were dried at 120 °C under vacuum for 3h prior to use. Methanol and toluene were dried over molecular sieves and Na metal, respectively, and distilled under  $\text{N}_2$  prior to use. All other chemicals were used as received.

**3.2.2 Synthesis of Cubic  $\text{Ni}_{1-x}\text{Mo}_x$  Alloy NPs.** In a typical synthesis of cubic  $\text{Ni}_{1-x}\text{Mo}_x$  alloy NPs, appropriate amounts of  $\text{Ni}(\text{acac})_2$  and  $\text{Mo}(\text{CO})_6$  were mixed in a 50 mL flask with 10 mL OLA surfactant inside a nitrogen glove box. This mixture was sealed under argon, attached

to a Schlenk line, and degassed at 120 °C for 60 min to produce a homogeneous green colored solution. Then, the reaction mixture was flushed with argon, and the temperature was raised to 230–250 °C (at a rate of ~5°C per min) and heated for additional 30 min to produce a black colored solution of cubic Ni<sub>1-x</sub>Mo<sub>x</sub> alloy NPs. Alloy NPs with varying elemental compositions were synthesized by varying the molar ratios of Ni(acac)<sub>2</sub>: (Mo(CO)<sub>6</sub>) as illustrated in Table 3.1. Phase-pure cubic Ni NPs were produced at 230 °C with no use of Mo(CO)<sub>6</sub>.

**3.2.3 Synthesis of Hexagonal Ni<sub>1-x</sub>Mo<sub>x</sub> Alloy NPs.** In a typical synthesis of hexagonal Ni<sub>1-x</sub>Mo<sub>x</sub> alloy NPs, appropriate amounts of Ni(acac)<sub>2</sub> and Mo(CO)<sub>6</sub> were mixed with 1 mL of OLA and 7 mL of ODE in a 50 mL round bottom flask under nitrogen. This mixture was sealed under argon, attached to a Schlenk line, and degassed at 120 °C for 60 min to produce a homogeneous green color solution. Then, the mixture was flushed with argon, and the temperature was raised to 300 °C (at a rate of ~8°C per min) and heated for 30 min to produce hexagonal Ni<sub>1-x</sub>Mo<sub>x</sub> nanoalloys. The elemental compositions of the hexagonal alloy NPs were varied by changing the molar ratios of Ni(acac)<sub>2</sub>: (Mo(CO)<sub>6</sub>) as shown in Table 3.1. Phase-pure hexagonal Ni NPs were produced at 300 °C with no use of Mo(CO)<sub>6</sub>.

**Table 3.1** Moles of Ni(acac)<sub>2</sub> and Mo(CO)<sub>6</sub>, volumes of OLA and ODE surfactant and solvents, and growth temperatures used in the synthesis of Ni<sub>1-x</sub>Mo<sub>x</sub> alloy NPs with varying atomic compositions and crystal structures.

| Sample Name <sup>a</sup>                | Crystal Structure | Ni(acac) <sub>2</sub> (mmol) | Mo(CO) <sub>6</sub> (mmol) | OLA (mL) | ODE (mL) | Growth Temperature (°C) |
|---|-------------------|------------------------------|----------------------------|----------|----------|-------------------------|
| Ni                                      | Cubic             | 0.500                        | 0.000                      | 10       | 0        | 230                     |
| Ni <sub>0.913</sub> Mo <sub>0.087</sub> | Cubic             | 0.400                        | 0.100                      | 10       | 0        | 230                     |
| Ni <sub>0.934</sub> Mo <sub>0.066</sub> | Cubic             | 0.375                        | 0.125                      | 10       | 0        | 230                     |
| Ni <sub>0.886</sub> Mo <sub>0.114</sub> | Cubic             | 0.350                        | 0.150                      | 10       | 0        | 230                     |
| Ni <sub>0.989</sub> Mo <sub>0.011</sub> | Cubic             | 0.450                        | 0.050                      | 10       | 0        | 250                     |
| Ni <sub>0.964</sub> Mo <sub>0.036</sub> | Cubic             | 0.400                        | 0.100                      | 10       | 0        | 250                     |
| Ni <sub>0.982</sub> Mo <sub>0.018</sub> | Cubic             | 0.350                        | 0.150                      | 10       | 0        | 250                     |
| Ni                                      | Hexagonal         | 0.500                        | 0.000                      | 1        | 7        | 300                     |
| Ni <sub>0.990</sub> Mo <sub>0.010</sub> | Hexagonal         | 0.450                        | 0.050                      | 1        | 7        | 300                     |
| Ni <sub>0.980</sub> Mo <sub>0.020</sub> | Hexagonal         | 0.400                        | 0.100                      | 1        | 7        | 300                     |
| Ni <sub>0.985</sub> Mo <sub>0.015</sub> | Hexagonal         | 0.375                        | 0.125                      | 1        | 7        | 300                     |

<sup>a</sup>Elemental compositions of Ni and Mo were investigated by SEM-EDS analysis of multiple individually prepared samples and average values are presented.

**3.2.4 Isolation and Purification of NPs.** After synthesis, the reaction mixture was promptly cooled using compressed air until the temperature reached ~80 °C. The mixture was transferred into a centrifuge tube and ~5 mL of toluene was added, followed by ~20 mL methanol. The mixture was centrifuged at 4000g for 5 min to collect a black color precipitate of

alloy NPs. The alloy NPs were purified by redispersion and precipitation (3–5 times) in toluene and methanol, respectively.

**3.2.5 Physical Characterization.** Powder X-ray diffraction (PXRD) patterns of alloy NPs were recorded using a PANalytical X'pert PRO equipped with Cu K $\alpha$  ( $\lambda = 1.5418 \text{ \AA}$ ) radiation and calibrated with a Si standard. Transmission electron microscopy (TEM) images were acquired using a Zeiss Libra 120 TEM microscope equipped with a Gatan ultrascan 4000 camera operating at 120 kV. High-resolution TEM images were recorded on a FEI Model Titan 8300 electron microscope equipped with a Gatan Model 794 multiscan camera operating at 300 kV. Samples were prepared by drop casting 10  $\mu\text{L}$  of alloy NPs dispersed in toluene onto carbon-coated Cu grids, followed by solvent evaporation. A Thermofisher ESCALAB 250 instrument equipped with Al K $\alpha$  radiation was utilized to record X-ray photoelectron spectra (XPS) of alloy NPs. The powder samples were drop-casted onto Ti foils and annealed in 5% H<sub>2</sub>/Ar gas mixture at 450 °C for 2 h prior to XPS. High-resolution spectra were collected with a pass energy of 26.00 eV, 20 ms per step, and multiple sweeps depending on the counts observed for the Mo3d and Ni2p regimes. Energy dispersive spectra (EDS) were recorded using a Hitachi Model FE-SEM Su-70 scanning electron microscope (SEM) operating at 20 keV with an in-situ EDAX detector. The samples were adhered onto an Al stub using double-sided carbon tape purchased from Ted Pella Inc. The atomic percentages of Ni and Mo were obtained from the EDS analysis of multiple individually prepared samples, and the averaged values were obtained from 5 individual measurements for each sample. The composition of the alloys were also investigated by a Varian VISTA-MPX inductively coupled plasma–optical emission spectrometer (ICP-OES). The samples were digested in acids (HCl: HNO<sub>3</sub> = 3: 1) for ICP-OES, which were further diluted with milli-Q filtered water prior to analysis.

**3.2.6 Fabrication of Working Electrodes.** The HER electrodes were fabricated by drop-casting colloidal suspensions of Ni<sub>1-x</sub>Mo<sub>x</sub> alloy NPs or commercial Pt/C catalyst dispersed in isopropyl alcohol onto Ti foil substrates. The Ti foils were cut into square pieces (~0.2 cm<sup>2</sup>), pressed flat, and sonicated in 1 M HCl and 40% H<sub>2</sub>O<sub>2</sub> (1:1, v:v) solution for 15 min. A mixture of acetone and ethanol (1:1, v:v) was then used to clean the Ti foils via sonication for 10 min, followed by additional 10 min sonication in Milli-Q water (18 Ω). The Ni<sub>1-x</sub>Mo<sub>x</sub> and Pt/C catalyst inks were produced by weighing appropriate amounts of alloy NPs or Pt/C and suspending in isopropyl alcohol (10 mg/mL) via sonication for 30 min. Then, 10 μL aliquots of catalyst inks were drop-casted onto the clean Ti foil substrates, incrementally to produce a visible coating (~100 μL total). Each aliquot was allowed to dry in air prior to subsequent addition. The electrocatalyst-coated Ti foils were then annealed at 450 °C for 2 h in 5% H<sub>2</sub>/Ar. The working electrodes were prepared by connecting the annealed substrate to an insulated Cu wire. Enough insulation was stripped to allow for an ohmic contact. Ag paint was then utilized to connect the back of the Ti substrate to the bare Cu wire. Finally, a two-part epoxy was applied to insulate the electrode, leaving the electrocatalytic active area on the front of the Ti substrate exposed (Figure 3.1). The epoxy was allowed to dry for ~5 h before use.

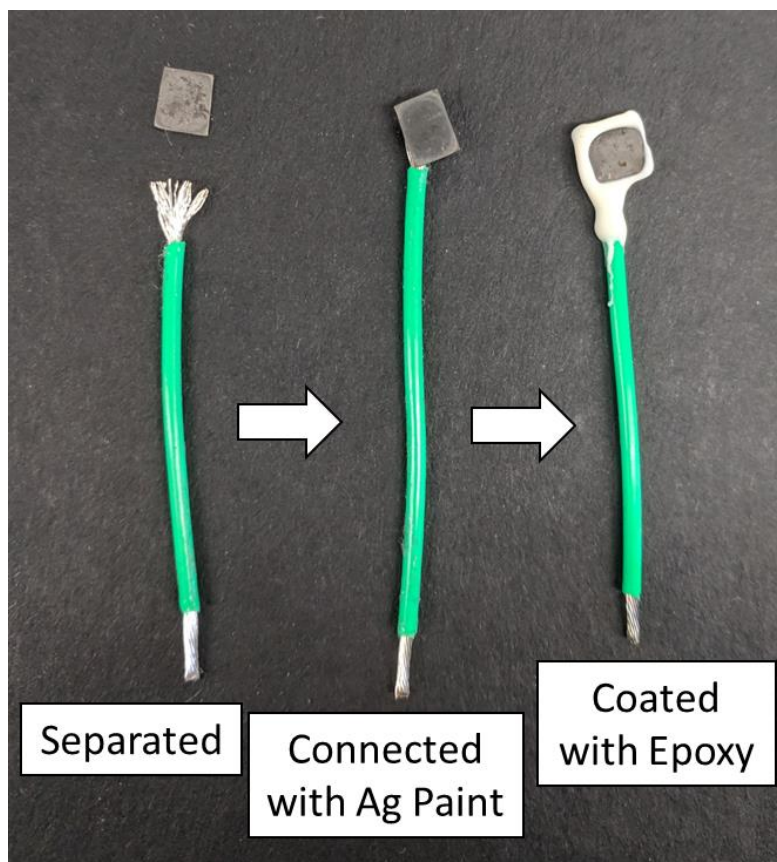


**Figure 3.1** A depiction of the electrode fabrication process to produce  $\text{Ni}_{1-x}\text{Mo}_x$  alloy NP working electrodes. The alloy NPs drop-casted on Ti substrates are annealed at 450 °C under 5%  $\text{H}_2/\text{Ar}$  atmosphere, attached to an insulated Cu wire using silver paint, and further coated with epoxy to template the electrodes.

**3.2.7 Electrochemical Measurements.** The performance of  $\text{Ni}_{1-x}\text{Mo}_x$  alloy NPs for HER was investigated by linear sweep voltammetry (LSV) using a Gamry Interface 5000P galvanostat. All electrochemical measurements were conducted in a conventional three-electrode cell at room temperature with an alkaline electrolyte solution (2 M KOH) prepared from Milli-Q-filtered water. The electrolyte was purged with high purity  $\text{N}_2$  prior to and during data acquisition. The  $\text{Ni}_{1-x}\text{Mo}_x$

alloy NP coated Ti foil electrodes and an over-dipped graphite rod were used as the working and counter electrodes, respectively. The potentials of the working electrodes were recorded against an Alkaline/HgO (1 M NaOH) reference electrode. The polarization data were obtained for each electrocatalyst by sweeping the potential from -0.798 to -1.398 V vs Hg/HgO at a sweep rate of 5 mV s<sup>-1</sup> under rapid stirring. The built-in resistance correction via a current interruption method was utilized on the Gamry Interface 5000P to obtain the polarization data. Chronopotentiometry was used to investigate the stability of Ni<sub>1-x</sub>Mo<sub>x</sub> alloy NP electrodes. The voltage was recorded over time at a constant current density of -20 mA/cm<sup>2</sup>, agitation (300 rpm), and nitrogen bubbling.

### **3.3 RESULTS AND DISCUSSION**

#### **3.3.1 Synthesis of Ni<sub>1-x</sub>Mo<sub>x</sub> alloy NPs**

Ni<sub>1-x</sub>Mo<sub>x</sub> alloy NPs with cubic and hexagonal structures and distinct elemental compositions were produced by thermal decomposition of Ni(acac)<sub>2</sub> and Mo(CO)<sub>6</sub> in alkylamine (OLA) and alkene (ODE) surfactant/solvent mixtures at 230–300 °C. The growth of different crystal phases is governed by the concentration of OLA/ODE ligands, heating rate, and reaction temperature. In our experiments, phase-pure cubic alloy NPs were produced when OLA is used as both the surfactant and solvent with no use of ODE at 230–250 °C, whereas phase-pure hexagonal alloys were obtained in ODE with minimal amount of OLA at 300 °C. It is assumed that at high concentration of OLA, the large excess of alkylamines passivate the alloy nuclei surface, slowing down the growth, and producing thermodynamically stable cubic Ni<sub>1-x</sub>Mo<sub>x</sub> alloys.<sup>52</sup> Upon introduction of ODE (>35–60% of total volume), Ni<sub>1-x</sub>Mo<sub>x</sub> alloy NPs consisting of both cubic and hexagonal phases were produced. The decreased concentration of OLA reduces the amount of alkylamines that passivate the alloy nuclei surface, promoting the growth of mixed phase alloys.<sup>53</sup>

In contrast, phase-pure hexagonal alloy NPs were produced in reactions performed with large excess of alkenes (ODE, 70–80% of the total volume). It is likely that high reaction temperature and significantly low concentrations of OLA facilitate the rapid decomposition of Ni/Mo precursors into hexagonal nuclei and subsequent growth of hexagonal alloys.<sup>28</sup> It should be noted that high temperature ( $\geq 300$  °C) along with rapid growth of alloy nuclei are essential for the synthesis of phase-pure hexagonal  $\text{Ni}_{1-x}\text{Mo}_x$  alloys, whereas the use of OLA only at 300 °C resulted in mix-phased alloys.

It is important to note that the concentration of Ni and Mo precursors and growth time have no effect on the resultant crystal structure, but rather affect the composition and size-dispersity of  $\text{Ni}_{1-x}\text{Mo}_x$  alloys. In general, lower temperature and higher Mo concentrations resulted in larger, polydispersed alloy NPs whereas higher temperature and lower Mo concentrations consistently produced smaller, more uniform alloy NPs. The atomic composition of the alloy is also dependent on the reaction temperature. At low temperature (230 °C), more Mo (up to 11.4%) can be incorporated into cubic Ni crystals whereas at high temperature (250–300°C) significantly low Mo (~1–3.6%) is incorporated into both cubic and hexagonal Ni crystals. In addition,  $\text{Mo}(\text{CO})_6$  exhibits a lower reactivity than  $\text{Ni}(\text{acac})_2$ , therefore alloy NPs show low Mo incorporation into both crystal phases.<sup>54</sup> However, by manipulating the growth temperature and the concentration of alkyl and alkylamine ligands, phase-pure hexagonal and cubic  $\text{Ni}_{1-x}\text{Mo}_x$  alloy NPs, displaying low Mo concentrations (*i.e.*  $x = \sim 1-11.4\%$ ), can be reproducibly produced.

PXRD patterns of  $\text{Ni}_{1-x}\text{Mo}_x$  alloys produced at 230–250 °C suggest that they retain the face centered cubic (fcc) structure of Ni and a shift in diffraction patterns to lower  $2\theta$  angles with increasing Mo ( $x = 0.011-0.066$ ), consistent with the expansion of fcc Ni by larger Mo.<sup>43</sup> The diffraction patterns of cubic alloys show three characteristic Bragg reflections, which can be



indexed to (111), (200), and (220) planes of cubic Ni-Mo (Figure 3.2A). In contrast, the diffraction patterns of  $\text{Ni}_{1-x}\text{Mo}_x$  alloys produced at 300 °C show the hexagonal crystal structure, with six pronounced reflections originating from (100), (002), (101), (102), (110), and (103) planes. A systematic shift in diffraction patterns to lower  $2\theta$  angles with increasing concentration of the Mo is also evident in the hexagonal alloys, specifically for  $x = 0.012$  and  $0.015$  compositions. However, cubic  $\text{Ni}_{0.913}\text{Mo}_{0.087}$  and hexagonal  $\text{Ni}_{0.981}\text{Mo}_{0.019}$  alloy NPs do not follow this trend likely because of minor hexagonal and cubic impurities present in those samples, respectively (Figure 3.2). The elemental compositions of cubic and hexagonal alloys, obtained from SEM/EDS analysis, indicate Ni: Mo atomic ratios of 99.0–88.6%: 1.0–11.4% (Table 3.3). The composition analysis via ICP-OES shows a similar trend in the Mo concentration, in agreement with EDS (Table 3.2). However, a larger difference between the nominal molar ratio and experimental ratio of Ni: Mo was noted, which we attribute to limited solubility of Mo atoms in both cubic and hexagonal Ni crystals.

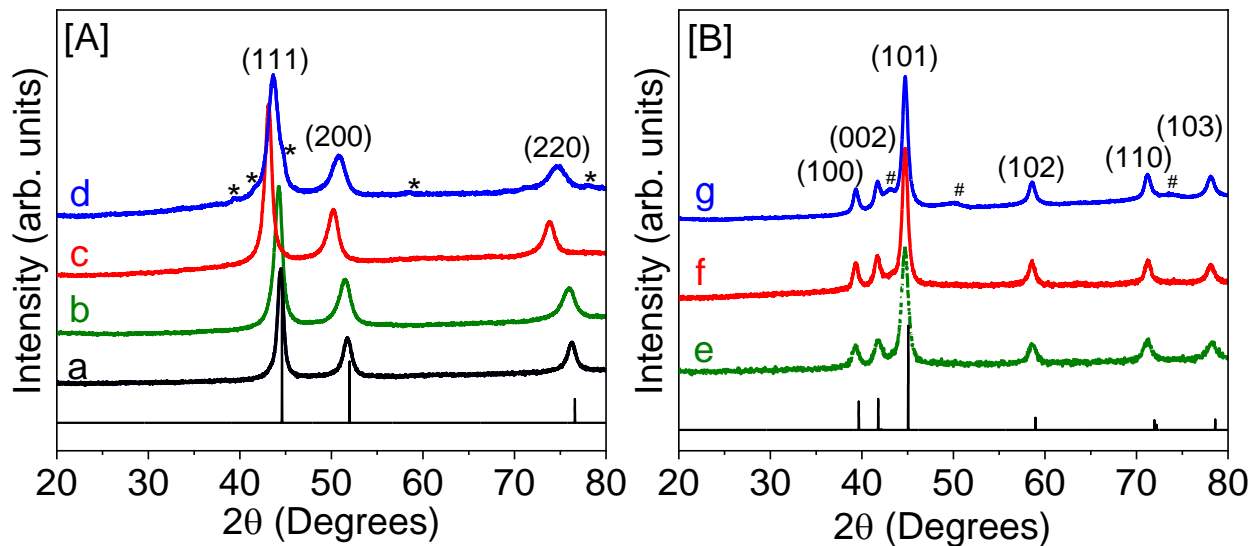


**Figure 3.2** Powder X-ray diffraction patterns of [A] cubic and [B] hexagonal  $\text{Ni}_{1-x}\text{Mo}_x$  alloy NPs produced with varying Mo concentrations: (a)  $x = 0.011$ , (b)  $x = 0.036$ , (c)  $x = 0.066$ , (d)  $x = 0.087$ , (e)  $x = 0.012$ , (f)  $x = 0.015$ , and (g)  $x = 0.019$ . The vertical gray line shown in A corresponds to cubic Ni structure (JCPDS # 01-070-0989) whereas the vertical gray line shown in B represents hexagonal Ni (JCPDS # 01-089-7129) structure. The diffraction peaks corresponding to hexagonal and cubic  $\text{Ni}_{1-x}\text{Mo}_x$  impurities are shown in \* and #, respectively.

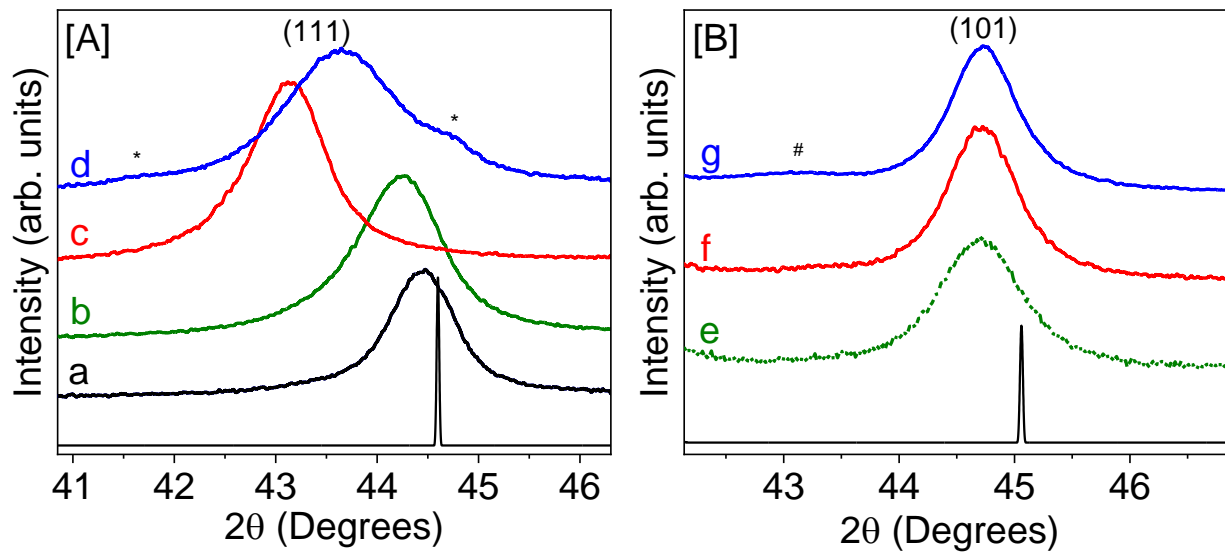


**Figure 3.3** Powder X-ray diffraction patterns (zoomed in to display the most intense peak) of [A] cubic and [B] hexagonal  $\text{Ni}_{1-x}\text{Mo}_x$  alloy NPs with varying Mo concentration: (a)  $x = 0.011$ , (b)  $x = 0.036$ , (c)  $x = 0.066$ , (d)  $x = 0.087$ , (e)  $x = 0.012$ , (f)  $x = 0.015$ , and (g)  $x = 0.019$ . The vertical gray line shown in A corresponds to (111) plane in cubic Ni structure (JCPDS # 01-070-0989) whereas the vertical gray line shown in B represents (101) plane in hexagonal Ni (JCPDS # 01-089-7129) structure. The diffraction peaks corresponding to hexagonal and cubic  $\text{Ni}_{1-x}\text{Mo}_x$  impurities are shown in \* and #, respectively.

**Table 3.2.** Elemental compositions of Ni<sub>1-x</sub>Mo<sub>x</sub> alloy NPs obtained from EDS and ICP-OES analysis before and after annealing at 450 °C under 5% H<sub>2</sub>/Ar atmosphere.

| Samples                                 | As-Prepared             |      |                |      | Annealed                |      |                |      |
|---|-------------------------|------|----------------|------|-------------------------|------|----------------|------|
|   | EDS <sup>1</sup> (At %) |      | ICP-OES (At %) |      | EDS <sup>1</sup> (At %) |      | ICP-OES (At %) |      |
|   | Ni                      | Mo   | Ni             | Mo   | Ni                      | Mo   | Ni             | Mo   |
| Ni <sub>0.913</sub> Mo <sub>0.087</sub> | 91.31                   | 8.69 | 90.43          | 9.57 | 92.93                   | 7.07 | 90.40          | 9.60 |
| Ni <sub>0.934</sub> Mo <sub>0.066</sub> | 93.45                   | 6.55 | 91.85          | 8.15 | 95.27                   | 4.73 | 91.85          | 8.15 |
| Ni <sub>0.990</sub> Mo <sub>0.010</sub> | 98.98                   | 1.02 | 98.75          | 1.25 | 97.35                   | 2.65 | 98.70          | 1.30 |

<sup>1</sup>Atomic percentages of Ni and Mo were obtained from SEM/EDS analysis of multiple individually prepared samples (five spots per each sample), and averaged values are presented. <sup>2</sup>Atomic percentages of Ni and Mo were obtained from the ICP-OES analysis of multiple individually prepared samples and then averaged to obtained individual values for each sample.

The morphology and size dispersity of alloy NPs were investigated by using TEM. Figure 3.4 shows the representative TEM images recorded from as-synthesized Ni<sub>1-x</sub>Mo<sub>x</sub> NPs with no further size selection. The cubic Ni<sub>1-x</sub>Mo<sub>x</sub> alloys show pseudo-spherical to oblong-shaped particles with average sizes from 18.4 ± 2.9 – 42.8 ± 6.7 nm for x = 0.011 – 0.114 compositions (Figures 3.4A–F, 3.5). Corresponding size histograms show notable variation in size across variable Mo compositions and high resolution TEM images show high crystallinity of the alloy NPs (Figures 3.6–3.7). In general, a noteworthy increase in size with increasing concentration of Mo is observed because of the anisotropic growth of alloy NPs. The cubic Ni<sub>0.934</sub>Mo<sub>0.066</sub>, Ni<sub>0.913</sub>Mo<sub>0.087</sub>, and Ni<sub>0.886</sub>Mo<sub>0.114</sub> NPs show pointy rough surfaces that are potentially attractive for electrocatalysis.

However, the growth of an amorphous surface coating is also noted specifically for  $\text{Ni}_{0.913}\text{Mo}_{0.087}$  and  $\text{Ni}_{0.886}\text{Mo}_{0.114}$  alloy NPs (Figure 3.7). In contrast, the hexagonal NPs show pseudo-spherical to polyhedral particles with average sizes of  $19.3 \pm 4.7$  to  $23.6 \pm 5.3$  nm for  $x = 0.012 - 0.019$  compositions (Figure 3.8). Similarly, phase-pure cubic and hexagonal Ni NPs produced via a similar synthesis show spherical to polygonal particles (Figure 3.9). Both hexagonal  $\text{Ni}_{1-x}\text{Mo}_x$  alloys and phase-pure cubic and hexagonal Ni crystals do not show rough surfaces, which has been commonly observed in cubic  $\text{Ni}_{1-x}\text{Mo}_x$  alloys with high Mo ( $x = 0.066 - 0.114$ ). Thus, we assume that anisotropic alloy NPs with rough surface is induced by high concentration of Mo. It has been reported that primary amines allow for rapid reduction of Ni precursors at elevated temperatures but offer poor surface passivation, resulting in non-uniform growth of both cubic and hexagonal Ni crystals.<sup>55</sup> Thus, further optimization in synthetic parameters and the use of a combination of surfactant ligands and reducing agents (amine, phosphines, and/or alkylaluminum) is necessary for the synthesis of monodisperse alloys. Since the focus of this study is on the investigation of electrocatalytic activity of  $\text{Ni}_{1-x}\text{Mo}_x$  alloys, we minimized the use of strongly coordinating organic surfactants (alkyls and phosphines) to boost the overall HER performance.

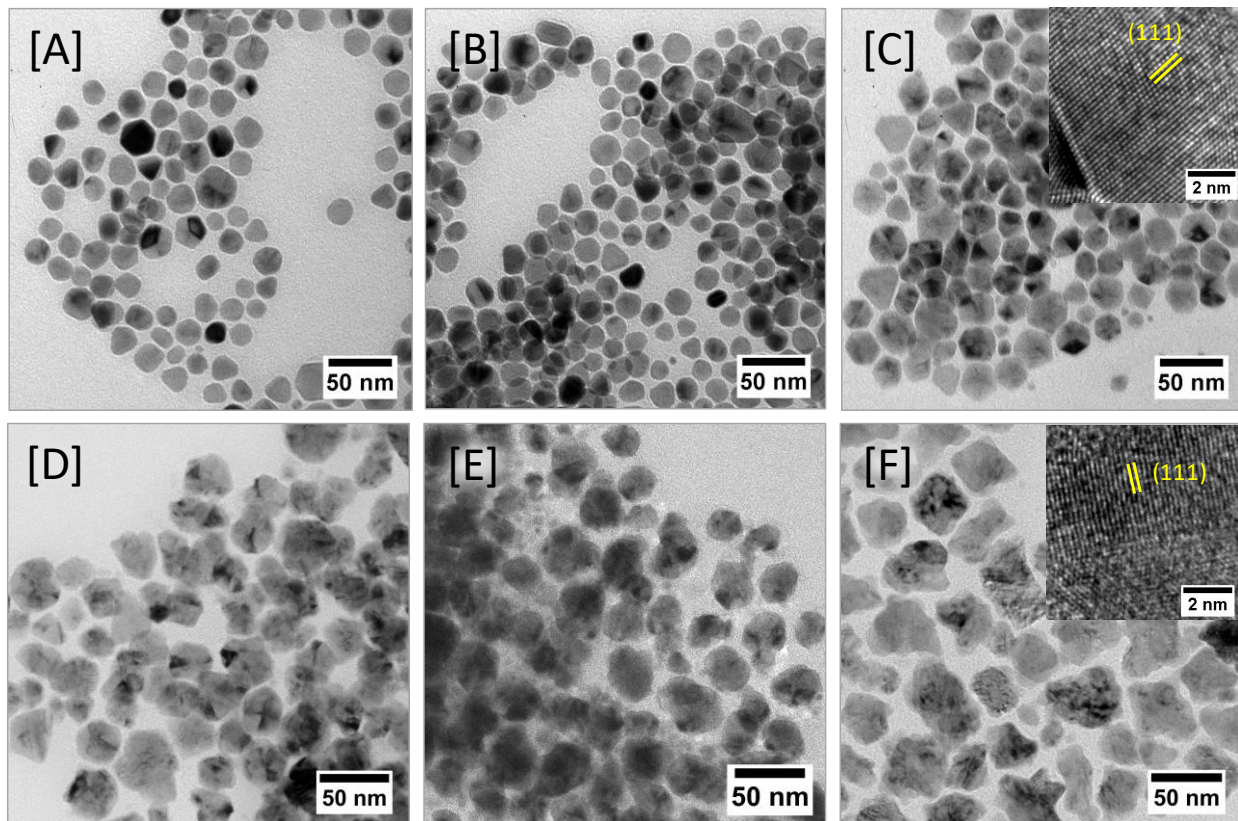


**Figure 3.4** Low resolution TEM images of cubic  $\text{Ni}_{1-x}\text{Mo}_x$  alloy NPs with varying elemental composition: [A]  $x = 0.011$  ( $18.4 \pm 2.9$  nm), [B]  $x = 0.018$  ( $24.9 \pm 5.4$  nm), [C]  $x = 0.036$  ( $22.1 \pm 4.5$  nm), [D]  $x = 0.066$  ( $29.9 \pm 4.8$  nm), [E]  $x = 0.087$  ( $28.9 \pm 5.4$  nm) and [F]  $x = 0.114$  ( $42.9 \pm 6.8$  nm). Insets in (C) and (D) show high resolution images of single particles with lattice fringes of 2.060 and 2.093 Å, corresponding to an expanded (111) plane of cubic Ni.

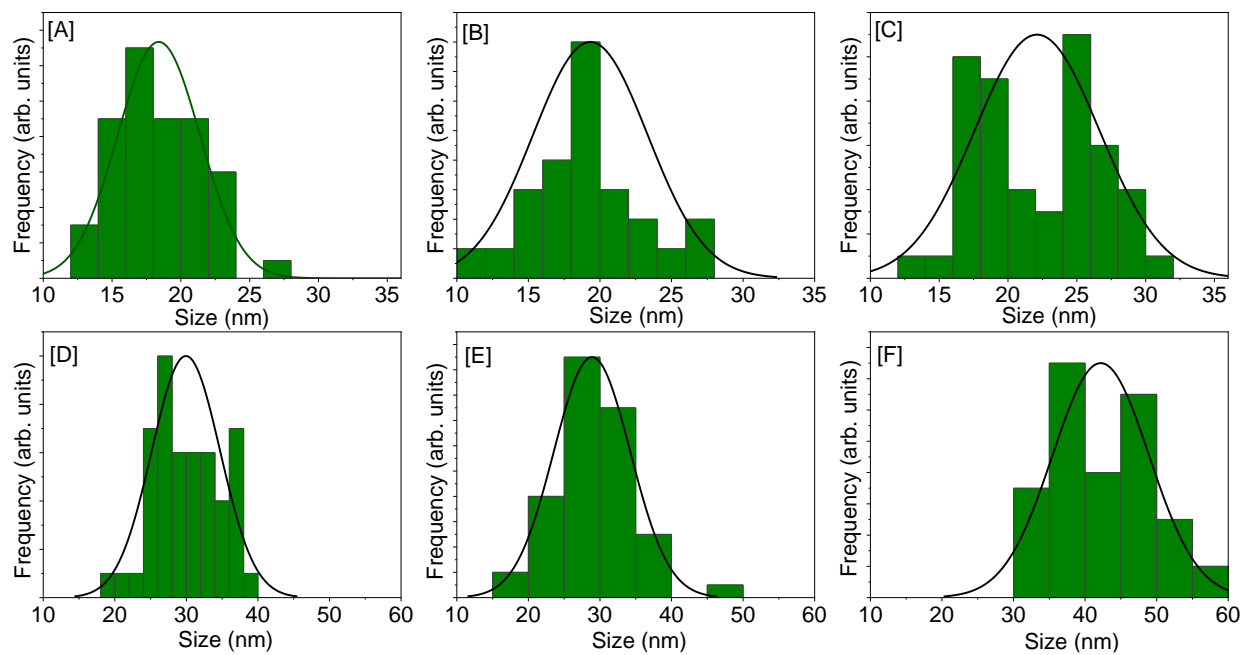


**Figure 3.5** Size histograms of cubic  $\text{Ni}_{1-x}\text{Mo}_x$  alloy NPs with varying elemental composition: [A]  $x = 0.011$ , [B]  $x = 0.018$ , [C]  $x = 0.036$ , [D]  $x = 0.066$ , [E]  $x = 0.087$  and [F]  $x = 0.114$ .

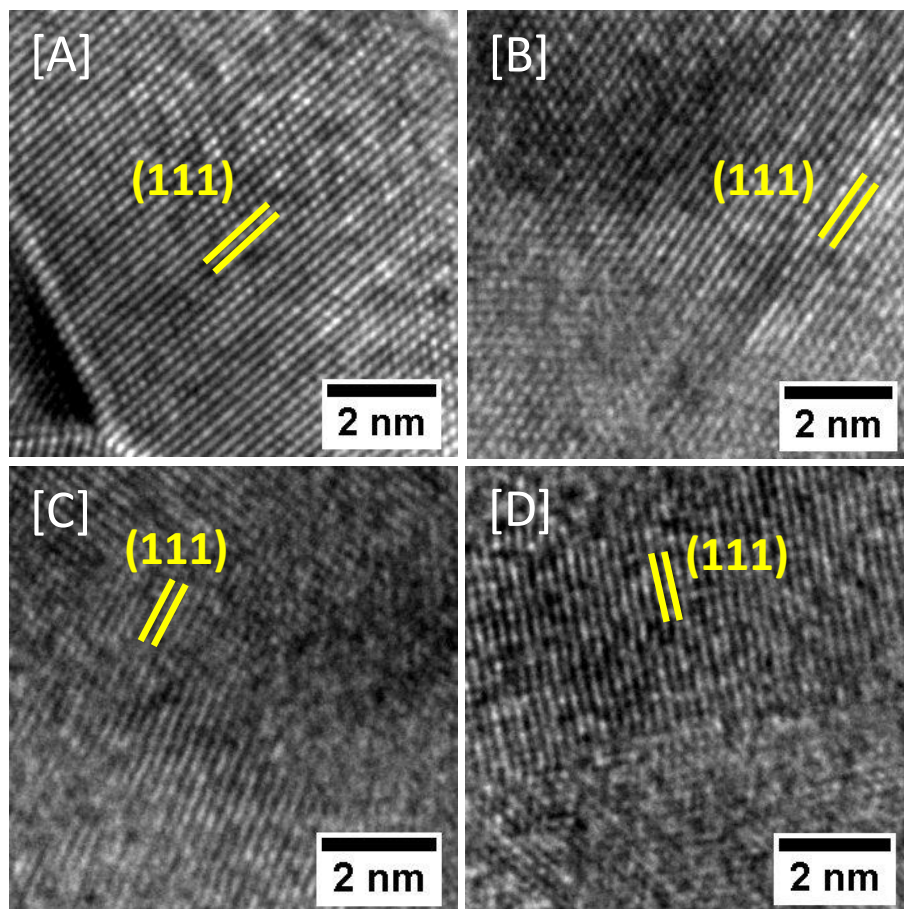


**Figure 3.6** High resolution TEM images of cubic  $\text{Ni}_{1-x}\text{Mo}_x$  alloy NPs with varying elemental composition: [A]  $x = 0.036$ , [B]  $x = 0.066$ , [C]  $x = 0.087$  and [D]  $x = 0.114$  showing lattice fringes of 2.060, 2.070, 2.076, and 2.093 Å, respectively. These values correspond to an expanded (111) plane in face-centered-cubic Ni.



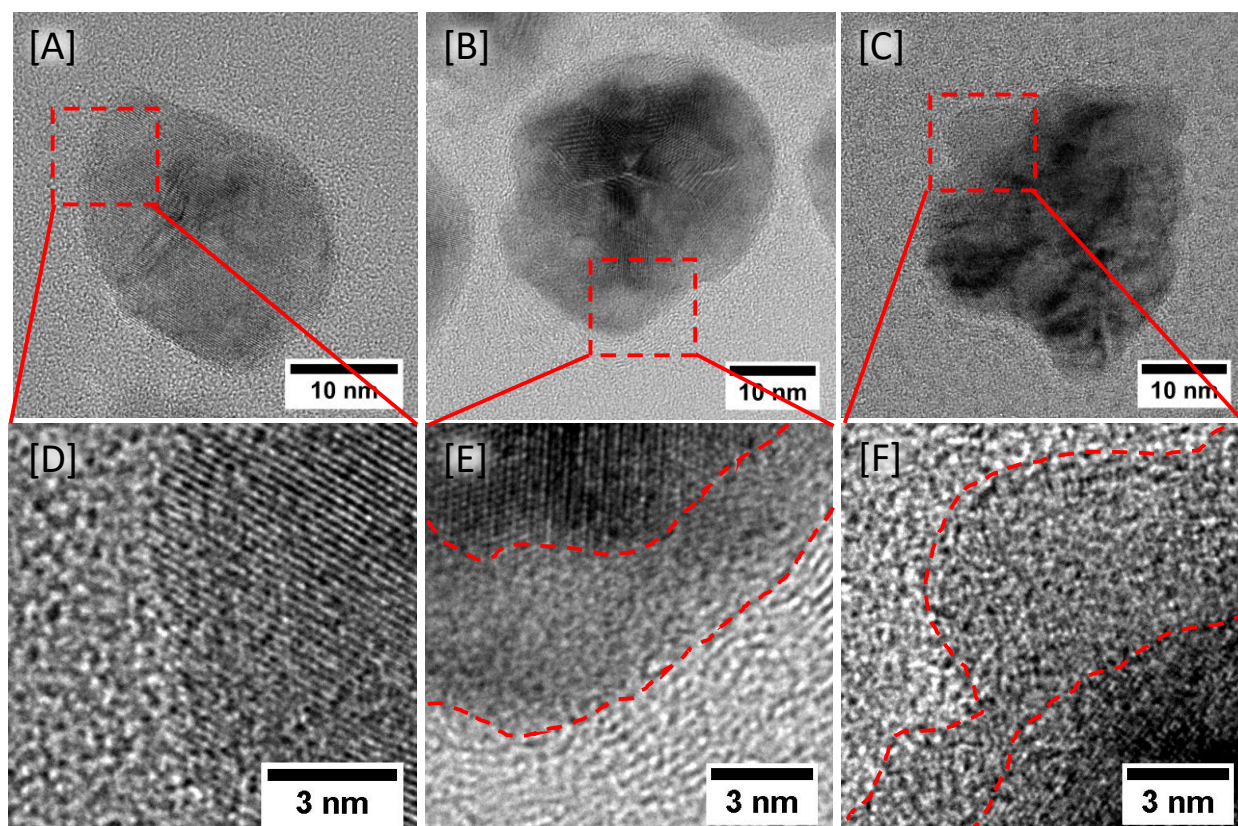


**Figure 3.7** High resolution TEM images of cubic  $\text{Ni}_{1-x}\text{Mo}_x$  alloy NPs with varying elemental composition: [A]  $x = 0.066$ , [B]  $x = 0.087$  and [C]  $x = 0.114$  along with [D-F] their zoomed-in images showing the edge of the particles. With increasing Mo concentration, formation of an amorphous surface coating was noticed.

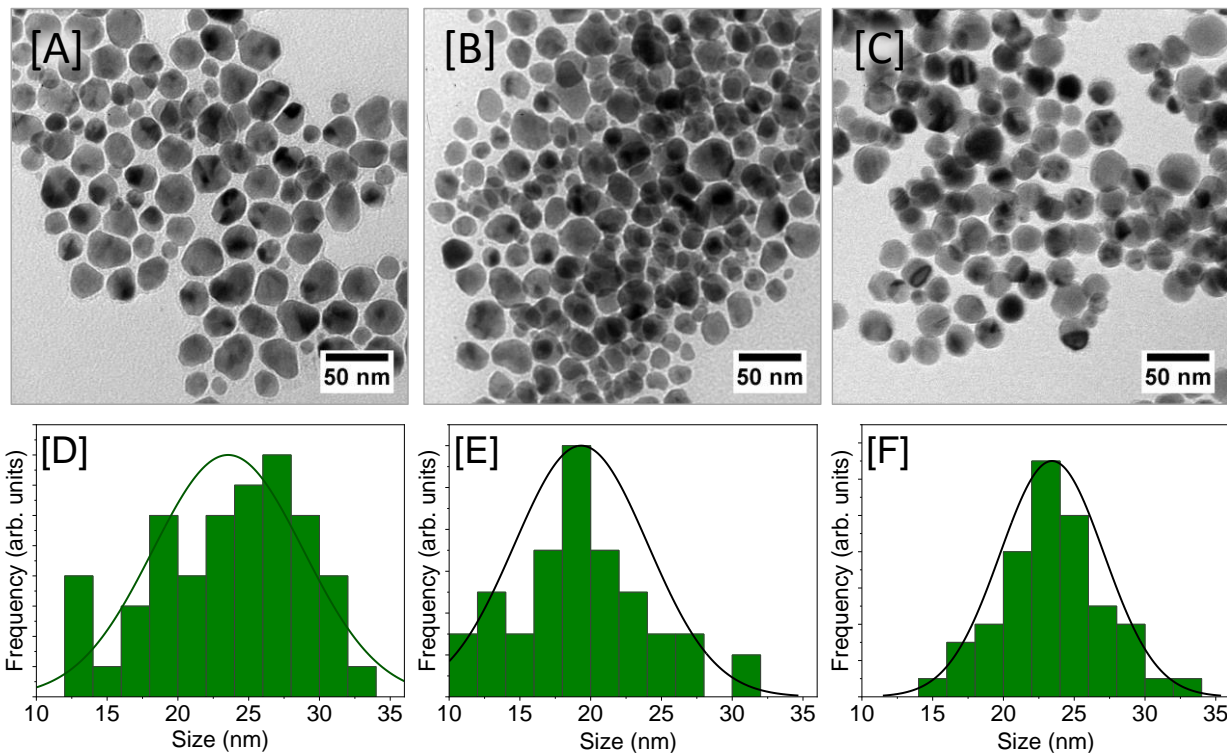


**Figure 3.8** Low resolution TEM images of hexagonal  $\text{Ni}_{1-x}\text{Mo}_x$  alloy NPs with varying elemental composition: [A]  $x = 0.012$  ( $23.6 \pm 5.3$  nm), [B]  $x = 0.015$  ( $19.3 \pm 4.7$  nm) and [C]  $x = 0.019$  ( $23.4 \pm 3.7$  nm) along with corresponding [D-F] size histograms, respectively.

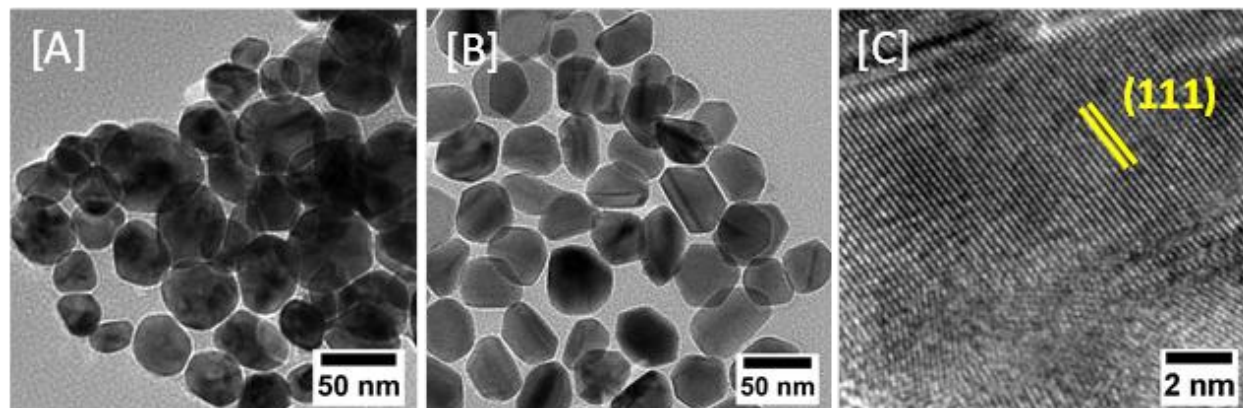


**Figure 3.9** Low resolution TEM images of [A] cubic ( $47.9 \pm 10.1$  nm), [B] hexagonal ( $46.9 \pm 6.7$  nm) Ni nanocrystals. [C] HRTEM image of cubic Ni NPs showing lattice fringes of  $2.030 \text{ \AA}$  assigned for (111) plane.

The surface of cubic  $\text{Ni}_{0.913}\text{Mo}_{0.087}$  and hexagonal  $\text{Ni}_{0.990}\text{Mo}_{0.010}$  alloy NPs (Figure 3.10) was analyzed by XPS. The survey spectra of both samples show peaks corresponding to Ni, Mo, C, and O (Figure 3.11). High-resolution XPS spectra were shifted on the basis of C1s and deconvoluted for the Ni2p and Mo3d orbitals. The binding energies of the deconvoluted Ni2p<sub>3/2</sub> spectra for the annealed cubic  $\text{Ni}_{0.913}\text{Mo}_{0.087}$  NPs were observed at 853.0, 854.1, 855.0, 857.0, 859.1, and 861.2 eV, which correlate to  $\text{Ni}^0$ ,  $\text{Ni}^{2+}$  (NiO),  $\text{Ni}^{2+}$  (Ni(OH)<sub>2</sub>),  $\text{Ni}^{2+}$  (NiO/Ni(OH)<sub>2</sub> multiplex),  $\text{Ni}^0$  ( $\text{Ni}^0 + 6 \text{ eV}$ ) and  $\text{Ni}^{2+}$  satellites, respectively (Figure 3.10A-B).<sup>41,43,45,56-59</sup> The Ni2p<sub>3/2</sub> binding energies of the annealed hexagonal  $\text{Ni}_{0.990}\text{Mo}_{0.010}$  NPs were negligibly shifted compared with the aforementioned states, suggesting presence of similar Ni species. Metallic  $\text{Ni}^0$  was observed as the dominant species for each composition. The deconvoluted peaks in the Mo3d<sub>5/2</sub> region for the cubic  $\text{Ni}_{0.913}\text{Mo}_{0.087}$  alloy NPs were observed at 228.5, 229.0, 230.8, 232.8 eV, which correlate to  $\text{Mo}^0$ ,  $\text{Mo}^{4+}$  (MoO<sub>2</sub>),  $\text{Mo}^{5+}$  (Mo<sub>x</sub>O<sub>y</sub>), and  $\text{Mo}^{6+}$  (MoO<sub>3</sub>) species, respectively

(Figure 3.10C-D).<sup>41,43,45,56-58</sup> Low counts were observed for the high-resolution Mo3d spectra of hexagonal Ni<sub>0.990</sub>Mo<sub>0.010</sub> NPs, which agrees with the low levels of Mo present in the hexagonal NPs. Higher valent charged species were prominent in the Mo3d region over the Ni2p region for annealed samples. As-synthesized Ni<sub>1-x</sub>Mo<sub>x</sub> alloy NPs were also analyzed by XPS (Figure 3.12) and a clear change in surface species was noted after annealing. The pre-annealed Ni<sub>1-x</sub>Mo<sub>x</sub> alloy NPs show Ni<sup>2+</sup> (Ni(OH)<sub>2</sub>) and Mo<sup>6+</sup> (MoO<sub>3</sub>) as dominant species for both crystal phases with low levels of metallic Ni<sup>0</sup> and Mo<sup>0</sup> present. These high valent Ni and Mo species are likely coordinated with residual surfactant ligands or can originate from potential oxide impurities introduced during synthesis and isolation of alloy NPs. Annealing reduces the surface charged states, removes the residual ligands, and increases the metallic Ni<sup>0</sup> and Mo<sup>0</sup> species. Similar spectra were recorded for as-synthesized and annealed alloy NPs with cubic and hexagonal crystal structures, supporting the production of Ni<sub>1-x</sub>Mo<sub>x</sub> alloys.

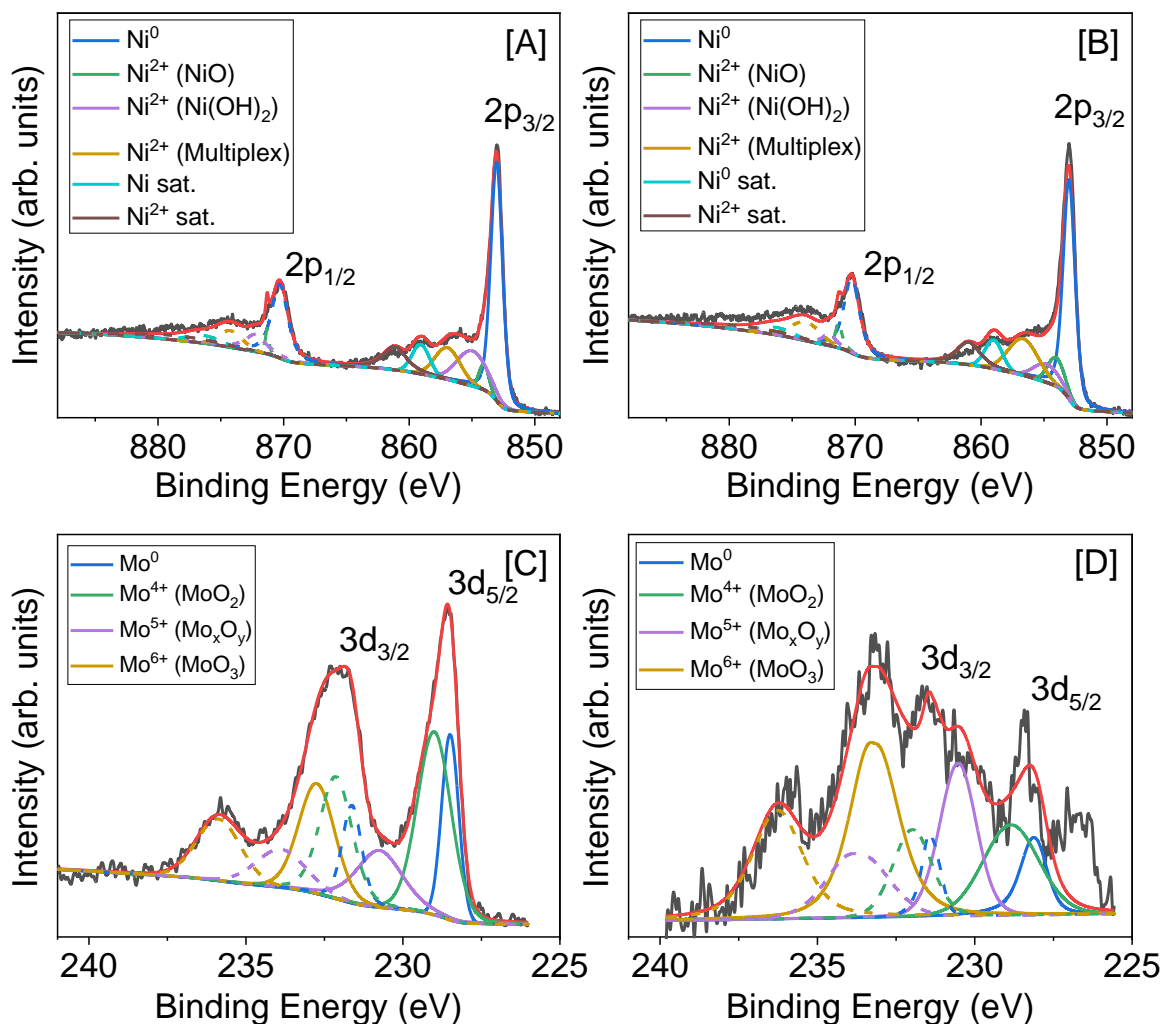


**Figure 3.10** Ni2p and Mo3d XPS spectra of [A,C] cubic Ni<sub>0.913</sub>Mo<sub>0.087</sub> and [B,D] hexagonal Ni<sub>0.990</sub>Mo<sub>0.010</sub> alloy NPs annealed at 450 °C for 2 h under 5% H<sub>2</sub>/Ar atmosphere. In all spectra, solid black lines are experimental data, colored lines are fitted deconvolutions with dash lines representing the doublets, and the solid red lines are spectral envelopes.

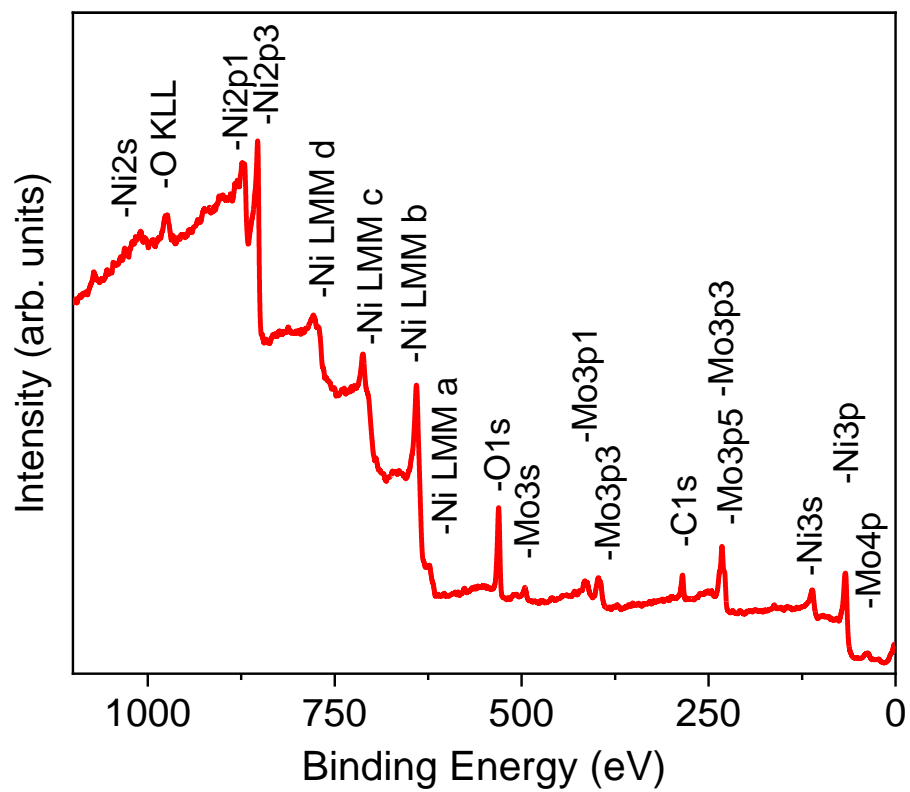


**Figure 3.11** XPS survey spectrum of the annealed Ni<sub>0.913</sub>Mo<sub>0.087</sub> alloy NPs.



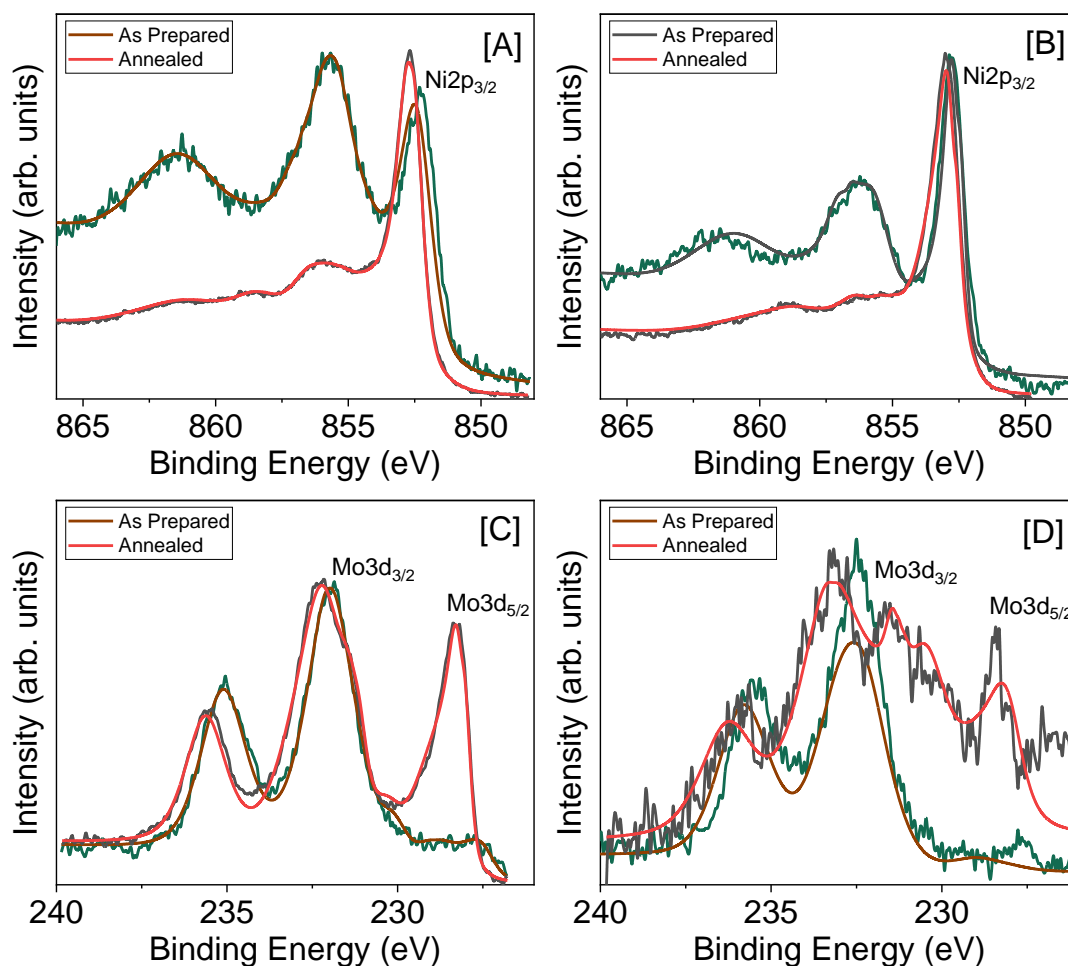


**Figure 3.12** Ni2p and Mo3d XPS spectra of [A,C] cubic  $\text{Ni}_{0.934}\text{Mo}_{0.066}$  and [B, D] hexagonal  $\text{Ni}_{0.990}\text{Mo}_{0.010}$  alloy NPs comparing differences in spectra between the as-synthesized and annealed samples. In all spectra, the green (as-synthesized) and black (annealed) lines represent experimental data and red and brown lines correspond to spectral envelopes.

### 3.3.2 Electrocatalytic activity of $\text{Ni}_{1-x}\text{Mo}_x$ alloy NPs for HER

Titanium foil was utilized to fabricate  $\text{Ni}_{1-x}\text{Mo}_x$  working electrodes for HER. As a current collector, Ti has good mechanical strength and electrical conductivity but lacks HER activity due to electrochemical inertness.<sup>13,32,60</sup> Prior to annealing in  $\text{H}_2/\text{Ar}$  atmosphere, the  $\text{Ni}_{1-x}\text{Mo}_x$  alloy NPs

were not electrocatalytic active. However, after annealing residual ligands were removed (Figure 3.13), charge transport was increased, resulting in HER activity. The TEM images, EDS spectra, and XRD patterns of as-synthesized and post-annealed samples show no significant change in morphology, composition, and crystal structures of the electrocatalysts (Figure 3.14-3.16).

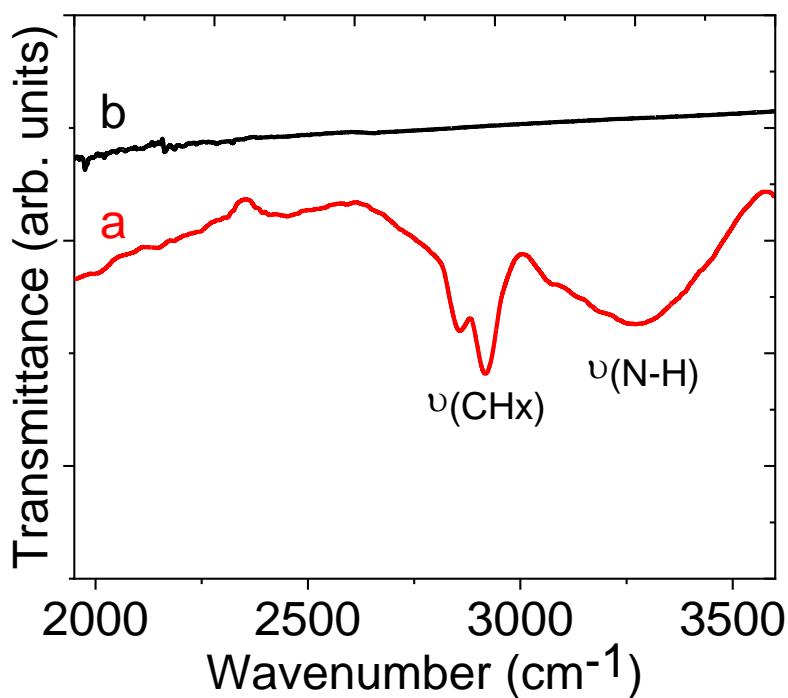


**Figure 3.13** Representative FT-IR spectra of cubic  $\text{Ni}_{0.913}\text{Mo}_{0.087}$  alloy NPs (a) before and (b) after annealing at 450 °C for 2 h under 5%  $\text{H}_2/\text{Ar}$  atmosphere. As-synthesized NPs show characteristic peaks corresponding to alkyl stretching (C-H) at 2850 and 2920  $\text{cm}^{-1}$  that can originate from both oleylamine and octadecene ligands. In addition, a broad stretching vibration corresponding to N-H bonds is observed at  $\sim 3100\text{-}3000\text{ cm}^{-1}$ , suggesting the presence of oleylamine ligands bound to alloy NP surface. Annealed samples show no peaks corresponding to alkyl and alkylamine, consistent with the removal of octadecene and oleylamine from the NP surface.



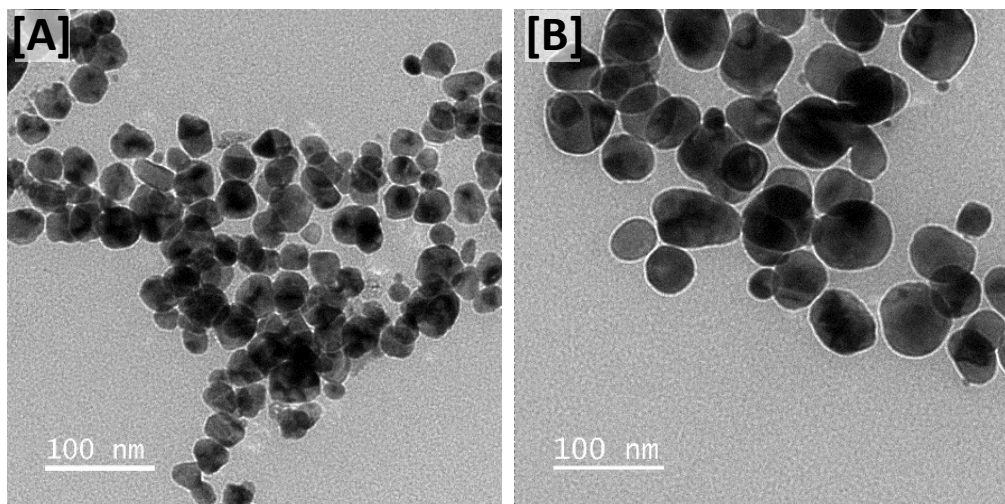


**Figure 3.14** Low resolution TEM images of cubic  $\text{Ni}_{0.934}\text{Mo}_{0.066}$  and hexagonal  $\text{Ni}_{0.990}\text{Mo}_{0.010}$  alloy NPs annealed at 450 °C for 2 h under 5%  $\text{H}_2/\text{Ar}$  atmosphere. These images show no significant change in morphology of prior to and after annealing.

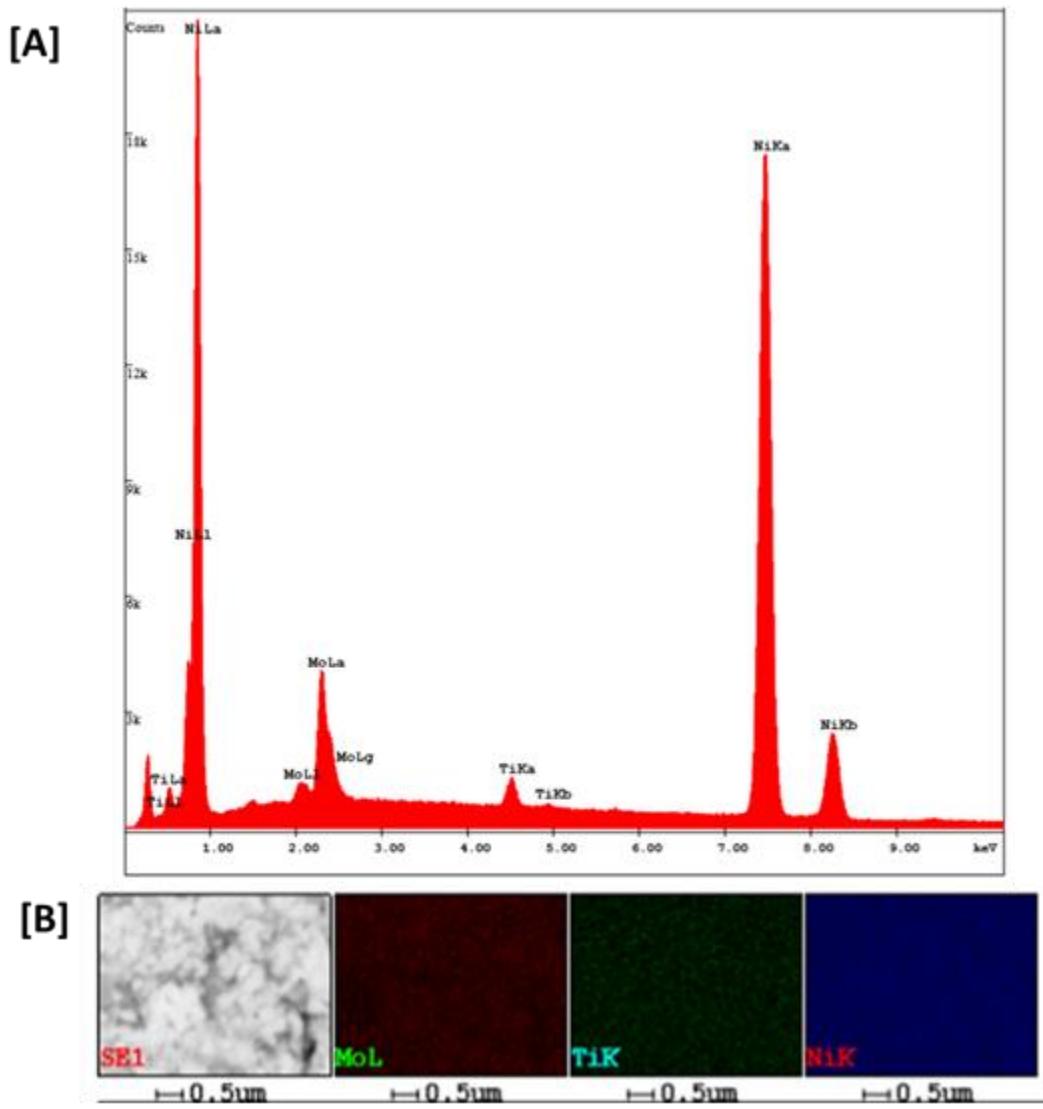


**Figure 3.15** [A] A representative EDAX spectrum of the annealed, cubic  $\text{Ni}_{0.913}\text{Mo}_{0.087}$  alloy NPs. [B] The STEM image and elemental maps of Mo L (red), Ti K (green), and Ni K (blue) recorded from a large area of cubic  $\text{Ni}_{0.913}\text{Mo}_{0.087}$  alloy NPs, showing the elemental distribution.

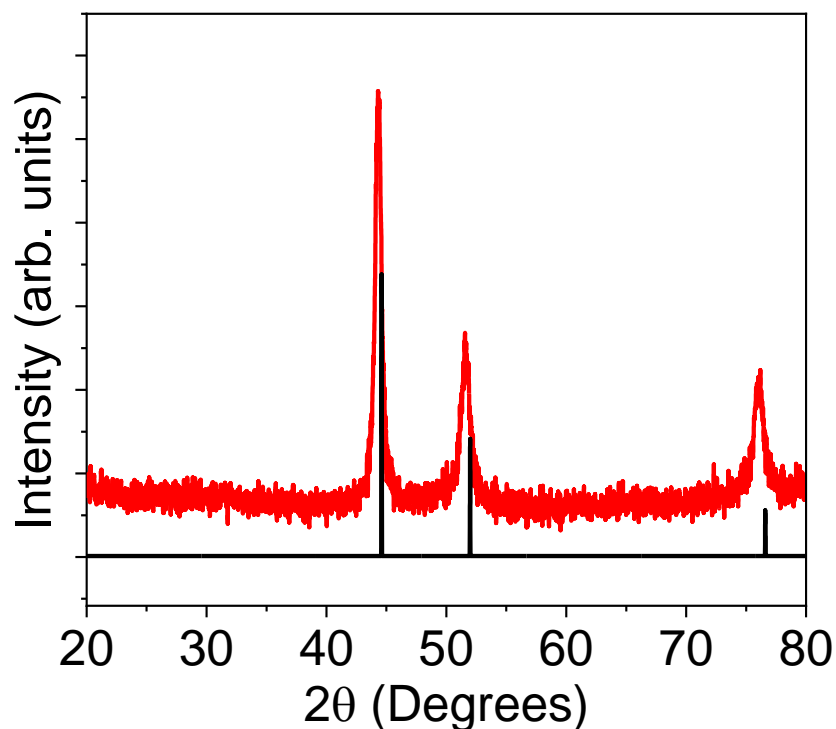


**Figure 3.16** PXRD pattern of cubic Ni<sub>0.913</sub>Mo<sub>0.087</sub> alloy NPs annealed at 450 °C for 2 h under 5% H<sub>2</sub>/Ar atmosphere. The vertical black line corresponds to cubic Ni structure (JCPDS # 01-070-0989).

The HER activity of Ni<sub>1-x</sub>Mo<sub>x</sub> alloy NPs was investigated in alkaline media using linear sweep voltammetry (LSV). Polarization curves of plotted LSV data quantify the behavior of electrocatalysts over a range of current densities. The voltage at specific current densities are extracted from the polarization curves to provide over-potentials by subtracting the thermodynamic value for a specific chemical reaction (0 V vs. RHE for the HER). The standard current densities reported for renewable energy applications are -10 and -20 mA/cm<sup>2</sup>, and provide a metric to compare the performance of various electrocatalysts.<sup>6,29,39,61,62</sup>

HER polarization curves were generated for varying compositions and crystal structures of alloy NPs (Figure 3.17). The HER activity of phase-pure cubic and hexagonal Ni NPs were also investigated as a benchmark for the performance investigation of Ni<sub>1-x</sub>Mo<sub>x</sub> alloy NPs. The cubic and hexagonal Ni NPs exhibit over-potentials of -193 mV and -232 mV at -10 mA/cm<sup>2</sup>, suggesting a higher HER activity for cubic sample. The activity of the cubic Ni NPs was further enhanced after incorporation of Mo for all cubic Ni<sub>1-x</sub>Mo<sub>x</sub> alloy samples. The cubic Ni<sub>0.934</sub>Mo<sub>0.066</sub> alloy NPs showed the lowest over-potential (highest HER activity) of -65 mV at -10 mA/cm<sup>2</sup> (Table 3.3). A similar composition of Ni<sub>0.938</sub>Mo<sub>0.062</sub> showed high HER activity (-62 mV at -10 mA/cm<sup>2</sup>) agreeing with the performance of Ni<sub>0.934</sub>Mo<sub>0.066</sub>. However, further increasing Mo results in a decrease in HER activity. The cubic Ni<sub>0.913</sub>Mo<sub>0.087</sub> and Ni<sub>0.886</sub>Mo<sub>0.114</sub> alloy NPs showed over-potentials of -132 and -253 mV at -10 mA/cm<sup>2</sup>, respectively. This increase in over-potential for the Ni<sub>0.913</sub>Mo<sub>0.087</sub> is likely attributed to significant amorphous coating observed on alloy NPs (Figure 3.7), which can hinder the catalytically active crystalline core (crystal facets) of the particles. In contrast, the hexagonal Ni<sub>0.990</sub>Mo<sub>0.010</sub>, Ni<sub>0.985</sub>Mo<sub>0.015</sub>, and Ni<sub>0.980</sub>Mo<sub>0.020</sub> alloy NPs showed over-potentials of -242, -228, and -162 mV at -10 mA/cm<sup>2</sup>, respectively. Ni<sub>0.980</sub>Mo<sub>0.020</sub> alloy NPs were found to be the most HER active hexagonal sample. In general, the hexagonal alloy NPs show higher over-potentials (lower HER activity) compared to the cubic alloy NPs, consistent with phase dependency observed in monometallic Ni NPs. However, the highest HER active (*i.e.* the lowest over-potential) hexagonal (Ni<sub>0.980</sub>Mo<sub>0.020</sub>, -162 mV) alloy NPs outperformed the lowest HER active cubic (Ni<sub>0.964</sub>Mo<sub>0.036</sub>, -177 mV) NPs.

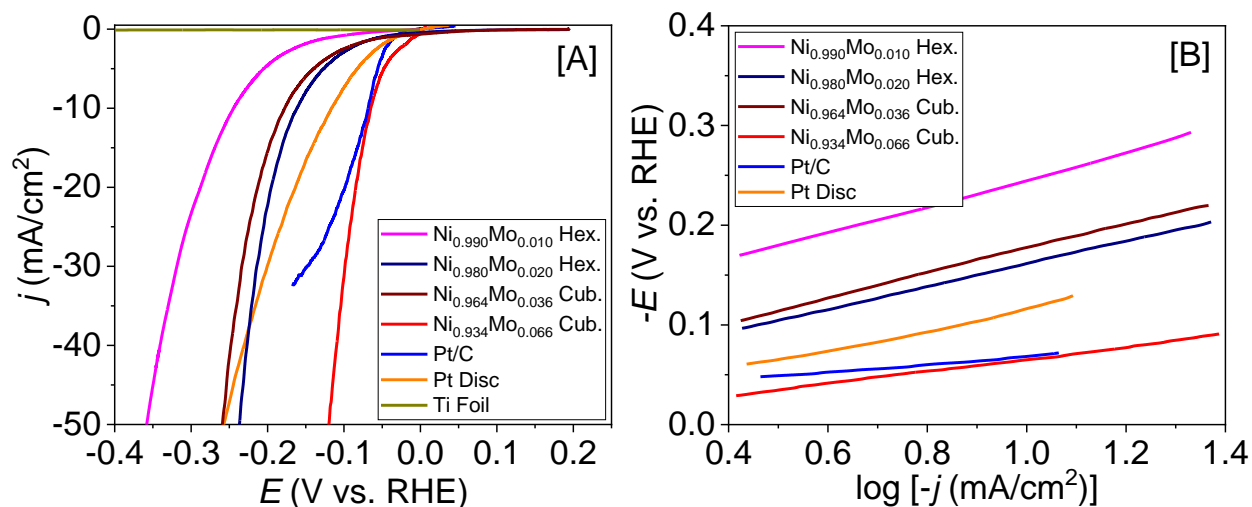


**Figure 3.17** [A] Polarization curves and [B] Tafel plots of Ti foil, commercial Pt disc and Pt/C electrocatalysts, and Ni<sub>1-x</sub>Mo<sub>x</sub> alloy NP electrocatalysts for alkaline HER. Data were recorded at 25 °C under nitrogen atmosphere with continuous stirring.

Polarization behavior for Ni<sub>1-x</sub>Mo<sub>x</sub> electrocatalysts was also compared with a commercial Pt disc and Pt/C electrodes (Figure 3.17). For a baseline, Ti foil electrodes were also tested. A significant improvement in HER activity was observed over the Ti foil substrate for all NPs. The over-potentials of the two Pt-based electrodes agree well with literature reports and performed as expected.<sup>3</sup> For Pt disc, over-potentials of -129 mV and -167 mV were produced at -10 and -20 mA/cm<sup>2</sup>, respectively. The Pt/C electrodes show over-potentials of -68 and -98 mV at -10 and -20 mA/cm<sup>2</sup>, respectively. In contrast, the highest performing hexagonal (Ni<sub>0.980</sub>Mo<sub>0.020</sub>) and cubic (Ni<sub>0.934</sub>Mo<sub>0.066</sub>) alloy NPs show -162/-199 and -65/-85 mV over-potentials at -10/-20 mA/cm<sup>2</sup>, respectively. The hexagonal Ni<sub>1-x</sub>Mo<sub>x</sub> alloy NPs were not observed to rival platinum-based electrodes for HER activity. However, the cubic Ni<sub>1-x</sub>Mo<sub>x</sub> alloys NPs show either comparable or improved HER activity to commercial Pt disc or Pt/C electrocatalysts.

The dependence of HER activity on alloy composition was also investigated (Figure 3.18). In general, an increase in the Mo content results in a decrease in the HER overpotential (increase in HER activity) for both crystal structures. The hexagonal alloys exhibit a sharp increase in HER activity compared to the cubic alloys (Figure 3.18A-B). For cubic alloys, HER activity increases up to 6.6 % Mo followed by a decrease. These interesting trends in experimental data provide a good foundation for future computational studies to understand the variation in the electronic structure with admixing of Mo. Figure 3.18 shows the Pt disc and Pt/C over-potentials as horizontal dashed lines representing a standard electrocatalytic performance achieved for commercial PGMs. Among the  $\text{Ni}_{1-x}\text{Mo}_x$  alloys investigated,  $\text{Ni}_{0.934}\text{Mo}_{0.066}$  alloy NPs outperformed both Pt disc and Pt/C catalysts for alkaline HER, under identical experimental conditions.

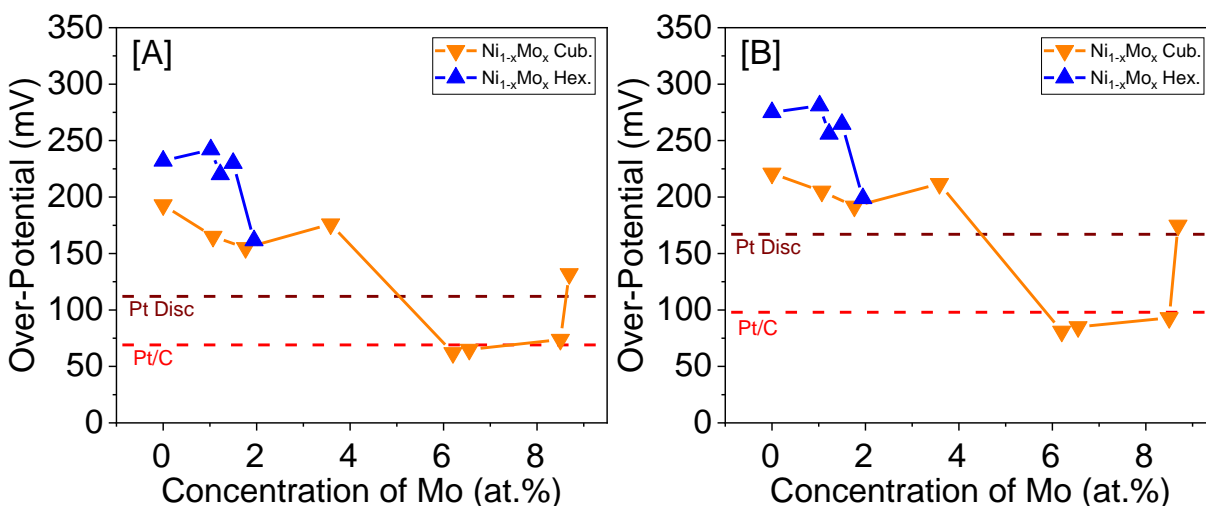


**Figure 3.18** A plot illustrating the effect of Mo content on the magnitude of the over-potential for  $\text{Ni}_{1-x}\text{Mo}_x$  alloy NPs at current densities of [A] -10 and [B] -20  $\text{mA}/\text{cm}^2$ . Two dashed lines represent the standard HER activity obtained for Pt-based electrodes under alkaline conditions.

**Table 3.3** Comparative results of elemental compositions, over-potentials, and Tafel slopes obtained for Ni and Ni<sub>1-x</sub>Mo<sub>x</sub> alloy NPs with cubic and hexagonal crystal phases.

| Sample Name <sup>a</sup>                | Crystal Structure | Elemental Composition by ICP-OES (at.%) |      | Over-Potential (mV at -10mA/cm <sup>2</sup> ) | Over-Potential (mV at -20mA/cm <sup>2</sup> ) | Tafel slope (mV/dec) |
|---|-------------------|---|------|---|---|----------------------|
|   |                   | Ni                                      | Mo   |   |   |                      |
| Ni                                      | Cubic             | 100                                     | 0    | -193  | -221  | 99.0                 |
| Ni <sub>0.913</sub> Mo <sub>0.087</sub> | Cubic             | 90.4                                    | 9.6  | -132  | -175  | 112.3                |
| Ni <sub>0.934</sub> Mo <sub>0.066</sub> | Cubic             | 92.0                                    | 8.0  | -65   | -85   | 61.4                 |
| Ni <sub>0.886</sub> Mo <sub>0.114</sub> | Cubic             | 82.9                                    | 17.1 | -253  | -292  | 131.6                |
| Ni <sub>0.989</sub> Mo <sub>0.011</sub> | Cubic             | 98.8                                    | 1.2  | -165  | -205  | 119.9                |
| Ni <sub>0.964</sub> Mo <sub>0.036</sub> | Cubic             | 96.9                                    | 3.1  | -177  | -212  | 129.4                |
| Ni <sub>0.982</sub> Mo <sub>0.018</sub> | Cubic             | 98.2                                    | 1.8  | -156  | -192  | 120.2                |
| Ni                                      | Hexagonal         | 100                                     | 0    | -232  | -275  | 152.0                |
| Ni <sub>0.990</sub> Mo <sub>0.010</sub> | Hexagonal         | 98.8                                    | 1.2  | -242  | -281  | 127.3                |
| Ni <sub>0.980</sub> Mo <sub>0.020</sub> | Hexagonal         | 97.9                                    | 2.1  | -162  | -199  | 113.9                |
| Ni <sub>0.985</sub> Mo <sub>0.015</sub> | Hexagonal         | 98.3                                    | 1.7  | -228  | -265  | 123.9                |

<sup>a</sup>Elemental compositions of Ni and Mo were investigated by SEM-EDS analysis of multiple individually prepared samples and average values are presented.

To obtain further insights into the electrochemical mechanism on the electrode surface, polarization data were converted into Tafel plots (Figure 3.17B). The Pt/C electrode showed the best (lowest) Tafel slope of 39.6 mV/dec and the best performing cubic  $\text{Ni}_{0.934}\text{Mo}_{0.066}$  alloy NPs showed a comparable slope of 61.4 mV/dec. Of interest, the Pt disc electrode showed an intermediate slope of 104.3 mV/dec. In contrast, the Tafel slopes of cubic  $\text{Ni}_{1-x}\text{Mo}_x$  alloys ( $x=0-11.4\%$ ) were in the range of 61.4–129.4 mV/dec and hexagonal  $\text{Ni}_{1-x}\text{Mo}_x$  alloy NPs ( $x=0-2.0\%$ ) were in the range of 113.9–152 mV/dec. These values suggest that Pt/C electrode exhibits a Heyrovsky HER mechanism whereas the cubic and hexagonal alloy NPs show Volmer-Heyrovsky HER mechanism.<sup>4,42</sup> In general, lower Tafel slopes represent better HER activity and the Pt/C electrode and cubic  $\text{Ni}_{0.934}\text{Mo}_{0.066}$  alloy NPs showed the lowest Tafel slopes of 39.6 and 61.4 mV/dec. Overall, the Tafel slopes obtained for all  $\text{Ni}_{1-x}\text{Mo}_x$  samples show a similar linear behavior and therefore the electrochemical reaction mechanism is expected to be similar.

Stability of the electrocatalyst is important for practical use in HER. In our work, due to the rapid production of hydrogen bubbles, the alloy NPs often exhibit a high delamination behavior. Our experiments could not differentiate between the physical (delamination) and chemical stability (i.e., oxidation, dissociation, deposition, and phase change, etc.) of the electrocatalysts. Nevertheless, a constant current density was applied to the cubic  $\text{Ni}_{0.934}\text{Mo}_{0.066}$  alloy NPs for up to 9 h, and a change in the polarization curve was recorded (Figure 3.19A). The over-potential at  $-10 \text{ mA/cm}^2$  of the cubic  $\text{Ni}_{0.934}\text{Mo}_{0.066}$  alloy NPs increased from  $-71.2$  to  $-84.3$  mV after 9 h. The change in over-potential at  $-20 \text{ mA/cm}^2$  was also recorded and a decrease was observed from 0–1.6 h (Figure 3.19B). This decrease has also been observed in other works and is likely due to an in-situ activation of the Ni-Mo electrocatalysts.<sup>34</sup> A consequential increase in over-potential was observed after 1.6 h, potentially due to physical deterioration of the working electrode. This loss



is less significant than that reported for electrodeposited films of Ni-Mo in acidic media, where ~50 mV increase in over-potential was observed after 20 h.<sup>3,34,41</sup> However, further optimization and/or use of alternate electrode fabrication methods is needed to improve the stability of NP electrodes.

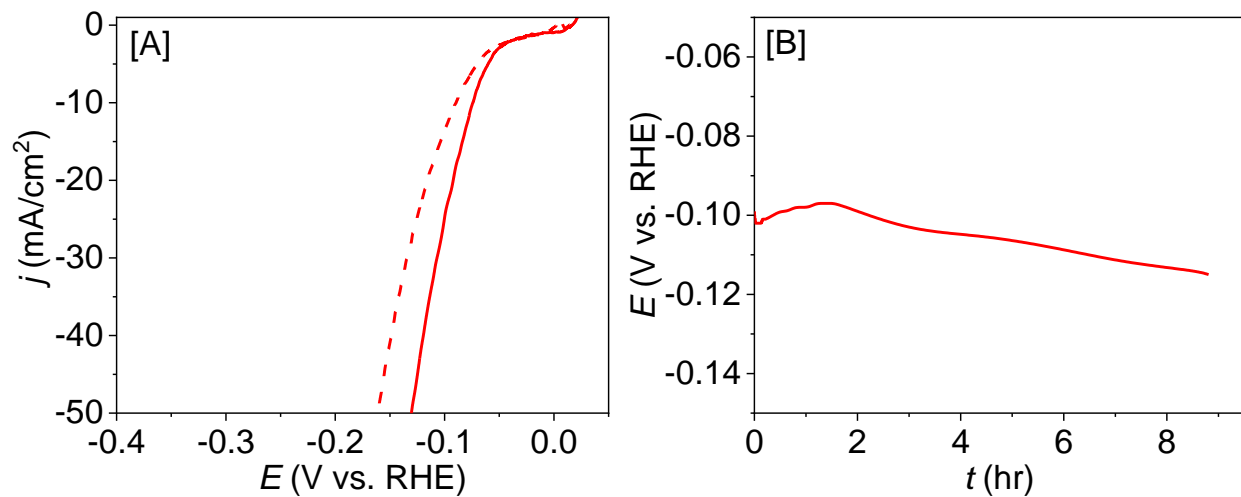


**Figure 3.19** Plots illustrating the stability of Ni<sub>0.934</sub>Mo<sub>0.066</sub> alloy NPs for alkaline HER. [A] Polarization curve for before (solid line) and after (dashed line) 9 h of a constant polarization at a current density of -20 mA/cm<sup>2</sup>. [B] The change in the over-potential over time.

### 3.4 Conclusion

In summary, we have developed a facile colloidal synthesis to produce phase-pure Ni<sub>1-x</sub>Mo<sub>x</sub> alloy NPs displaying cubic and hexagonal crystal structures and varying atomic compositions (0–11.4%), for the first time in the literature. The crystal structures of the alloy NPs were tuned by varying the growth temperature, growth rate, and concentration of the OLA/ODE ligands. As-synthesized alloy NPs exhibit spherical to polygonal morphology with sizes in the range of  $18.4 \pm 2.9 - 42.8 \pm 6.7$  nm across varying Mo compositions (~0–11.4%). A significant increase in shape

anisotropy and growth of pointy rough surfaces were observed at high Mo concentrations (0.066–0.114%), specifically for cubic alloys. The XPS spectra of alloy NPs indicate the presence of Ni<sup>0</sup> and Mo<sup>0</sup> states in the core of NPs and charged Ni<sup>n+</sup> and Mo<sup>n+</sup> states on the surface of NPs, presumably stabilized by surfactant ligands. The HER activity of both Ni and Ni<sub>1-x</sub>Mo<sub>x</sub> alloy NPs in alkaline medium is phase-dependent, with cubic alloys showing a significantly higher performance than the hexagonal alloys. For a current density of -10 mA/cm<sup>2</sup>, cubic alloys showed over-potentials of -62 to -177 mV compared to -162 to -242 mV for hexagonal alloys. For cubic Ni<sub>1-x</sub>Mo<sub>x</sub> alloy NPs, the HER activity increases with increasing Mo up to 6.6%, followed by a decrease in activity at 8.7% and 11.4%. In general, the admixture of Mo into cubic Ni NPs significantly increases the HER activity. Among all the tested materials, the cubic Ni<sub>0.934</sub>Mo<sub>0.066</sub> NPs showed the best alkaline HER activity with over-potentials of -64 and -85 mV at -10 and -20 mA/cm<sup>2</sup>, respectively, which are comparable or superior to commercial Pt-based electrodes.

**Chapter IV. Reduction of Water – Stable and Efficient  
Electrocatalytic Hydrogen Production Cathodes: Phase,  
Morphology, and Composition Dependent NiMoP**

Transition metal phosphides (TMPs) have emerged recently as potential earth-abundant electrocatalyst alternatives to platinum group metals (PGMs) for hydrogen production. Specifically, Ni<sub>2</sub>P has demonstrated high activity (<150 mV @ -10 mA/cm<sup>2</sup>) and stability (no increase in over-potential after 400 cycles) for the hydrogen evolution reaction (HER). However, when compared with platinum (Pt), Ni<sub>2</sub>P exhibits a lower HER activity. Herein, ternary Ni–Mo–P alloy NPs were studied, for the first time, to enhance the HER performance of Ni<sub>2</sub>P. The catalytic performance of discrete Ni<sub>2</sub>P, Ni<sub>12-x</sub>Mo<sub>x</sub>P<sub>5</sub>, and Ni<sub>2-x</sub>Mo<sub>x</sub>P alloy NPs have not been studied, where the influence of crystal phase and composition is poorly understood for the ternary catalysts. Furthermore, solid, hollow and hetero-structured multi-faceted, crystalline morphology NPs were synthesized and studied. The crystallinity is reported to indicate that Mo atoms were incorporated into tetragonal Ni<sub>12</sub>P<sub>5</sub> and hexagonal Ni<sub>2</sub>P lattices. The Ni<sub>1.87</sub>Mo<sub>0.13</sub>P and Ni<sub>10.83</sub>Mo<sub>1.17</sub>P<sub>5</sub> NPs were shown to produce -10 mA/cm<sup>2</sup> at over-potentials of -96 and -82 mV in alkaline media, respectively. This is an improved performance over the synthesized Ni<sub>2</sub>P sample of -126 mV. The high performance electrocatalysts were found to be stable, indicating that NiMoP alloy NPs are one step closer to earth-abundant electrocatalysts competing with PGMs.

## 4.1 INTRODUCTION

Scalable electrolysis and photoelectrochemical water splitting applications require both high performance and earth-abundant platinum-free catalysts. Platinum group metals (PGMs) are often implemented due to their high performance and relatively high stability, however, are limited in scalable applications due to economic costs.<sup>63</sup> Transition metal phosphides (TMPs) have gained attention for maintaining a higher stability over transition metals while retaining moderate performance.<sup>13</sup> Of focus, the scientific community has deemed Ni<sub>2</sub>P as a primary alternative to

PGMs for hydrogen production with a relatively high performance of 130 mV at  $-20 \text{ mA/cm}^2$  in acidic media.<sup>16</sup> However, PGMs still outperform  $\text{Ni}_2\text{P}$  by two-fold with platinum (Pt) exhibiting an over-potential of  $\sim 72 \text{ mV}$  at  $-10 \text{ mA/cm}^2$  in acidic media.<sup>64,65</sup> Therefore, considerations to optimize the performance of  $\text{Ni}_2\text{P}$  are still significant. Ni–Mo alloys have shown high performance ( $80 \text{ mV}$  at  $-20 \text{ mA/cm}^2$ ) to compete with Pt but rapidly degrades under hydrogen production in acidic media.<sup>14</sup> However, a reported increase in stability and performance is observed for Ni–Mo alloy NPs in alkaline conditions,  $70 \text{ mV}$  at  $-20 \text{ mA/cm}^2$ .<sup>14,66</sup> Expanding on a recent study for phase and composition dependence of Ni–Mo alloy NPs, a series of phases, compositions and morphologies were utilized to aid in identifying electrocatalytic characteristics leading to high activity in alkaline media.<sup>66</sup> To date, no NiMoP TMPs have been synthesized or reported for use as an electrocatalyst for the HER. Currently, TMPs are a compromise between performance and high stability, however by incorporating Mo atoms into  $\text{Ni}_x\text{P}_y$  lattices, it is theorized that the HER activity can be improved much like the performance of Ni–Mo compared to Ni. Furthermore, electronegativity and surface binding energies can be optimized for the HER while maintaining metallic conductivity and the enhanced stability from the phosphorous.

Previous studies of nanostructures and performance for  $\text{Ni}_{12}\text{P}_5$  vs  $\text{Ni}_2\text{P}$ .  $\text{Ni}_2\text{P}$  found in literature indicate a lower performance for the  $\text{Ni}_{12}\text{P}_5$  phase based upon a trend of increasing phosphorous leads to higher HER activity.<sup>67,68</sup> Reported TMP systems yield uniform, multifaceted, and pseudospherical morphologies, however, in the case of CoP, the synthesis can be modified to achieve different shapes, compositions, and crystal structures of equivalent NPs.<sup>68–70</sup> This is relevant because the system was modified to produce highly branched particles with a high density of exposed (111) crystal facets which suggest that other parameters besides crystallinity are significant. Furthermore, morphology may not play a significant role and therefore hetero-

structured electrocatalysts, where two different phases are bounded together may lead to increased HER activity.<sup>70</sup>

Herein, ternary NiMoP syntheses were developed to generate TMP electrocatalysts with varying atomic compositions, crystal phase, and morphologies. Each electrocatalysts was studied for the HER. Over-potentials were found to produce  $-10 \text{ mA/cm}^2$  for each sample and discussions into the effect of compositions, crystal phase, and morphologies were formed. Overall, high performance TMP electrocatalysts were synthesized and found to be stable for the HER.

## 4.2 EXPERIMENTAL SECTION

**4.2.1 Materials.** Nickel acetylacetonate ( $\text{Ni}(\text{acac})_2$ ), molybdenum hexacarbonyl ( $\text{Mo}(\text{CO})_6$ ), Octadecene (ODE; 90%) and KOH (reagent grade, 90%) were purchased from Acros Organics. Trioctylphosphine (TOP, 97%) was purchased from Strem. Oleylamine (OLA primary amine, 70%), Dioctyl ether (DOE, 99%), Pt on graphitized carbon (Pt/C, 20 wt.%), and Ti foil (thickness 0.25 mm, 99.7%) were purchased from Sigma-Aldrich. Graphite rods (6.15 mm x 102 mm, 99.9995%) were purchased from Alfa Aesar. Isopropyl alcohol (certified ACS Plus) was purchased from Fisher Scientific. PELCO colloidal Ag paint was purchased from Ted Pella Inc. Henkel Loctite Hysol 9462 epoxy adhesive was purchased from Ellsworth Adhesives. PTFE insulated stranded Ag-plated Cu wire (Chemical-Resistant Wire) was purchased from McMaster-Carr. A Pt (2 mm disc) working electrode and a Hg/HgO reference electrode filled with 1 M NaOH solution were purchased from CH Instruments. OLA, DOE and ODE were dried at  $120 \text{ }^\circ\text{C}$  under vacuum for 3h prior to use. Methanol and toluene were dried over molecular sieves and Na metal, respectively, and distilled under  $\text{N}_2$  prior to use. All other chemicals were used as received.

**4.2.2 Synthesis of Spherical Ni<sub>2-x</sub>Mo<sub>x</sub>P and Ni<sub>12-x</sub>Mo<sub>x</sub>P<sub>5</sub> Alloy NPs.** In a typical synthesis of **Spherical Ni<sub>2-x</sub>Mo<sub>x</sub>P** alloy NPs, Ni(acac)<sub>2</sub> and Mo(CO)<sub>6</sub> precursors of appropriate amounts were added to two separate portions of TOP (5 mL) in two 50 mL flasks and were mixed inside of a nitrogen filled glove box. Both Ni and Mo precursor's setups were attached to a Schlenk line, and degassed at 80 and 120 °C for 20 min before being flushed with argon and heated at 120 and 160 °C for another 20 min to produce homogenous green and yellowish white solutions, respectively. The solutions were then allowed to cool down to room temperature before use. In another 100 mL flask, 10 mL of ODE was placed inside the glove box and also transferred to Schlenk line for degassing at 120 °C for 20 min and then heating at 290 °C under argon. At this point, under vigorous stirring, the Ni/TOP precursor was first injected followed by the Mo/TOP. The temperature was then raised to 350 °C and left for 2h. Ni<sub>12-x</sub>Mo<sub>x</sub>P<sub>5</sub> alloy NPs were produced in a similar manner, except the final heating step of the mixture was maintained at a lower temperature of 300 °C for 1h. Variation of the composition of the alloy NPs was achieved by shifting the initial precursor ratios of Ni to Mo in this method.

**4.2.3 Synthesis of Hetero-Structured Ni<sub>2-x</sub>Mo<sub>x</sub>P and Ni<sub>12-x</sub>Mo<sub>x</sub>P<sub>5</sub> Alloy NPs.** In a typical synthesis of **Hetero-Structured Ni<sub>2-x</sub>Mo<sub>x</sub>P** alloy NPs, cubic Ni<sub>1-y</sub>Mo<sub>y</sub> alloy NPs were first synthesized as reported in Rodene et al.<sup>66</sup> Appropriate amounts of Ni(acac)<sub>2</sub> and Mo(CO)<sub>6</sub> were mixed in OLA (10 mL) and heated at 230 °C for 30 min. After the initial baking, the temperature was then raised to 250 °C for 10 – 60 min. The Ni<sub>1-y</sub>Mo<sub>y</sub> alloy NPs were then washed, dried, and transferred to a 100 mL flask before adding OLA (2 mL) and ODE (10 mL) inside of a glove box. The reaction flask was then connected to a Schlenk line and degassed for 20 min, followed by Ar flushing and heating at 300 °C for 5 min. TOP (8 mL) was then fast injected into the reaction

mixture. The reaction continued at 350 °C for 3h. Similarly, Ni<sub>12-x</sub>Mo<sub>x</sub>P<sub>5</sub> alloy NPs were produced with the final heating step of the mixture adapted to maintain 300 °C for 2h. Variations within the alloy NPs compositions were synthesized by changing the initial composition of the Ni<sub>1-y</sub>Mo<sub>y</sub> alloy NPs.

**4.2.4 Synthesis of Hollow Ni<sub>2-x</sub>Mo<sub>x</sub>P and Ni<sub>12-x</sub>Mo<sub>x</sub>P<sub>5</sub> Alloy NPs.** In a typical synthesis of **Hollow Ni<sub>2-x</sub>Mo<sub>x</sub>P** alloy NPs, Ni(acac)<sub>2</sub> and Mo(CO)<sub>6</sub> were mixed in 2 mL OLA, 5 mL of ODE, and 0.3 mL of TOP in a 100 mL flask, located inside of a glove box. The reaction flask was then connected to a Schlenk line and degassed for 30 min, followed by flushing with argon and heating at 230 °C for 10 min, the temperature was then raised to 330 °C for 2h. Similarly, Ni<sub>12-x</sub>Mo<sub>x</sub>P<sub>5</sub> alloy NPs were produced with the final heating step of the mixture maintained at 290 °C for 1h. Variant alloy NPs compositions were synthesized by varying the initial composition ratios of Ni to Mo.



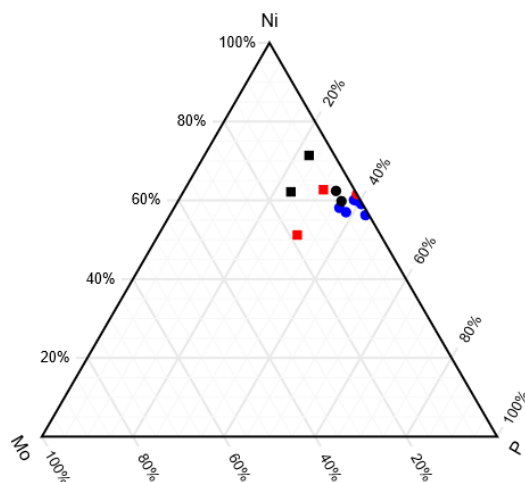


**Figure 4.1** Summarizing the synthesis of the electrocatalysts from SEM-EDAX measurements of the elemental composition distribution between Ni, Mo, and P where: circles and squares indicate the Ni<sub>2</sub>P and Ni<sub>12</sub>P<sub>5</sub> phases, respectively; blue, red, and black denote solids, hollows, and hetero-structured, respectively.

**4.2.5 Isolation and Purification of NPs.** After synthesis, the reaction mixture was promptly cooled using compressed air until the temperature reached ~80 °C. The mixture was transferred into a centrifuge tube and ~5 mL of toluene was added, followed by ~30 mL methanol/acetone mixture. The crude was centrifuged at 4000g for 6 min to collect a black color precipitate of alloy NPs. The alloy NPs were centrifuged another time following re-dispersion and precipitation in toluene and methanol, respectively.

**4.2.6 Physical Characterization.** Powder X-ray diffraction (PXRD) patterns of alloy NPs were recorded using a PANanalytical X’pert PRO equipped with Cu K $\alpha$  ( $\lambda = 1.5418 \text{ \AA}$ ) radiation and calibrated with a Si standard. Transmission electron microscopy (TEM) images were acquired using a JOEL JEM-1400 PLUS TEM microscope equipped with a Gatan OneView digital camera

operating at 120 kV. Samples were prepared by drop casting 10  $\mu\text{L}$  of alloy NPs dispersed in toluene onto carbon-coated Cu grids, followed by solvent evaporation. Elemental composition were recorded using energy dispersive spectra (EDS) attached to a Hitachi Model FE-SEM Su-70 scanning electron microscope (SEM) operating at 20 keV with an in-situ EDAX detector. The powder samples were pressed onto an Al stub using double-sided carbon tape purchased from Ted Pella Inc. The atomic percentages of Ni, Mo and P were obtained by averaging 5 individual measurements for each sample.

**4.2.7 Preparation of Working Electrodes.** The fabrication of electrodes was conducted similarly to previous reports.<sup>66</sup> NiMoP alloy NPs were suspended in IPA (10 mg/mL) via sonication and dropcasted onto cleaned Ti foil (ca. 0.2  $\text{cm}^2$ ). A mass loading of around 1.1 mg was achieved for each sample. The samples were allowed to completely dry, and then were annealed for 2 h at 450  $^\circ\text{C}$  under flowing 5%  $\text{H}_2/\text{Ar}$ . The NP-modified Ti foils were ohmically connected to an insulated copper wire by Ag paint and further insulated by a two-part epoxy. Care was taken to leave the NP film exposed.

**4.2.8 Electrochemical Measurements.** Electrochemical measurements were performed in 2 M KOH using a Gamry Interface 5000P galvanostat. All electrochemical measurements were conducted in a conventional three-electrode cell. An over-dipped graphite rod and Alkaline/HgO (1 M NaOH) electrode were used as the counter and reference electrodes, respectively. Linear sweep voltammetry (LSV) was utilized to obtain polarization curves at a sweep rate of 5  $\text{mV s}^{-1}$  under rapid stirring and bubbling of high purity Ar. Resistance correction was accounted by the current interruption method incorporated with the Gamry Interface 5000P. Electrochemical

stability was investigated by galvanostatically applying a current density of  $-10 \text{ mA/cm}^2$  for 10 h with Ar bubbling and rapid stirring. Electrochemical stability was performed without correcting for uncompensated resistance.

## 4.3 RESULTS AND DISCUSSION

### 4.3.1 Synthesis of $\text{Ni}_{2-x}\text{Mo}_x\text{P}$ and $\text{Ni}_{12-x}\text{Mo}_x\text{P}_5$ alloy NPs

The synthesis of binary  $\text{Ni}_2\text{P}$  and ternary  $\text{Ni}_{2-x}\text{Mo}_x\text{P}$  and  $\text{Ni}_{12-x}\text{Mo}_x\text{P}_5$  was produced by the thermal decomposition of  $\text{Ni}(\text{acac})_2$  and  $\text{Mo}(\text{CO})_6$  in the presence of TOP.<sup>71–73</sup> Initial precursor ratios were chosen to vary elemental composition; while the bake time, temperature, and concentration of TOP was varied to control the crystallinity and phase. Three unique synthesis methods were utilized to vary Mo and P additions into  $\text{Ni}_2\text{P}$  and  $\text{Ni}_{12}\text{P}_5$  crystal lattices. The variations in synthesis methods directly resulted in the formation of different particle morphologies (Figure 4.2). Solid spherical nanoparticles (NPs) were formed from the addition of  $\text{Mo}(\text{CO})_6/\text{TOP}$  Ni–P nucleates during synthesis. The presence of  $\text{Mo}(\text{CO})_6$  was found to aid in nucleation and growth of the NPs. Pseudo-spherical hollow NPs were more or less formed by limiting the concentration of TOP in the starting solution in the presence of all three precursors. The formation of hollow NP morphologies is a result of the Kirkendall effect, a well-known nanoscale.<sup>71,73–75</sup> In contrast, by first synthesizing Ni–Mo alloy NPs and then adding TOP to the synthesis mixture resulted in non-uniform rough polygons (Janus-type hetero-structures), with two distinct compositions or crystal phases fused together.

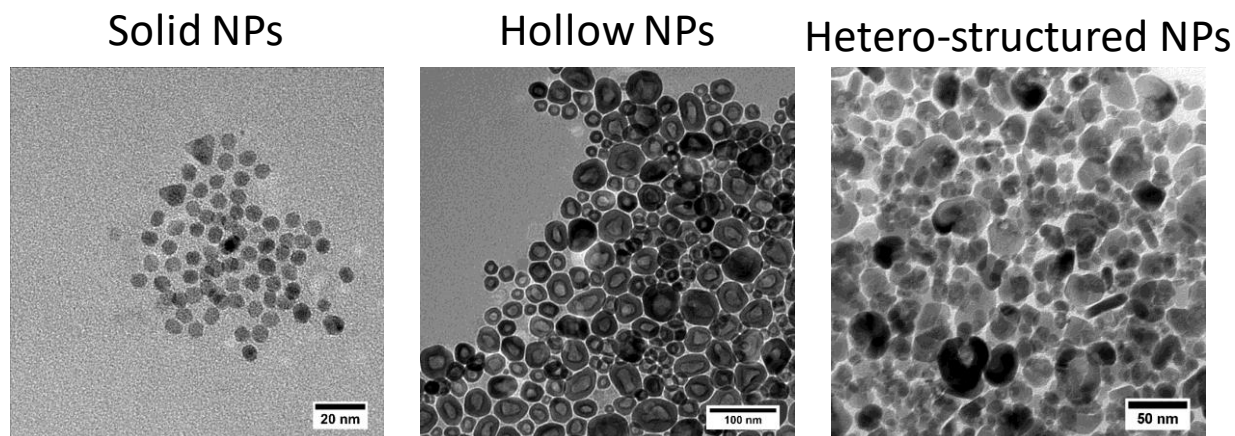


**Figure 4.2** TEM images depicting the differences in morphology produced from the three different synthesis methods for the  $\text{Ni}_{2-x}\text{Mo}_x\text{P}$  NPs.

Powdered XRD patterns are shown for the  $\text{Ni}_{2-x}\text{Mo}_x\text{P}$  and  $\text{Ni}_{12-x}\text{Mo}_x\text{P}_5$  NPs (Figure 4.3). The  $\text{Ni}_2\text{P}$  and  $\text{Ni}_{12}\text{P}_5$  phases were confirmed to be hexagonal and tetragonal, respectively. The patterns for the two phases exhibit multiple peaks in agreement with published pdf patterns. Slight shifting of the peak angles, intensities, and sharpness may be attributed to the incorporation of Mo atoms into the nickel phosphide lattices. A mixture of phases was observed for specific samples and identified by the dominate peaks at either  $\sim 41$  or  $\sim 49$  degrees, corresponding with the  $\text{Ni}_2\text{P}$  and  $\text{Ni}_{12}\text{P}_5$  phases, respectively. Furthermore, these two peaks can be utilized to approximate the ratios between the two TMP phases for a given sample.

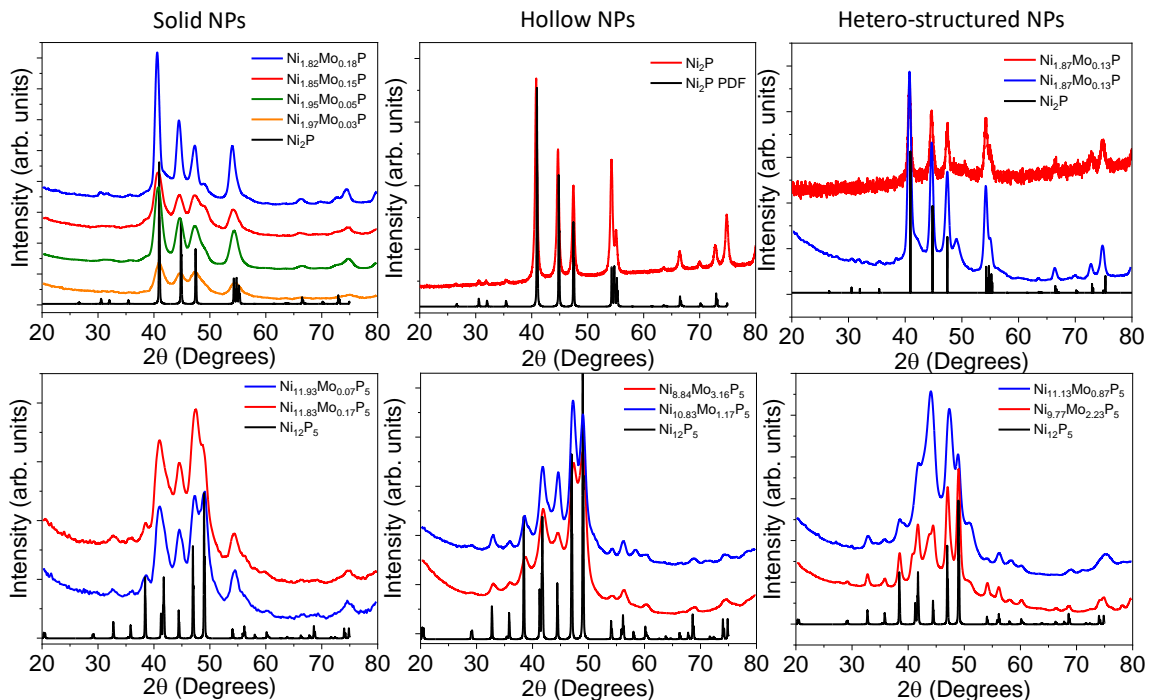


**Figure 4.3** XRD patterns utilized to determine the  $\text{Ni}_2\text{P}$  (top row) and  $\text{Ni}_{12}\text{P}_5$  (bottom row) parent crystal phases. The stacked XRD patterns are the result of samples being synthesized with varying Mo content. The baseline behavior of the top right and top middle patterns is a result of using a different XRD instrument and will be repeated on one instrument.

### 4.3.2 Electrocatalytic activity of Ni–Mo–P alloy NPs for HER

While the electrocatalytic activities of Ni–Mo and  $\text{Ni}_2\text{P}$  have been previously studied for the HER, Ni–Mo–P alloy NPs have not been previously reported. Pseudo-spherical NPs were considered as modified  $\text{Ni}_2\text{P}$  or  $\text{Ni}_{12}\text{P}_5$  crystal structures with varying atomic ratios of Mo (Table 4.1). The synthesized NPs were made into working electrodes by drop casting NPs onto Ti foil substrates and annealing. The annealing step was performed to aid in ligand removal, ohmic conductivity and particle adhesion.

Hollow Ni<sub>2</sub>P NPs were synthesized to give a basis for the HER performance of ternary TMPs. Figure 4.4 shows the polarization curves (current density vs. potential) for Ni<sub>2-x</sub>Mo<sub>x</sub>P and Ni<sub>12-x</sub>Mo<sub>x</sub>P<sub>5</sub> working electrodes plotted against synthesized Ni<sub>2</sub>P and previously report NiMo alloy NPs. The over-potential at -10 mA/cm<sup>2</sup> for the binary hollow Ni<sub>2</sub>P NPs was -126 mV, agreeing with reported literature values for comparable hollow Ni<sub>2</sub>P NPs in acidic media (-130 mV at -20 mA/cm<sup>2</sup>).<sup>16</sup> The polarization curves revealed that both phases contained active electrocatalysts. Therefore, further characterization into activity was performed.

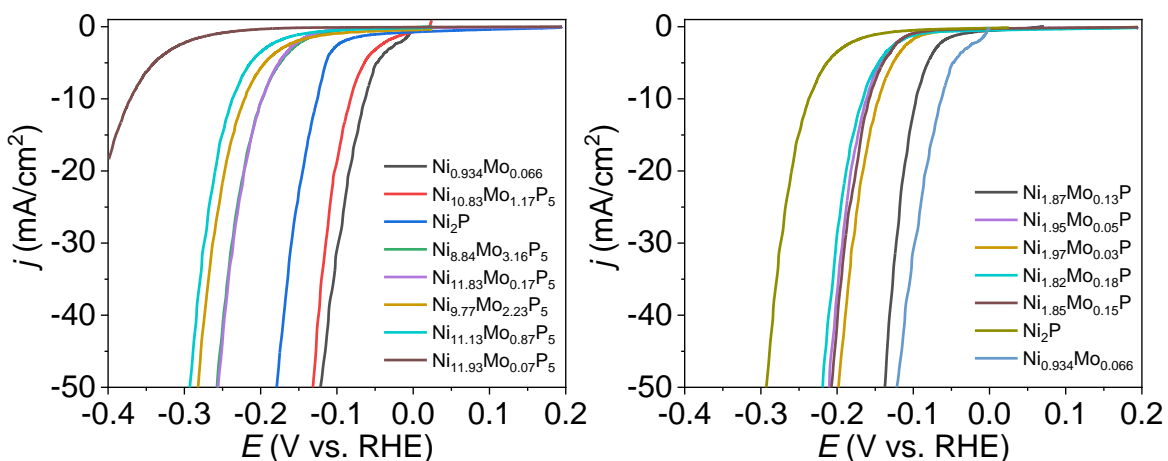


**Figure 4.4** Polarization curves of Ni<sub>1-x</sub>Mo<sub>x</sub> alloy NP from chapter 3, binary Ni<sub>2</sub>P, and ternary Ni<sub>2-x</sub>Mo<sub>x</sub>P and Ni<sub>12-x</sub>Mo<sub>x</sub>P<sub>5</sub> electrocatalysts for alkaline HER. Data were recorded at 25 °C under Ar bubbling with continuous stirring.

To understand the electrocatalytic performance of the synthesized NPs, the electrocatalysts were categorized based upon phase and morphology analyses. An elemental analysis of the synthesized composites was performed, where Ni<sub>2-x</sub>Mo<sub>x</sub>P and Ni<sub>12-x</sub>Mo<sub>x</sub>P<sub>5</sub> alloy NPs were synthesized with Mo content ranging from 0–5.6 % and 0.3–18.3 %, respectively (Figure 4.1). When plotting over-potential vs Mo content, almost no direct correlation to HER performance was

observed (Figure 4.5A). In fact, for the solid  $\text{Ni}_{2-x}\text{Mo}_x\text{P}$  phase, increasing the Mo content resulted in an initial negative effect on performance, with the hollow  $\text{Ni}_2\text{P}$  NPs being the most active. The  $\text{Ni}_{12-x}\text{Mo}_x\text{P}_5$  dominant phase generally showed a performance approaching that of  $-198$  mV at  $-10$   $\text{mA}/\text{cm}^2$ , regardless of the Mo content. The  $\text{Ni}_{12-x}\text{Mo}_x\text{P}_5$  phase with a Mo content of 6.75 % was found to exhibit a low over-potential of  $-82$  mV at  $-10$   $\text{mA}/\text{cm}^2$ . Similarly, two synthesized  $\text{Ni}_{2-x}\text{Mo}_x\text{P}$  phase samples with slightly varying morphologies, where the catalyst with  $\sim 4.2$  % Mo content exhibited low over-potentials of  $-96$  and  $-106$  mV at  $10$   $\text{mA}/\text{cm}^2$ . The performance of the high activity  $\text{Ni}_{2-x}\text{Mo}_x\text{P}$  and  $\text{Ni}_{12-x}\text{Mo}_x\text{P}_5$  NPs compare favorably to other recently reported TMP HER electrocatalysts operating under alkaline conditions.<sup>13,67</sup>

In general, the lower activity  $\text{Ni}_{12-x}\text{Mo}_x\text{P}_5$  samples exhibited higher over-potentials ( $-198$  to  $-370$  mV) than the  $\text{Ni}_{2-x}\text{Mo}_x\text{P}$  phase ( $-145$  to  $-166$  mV) to produce  $-10$   $\text{mA}/\text{cm}^2$ . These electrocatalysts performed worse than the synthesized  $\text{Ni}_2\text{P}$  binary electrocatalyst. This may appear similar to the performance of ternary  $\text{NiFeP}$  TMPs in literature, where the activity was directly between the binary  $\text{Ni}_2\text{P}$  and  $\text{Fe}_2\text{P}$  TMPs.<sup>76,77</sup> Furthermore, any phase dependence may partially be attributed to P content, where  $\text{Ni}_{2-x}\text{Mo}_x\text{P}$  alloy NPs (33.3 % P) were shown to generally be more active than  $\text{Ni}_{12-x}\text{Mo}_x\text{P}_5$  (29.4 % P). Over-potentials vs P content was plotted to demonstrate a correlation between the concentration of non-metal elements and performance (Figure 4.5B). Although the XRD patterns indicated phase-pure patterns matching known pdf patterns of  $\text{Ni}_2\text{P}$  and  $\text{Ni}_{12}\text{P}_5$ , the EDAX analysis indicated phosphorous concentrations deviating from the stoichiometric amounts. In most samples, the P content was higher than expected, indicating that excess P was present for the  $\text{Ni}_2\text{P}$  phase (33.3 % P), whereas excess metallic elements would have indicated the opposite.

The linear correlation for the less active samples demonstrated a direct increase in performance up to 42.9 % P in Figure 4.5B. This agrees with previous reports for other TMPs, where increasing phosphorous content for Co–P and other TMP electrocatalysts directly increases HER activity (i.e., Co < Co<sub>2</sub>P < CoP).<sup>68</sup> Unexpectedly, the performance vs. P content exhibited an addition linear behavior after peaking at 42.9 % P. The more active electrocatalysts in Figure 4.5B contradict the increasing P content trend to give low over-potentials. One interpretation of the data suggests that the phosphorous content is stabilized at a specific phase and that excess metallic elements are present to increase performance.

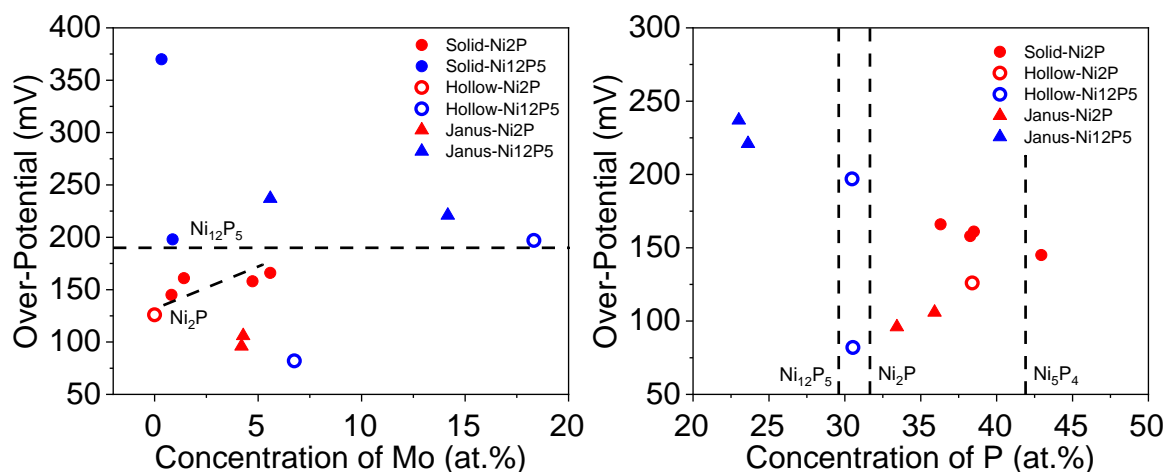


**Figure 4.5** Over-potential at  $-10 \text{ mA/cm}^2$  plotted against percent composition for Mo and P, respectively.

On the other hand, the high activity samples could be attributed to unique morphologies, as some of the morphologies were difficult to categorize. In general, the solid particles that did not exhibit a strong Kinderall effect and were less active than the binary Ni<sub>2</sub>P sample in both phases. Janus-type structures were observed in the Ni<sub>1.87</sub>Mo<sub>0.13</sub>P, Ni<sub>9.77</sub>Mo<sub>2.23</sub>P<sub>5</sub> and Ni<sub>11.13</sub>Mo<sub>0.87</sub>P<sub>5</sub> alloy NPs and potentially are contributing to higher performance. No previous literature has been



reported on the influence of performance based on morphological differences between hollow and solid pseudo-spherical electrocatalyst NPs. However, hollow NP electrocatalysts were reported to have a performance consistent with similar morphological shapes in literature.<sup>16,68,74</sup> Here, the data is suggesting that hollow and hetero-structured electrocatalysts may exhibit superior HER performance to solid NPs. Furthermore, complex XRD patterns for the ternary TMP NPs made differentiating peak position and intensities difficult and suggests that an increase in activity may be attributed to minute amounts of Ni or Ni –Mo alloy present around 43 (dominant cubic NiMo peak) and 49 degrees. HR-TEM and/or STEM/EDS will help correlate composition, phase, and morphology to HER activity.

**Table 4.1** Comparative results of over-potentials, elemental compositions, general morphology and crystal phase obtained for Ni<sub>2</sub>P, Ni<sub>2-x</sub>Mo<sub>x</sub>P and Ni<sub>12-x</sub>Mo<sub>x</sub>P<sub>5</sub> NPs.

| Name  | Over-Potential<br>mV @ -10mA/cm <sup>2</sup> | Ni   | Mo   | P    | Notes                                    |
|---|--|------|------|------|--|
| Ni <sub>1.82</sub> Mo <sub>0.18</sub> P               | -166   | 58.1 | 5.6  | 36.3 | Solid-Ni <sub>2</sub> P                  |
| Ni <sub>1.85</sub> Mo <sub>0.15</sub> P               | -158   | 57.0 | 4.7  | 38.3 | Solid-Ni <sub>2</sub> P                  |
| Ni <sub>1.95</sub> Mo <sub>0.05</sub> P               | -161   | 60.1 | 1.4  | 38.5 | Solid-Ni <sub>2</sub> P                  |
| Ni <sub>1.97</sub> Mo <sub>0.03</sub> P               | -145   | 56.2 | 0.8  | 42.9 | Solid-Ni <sub>2</sub> P                  |
| Ni <sub>11.83</sub> Mo <sub>0.17</sub> P <sub>5</sub> | -198   | 59.9 | 0.9  | 39.2 | Solid-Ni <sub>12</sub> P <sub>5</sub>    |
| Ni <sub>11.93</sub> Mo <sub>0.07</sub> P <sub>5</sub> | -370   | 59.0 | 0.3  | 40.6 | Solid-Ni <sub>12</sub> P <sub>5</sub>    |
| Ni <sub>2</sub> P                                     | -126   | 61.6 | 0.0  | 38.4 | Hollow-Ni <sub>2</sub> P                 |
| Ni <sub>8.84</sub> Mo <sub>3.16</sub> P <sub>5</sub>  | -197   | 51.2 | 18.3 | 30.5 | Hollow/S-Ni <sub>12</sub> P <sub>5</sub> |
| Ni <sub>10.83</sub> Mo <sub>1.17</sub> P <sub>5</sub> | -82  | 62.7 | 6.8  | 30.5 | Hollow-Ni <sub>12</sub> P <sub>5</sub>   |
| Ni <sub>1.87</sub> Mo <sub>0.13</sub> P               | -96  | 62.4 | 4.2  | 33.4 | Janus-Ni <sub>2</sub> P                  |
| Ni <sub>1.87</sub> Mo <sub>0.13</sub> P               | -106   | 59.8 | 4.3  | 35.9 | Janus-Ni <sub>2</sub> P                  |
| Ni <sub>9.77</sub> Mo <sub>2.23</sub> P <sub>5</sub>  | -221   | 62.1 | 14.2 | 23.6 | Janus-Ni <sub>12</sub> P <sub>5</sub>    |
| Ni <sub>11.13</sub> Mo <sub>0.87</sub> P <sub>5</sub> | -237   | 71.4 | 5.6  | 23.0 | Janus-Ni <sub>12</sub> P <sub>5</sub>    |

\* The composition in the sample name is determined by SEM-EDAX.

The stability of HER electrocatalysts is important for any practical applications. The high performance electrocatalyst alloys have demonstrated excellent short-term HER stability. To obtain stability data, the working electrode preparation is very important, as some electrocatalysts synthesized via the colloidal methods resulted in poor particle-substrate adhesion, such as the sample that gave an over-potential of -370 mV at -10 mA/cm<sup>2</sup>. Nevertheless, most working electrodes formed with the method provided gave excellent NP adhesion. A constant current

density was applied to multiple electrocatalysts for up to 10 h at both  $-10$  and  $-20$  mA/cm<sup>2</sup> without ohmic correction. A change in the polarization curve is shown in Figure 4.6A, where no significance loss in performance was observed after 10 h compared to Ni–Mo in chapter 3. Figure 4.6B shows deviations in the recorded voltage over time, which most likely were attributed to residual bubble formation. Furthermore, it was observed that when left in air for a period of time after anneal or after electrochemical testing, the TMP working electrodes slightly deactivate. However, the activity was shown to be reactivated after a few cathodic sweeps. Due to stability and performance, TMPs are foreseen to be implemented in applications such as photoelectrochemical devices.<sup>21,78</sup>

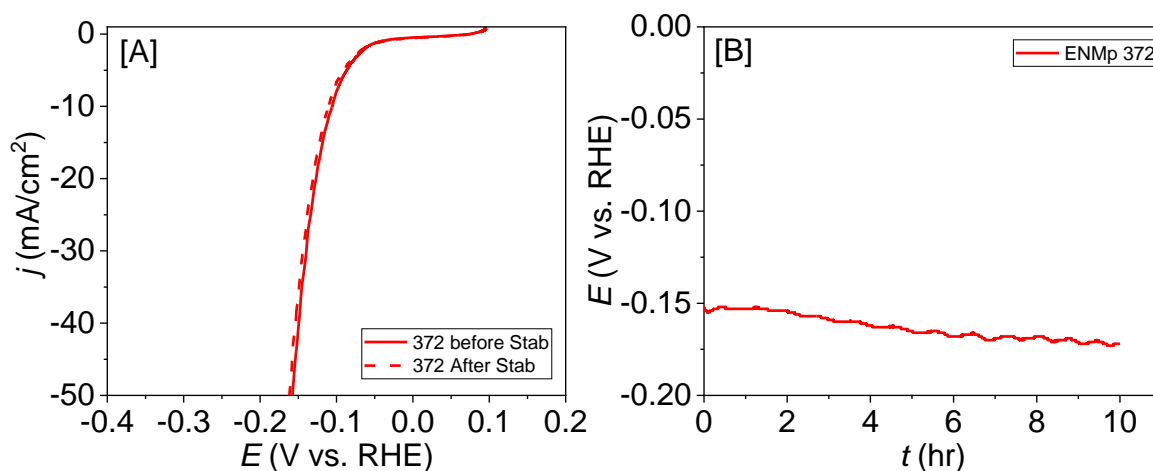


**Figure 4.6** Plots illustrating the stability of Ni<sub>1.87</sub>Mo<sub>0.13</sub>P NPs for alkaline HER. [A] The polarization curve before (solid line) and after (dashed line) 10 h of a constant applied current at  $-10$  mA/cm<sup>2</sup>. [B] Change in over-potential per 10 h of  $-10$  mA/cm<sup>2</sup>, applied without ohmic correction.

## 4.4 CONCLUSIONS

For the first time, three unique methods were developed to synthesize binary Ni<sub>2</sub>P and ternary Ni<sub>2-x</sub>Mo<sub>x</sub>P and Ni<sub>12-x</sub>Mo<sub>x</sub>P<sub>5</sub> NPs with varying elemental composition, crystal phase, and morphologies; to increase the HER activity of stable, earth-abundant electrocatalysts. Hollow Ni<sub>2</sub>P NPs were successfully synthesized and found to perform better than similar samples reported in literature. Increasing phosphorous content for the less active electrocatalysts directly resulted in an increase in HER activity (up to 42.9 % P) and the Ni<sub>2</sub>P phase was overall more active. Deviations in P content from stoichiometric quantities specific to each phase suggest the possible presence of secondary phases and compositions given by slight variation/additional peaks. These secondary phases and composition may be present in the XRD patterns and be attributed to the higher TMP activity for specific catalysts. Furthermore, hetero-structured electrocatalysts emphasize this theory. In summary, HER performance was increased to 84 mV at -10 mA/cm<sup>2</sup> for the ternary TMPs, owing to the formation of unique electrocatalysts resulting from the addition of Mo.

## **Chapter V. Conclusions and Future Directions**

## 5.1 DISSERTATION CONCLUSION

Efficient electrocatalysts are desirable for any electrochemical application. Of urgency, is the necessity to produce hydrogen readily and affordably. Herein, electrocatalysts for hydrogen production through the electrolysis of water were investigated. For the first time in the literature, facile colloidal syntheses were developed to produce distinct phase-pure  $\text{Ni}_{1-x}\text{Mo}_x$ ,  $\text{Ni}_2\text{P}$ ,  $\text{Ni}_{2-x}\text{Mo}_x\text{P}$  and  $\text{Ni}_{12-x}\text{Mo}_x\text{P}_5$  alloy nanoparticles (NPs) as low-cost and earth-abundant electrocatalysts for alkaline HER. Ni–Mo and Ni–Mo–P alloys NPs are presented as stable and efficient alternatives to replace expensive PGM electrocatalysts in alkaline media. Electrochemical techniques were developed and reported to aid in understanding electrochemical performance, chemical mechanisms and the stability of electrocatalysts at the electrode-electrolyte interfaces.

Phase-pure  $\text{Ni}_{1-x}\text{Mo}_x$  alloy NPs displayed cubic and hexagonal crystal structures with varying atomic compositions (0–11.4%) and spherical to polygonal morphologies. An XPS analysis was performed to investigate the dominant  $\text{Ni}^{n+}$  and  $\text{Mo}^{n+}$  surface species of the alloy NPs and may correlate lower charged species to higher performance. The HER activity of both Ni and  $\text{Ni}_{1-x}\text{Mo}_x$  alloy NPs in alkaline medium was found to be phase-dependent towards the cubic phase. For a current density of  $-10 \text{ mA/cm}^2$ , cubic alloys showed lower over-potentials than the hexagonal phase of  $-62$  to  $-177 \text{ mV}$  and  $-162$  to  $-242 \text{ mV}$ , respectively. For cubic  $\text{Ni}_{1-x}\text{Mo}_x$  alloy NPs, the HER activity increases with increasing Mo up to 6.6%, followed by a decrease in activity at 8.7% and 11.4%. In general, the admixture of Mo into cubic Ni NPs was shown to significantly increase the HER activity. Among all the tested materials, the cubic  $\text{Ni}_{0.934}\text{Mo}_{0.066}$  NPs showed the best alkaline HER activity with over-potentials of  $-64$  and  $-85 \text{ mV}$  at  $-10$  and  $-20 \text{ mA/cm}^2$ , respectively. These alloys are comparable to or superior than commercial Pt-based electrodes resulting in a patent application being submitted.

Now emphasis is on elucidating stable high performance electrocatalysts, which will resemble materials that have a likelihood of real-world implementation; ternary transition metal phosphides (TMPs) were studied for alkaline HER. Three distinct syntheses were utilized to produce binary  $\text{Ni}_2\text{P}$  and ternary  $\text{Ni}_{2-x}\text{Mo}_x\text{P}$  and  $\text{Ni}_{12-x}\text{Mo}_x\text{P}_5$  alloy NPs with varying elemental composition, crystal phase, and morphologies. The catalytic performance of discrete  $\text{Ni}_{2-x}\text{Mo}_x\text{P}$  and  $\text{Ni}_{12-x}\text{Mo}_x\text{P}_5$  alloy NPs have not been previously studied for the HER. Furthermore, this work aimed to understand the influence of crystal phase and composition of ternary TMP electrocatalysts for the HER. Specific phases, compositions and morphologies were studied to understand correlations to intrinsic properties of TMPs leading to high HER activity.

Hollow  $\text{Ni}_2\text{P}$  NPs were successfully synthesized and studied; lower performance was found and expected compared to Ni–Mo and PGMs. In general, increasing phosphorous (P) content from  $\text{Ni}_{12}\text{P}_5$  (70 at. %) to  $\text{Ni}_2\text{P}$  (66 at. %) phases gave higher HER activity for the ternary electrocatalysts as well. The P content collected from EDS did not directly correlate with the stoichiometric P quantities, suggesting that slight variation/additional peaks in the XRD patterns may be present as minority mixed phases. These possible mixed phases may have resulted in the higher TMP HER activity for the  $\text{Ni}_{1.87}\text{Mo}_{0.13}\text{P}$  and  $\text{Ni}_{10.83}\text{Mo}_{1.17}\text{P}_5$  alloy NPs, whereas the increasing phosphorous trend did not fit. Furthermore, the hetero-structures may have a role on performance where unique morphologies may have led to have higher HER performance without a direct relation to Mo concentration. The  $\text{Ni}_{1.87}\text{Mo}_{0.13}\text{P}$  and  $\text{Ni}_{10.83}\text{Mo}_{1.17}\text{P}_5$  NPs were shown to be stable for 10 h at  $-10 \text{ mA cm}^{-2}$  with over-potentials of  $-96$  and  $-82 \text{ mV}$  in alkaline media, respectively. The  $\text{Ni}_{1.87}\text{Mo}_{0.13}\text{P}$  and  $\text{Ni}_{10.83}\text{Mo}_{1.17}\text{P}_5$  alloy NPs exhibited an improved performance over the synthesized  $\text{Ni}_2\text{P}$  sample ( $-126 \text{ mV}$  at  $-10 \text{ mA cm}^{-2}$ ). A strong correlation between phase dependence and the influence of Mo on HER activity needs to be further investigated.

Furthermore, understanding the intrinsic properties of electrocatalysts leading to high water splitting performance and stability can apply electrocatalysts in other research applications, such as water remediation of pollutants and sustainable chemical manufacturing practices. Photoelectrochemical (PEC) water remediation was reported in appendix A1, where the photocatalytic efficiency of g-C<sub>3</sub>N<sub>4</sub> was improved through the formation of CeO<sub>2</sub>/g-C<sub>3</sub>N<sub>4</sub> and ZnO/g-C<sub>3</sub>N<sub>4</sub> composites. The composites formed from the metal acetate/melamine ratio of 0.136 mol % showed the highest dye degradation efficiency, which agreed with the photo-responses recorded from deposited films on FTO electrodes. Sustainable chemical manufacturing practices can utilize techniques developed in appendix A2, where the anodic electrochemical reactions are suggested as alternative pharmaceutical synthesis schemes.

Halogenated organic precursors/intermediates were successfully synthesized via an electrochemical chlorination method and verified with GC-MS, <sup>1</sup>H-NMR, and LC-MS. Electrochemical conversion cells were developed and utilized to understand the role of gaseous products in the conversion process. Applied voltage over specific lengths of time were evaluated to tune conversion. A facile electrochemical method was readily utilized to chemically produce the di-chloro-4P and mono-chloro-XCA substrates for the first time, which are not commercially available or registered in journal articles on SciFinder.



## 5.2 FUTURE DIRECTIONS

Immediately, the TMP and carbon nitride studies will be wrapped up and submitted for publication.

A larger scope includes: nanostructured materials are emerging as synergistic tools to supplement catalysts for enhanced water splitting and reaction kinetics. An industrially viable direction would consist of incorporating new functionalizing materials, such as the electrocatalysts described in this work, as replacements for PGMs in applications such as photocatalysis and water remediation. In this way, more sustainable and cost effective photocatalysts composites can be produced. Furthermore, functionalizing materials can highlight properties to improve overall solar efficiencies. Our study focused on distinct particles to understand the properties of a material that contribute to high performance. These understandings should be applied to hierarchical nano/micro-structures operating with high current conditions, high surface area, and robust electrodes. Overall, the stability, performance and cost are the main limitations of implementing electrocatalysts. The stability of earth-abundant materials is of high importance and should be referenced against the current DOE projections and targets. New systems and testing cells for long-term stability of electrocatalysts can be developed to resemble that of an implemented electrolyzer with a flow cell design.

On a technical side, further electrochemical technique utilization and development for both water splitting and non-water splitting applications can provide valuable mechanistic studies and insights. For example, electrochemical characterization of reactions beyond the potential window of aqueous electrolytes is beneficial. Furthermore, various electrochemical parameters and electrocatalyst selection can affect reaction conversion and selectivity's, etc. Utilizing the counter reaction to facilitate reactions other than the OER may be explored. Many of these future

suggestions are touched upon in the work provided for photoelectrochemical water remediation and electrochemical driven reactions in appendix A1 and A2

## REFERENCES

- (1) Gür, T. M. Perspective—Low-Carbon Electricity Is Great: What about “Less-Carbon”? *J. Electrochem. Soc.* **2017**, *164*, F1587–F1590.
- (2) Wang, T.; Guo, Y.; Zhou, Z.; Chang, X.; Zheng, J.; Li, X. Ni-Mo Nanocatalysts on N-Doped Graphite Nanotubes for Highly Efficient Electrochemical Hydrogen Evolution in Acid. *ACS Nano* **2016**, *10*, 10397–10403.
- (3) McCrory, C. C. L.; Jung, S.; Ferrer, I. M.; Chatman, S. M.; Peters, J. C.; Jaramillo, T. F. Benchmarking Hydrogen Evolving Reaction and Oxygen Evolving Reaction Electrocatalysts for Solar Water Splitting Devices. *J. Am. Chem. Soc.* **2015**, *137*, 4347–4357.
- (4) Laursen, A. B.; Wexler, R. B.; Whitaker, M. J.; Izett, E. J.; Calvino, K. U. D.; Hwang, S.; Rucker, R.; Wang, H.; Li, J.; Garfunkel, E.; et al. Climbing the Volcano of Electrocatalytic Activity While Avoiding Catalyst Corrosion: Ni<sub>3</sub>P, a Hydrogen Evolution Electrocatalyst Stable in Both Acid and Alkali. *ACS Catal.* **2018**, *8*, 4408–4419.
- (5) Yang, C. J. An Impending Platinum Crisis and Its Implications for the Future of the Automobile. *Energy Policy* **2009**, *37*, 1805–1808.
- (6) Sun, Y.; Delucchi, M.; Ogden, J. The Impact of Widespread Deployment of Fuel Cell Vehicles on Platinum Demand and Price. *Int. J. Hydrogen Energy* **2011**, *36*, 11116–11127.
- (7) Glaister, B. J.; Mudd, G. M. The Environmental Costs of Platinum-PGM Mining and Sustainability: Is the Glass Half-Full or Half-Empty? *Miner. Eng.* **2010**, *23*, 438–450.
- (8) Council, N. R. *Managing Materials for a Twenty-First Century Military*; National Academies Press, 2008.
- (9) Gattrell, M.; Kirk, D. W. The Electrochemical Oxidation of Aqueous Phenol at a Glassy Carbon Electrode. *Can. J. Chem. Eng.* **1990**, *68*, 997–1003.
- (10) Oliveira, R. T. S.; Salazar-Banda, G. R.; Santos, M. C.; Calegario, M. L.; Miwa, D. W.; Machado, S. A. S.; Avaca, L. A. Electrochemical Oxidation of Benzene on Boron-Doped Diamond Electrodes. *Chemosphere* **2007**, *66*, 2152–2158.
- (11) Fabian, D. M.; Hu, S.; Singh, N.; Houle, F. A.; Hisatomi, T.; Domen, K.; Osterloh, F. E.; Ardo, S. Particle Suspension Reactors and Materials for Solar-Driven Water Splitting. *Energy Environ. Sci.* **2015**, *8*, 2825–2850.
- (12) Jelena M., J.; Nikola M., R.; Nedeljko V., K.; Milan M., J. Electrocatalysis for Hydrogen Electrode Reactions in the Light of Fermi Dynamics and Structural Bonding Factors—I. Individual Electrocatalytic Properties of Transition Metals. *Int. J. Hydrogen Energy* **1998**, *23*, 1121–1156.
- (13) Callejas, J. F.; Read, C. G.; Roske, C. W.; Lewis, N. S.; Schaak, R. E. Synthesis, Characterization, and Properties of Metal Phosphide Catalysts for the Hydrogen-Evolution Reaction. *Chem. Mater.* **2016**, *28*, 6017–6044.

- (14) J. R. McKone; B. F. Sadler; C. A. Werlang; N. S. Lewis; H. B. Gray. Ni-Mo Nanopowders for Efficient Electrochemical Hydrogen Evolution. *ACS Catalysis*. 2013, pp 166–169.
- (15) Zhang, J.; Wang, T.; Liu, P.; Liao, Z.; Liu, S.; Zhuang, X.; Chen, M.; Zschech, E.; Feng, X. Efficient Hydrogen Production on MoNi<sub>4</sub> Electrocatalysts with Fast Water Dissociation Kinetics. *Nat. Commun.* **2017**, *8*, 1–8.
- (16) Popczun, E. J.; McKone, J. R.; Read, C. G.; Biacchi, A. J.; Wiltout, A. M.; Lewis, N. S.; Schaak, R. E. Nanostructured Nickel Phosphide as an Electrocatalyst for the Hydrogen Evolution Reaction. *J. Am. Chem. Soc.* **2013**, *135*, 9267–9270.
- (17) Koenigsmann, C.; Zhou, W. P.; Adzic, R. R.; Sutter, E.; Wong, S. S. Size-Dependent Enhancement of Electrocatalytic Performance in Relatively Defect-Free, Processed Ultrathin Platinum Nanowires. *Nano Lett.* **2010**, *10*, 2806–2811.
- (18) McEnaney, J. M.; Chance Crompton, J.; Callejas, J. F.; Popczun, E. J.; Biacchi, A. J.; Lewis, N. S.; Schaak, R. E. Amorphous Molybdenum Phosphide Nanoparticles for Electrocatalytic Hydrogen Evolution. *Chem. Mater.* **2014**, *26*, 4826–4831.
- (19) Chen, Z.; Dinh, H. N.; Miller, E. Photoelectrochemical Water Splitting; SpringerBriefs in Energy. Springer New York 2013.
- (20) Moniz, S. J. A.; Shevlin, S. A.; Martin, D. J.; Guo, Z. X.; Tang, J. Visible-Light Driven Heterojunction Photocatalysts for Water Splitting—a Critical Review. *Energy Environ. Sci.* **2015**, *8*, 731–759.
- (21) Roske, C. W.; Popczun, E. J.; Seger, B.; Read, C. G.; Pedersen, T.; Hansen, O.; Vesborg, P. C. K.; Brunschwig, B. S.; Schaak, R. E.; Chorkendorff, I.; et al. Comparison of the Performance of Cop-Coated and Pt-Coated Radial Junction N+p-Silicon Microwire-Array Photocathodes for the Sunlight-Driven Reduction of Water to H<sub>2</sub>(G). *J. Phys. Chem. Lett.* **2015**, *6*, 1679–1683.
- (22) Saraswat, S. K.; Rodene, D. D.; Gupta, R. B. Recent Advancements in Semiconductor Materials for Photoelectrochemical Water Splitting for Hydrogen Production Using Visible Light. *Renew. Sustain. Energy Rev.* **2018**, *89*, 228–248.
- (23) Herrero, J.; Gutiérrez, M. T. Photoelectrochemical Measurements of Amorphous Silicon Thin Films. *Electrochim. Acta* **1991**, *36*, 915–920.
- (24) Nyankson, E.; Rodene, D.; Gupta, R. B. Advancements in Crude Oil Spill Remediation Research after the Deepwater Horizon Oil Spill. *Water. Air. Soil Pollut.* **2016**, *227*.
- (25) Callejas, J. F.; McEnaney, J. M.; Read, C. G.; Crompton, J. C.; Biacchi, A. J.; Popczun, E. J.; Gordon, T. R.; Lewis, N. S.; Schaak, R. E. Electrocatalytic and Photocatalytic Hydrogen Production from Acidic and Neutral-PH Aqueous Solutions Using Iron Phosphide Nanoparticles. *ACS Nano* **2014**, *8*, 11101–11107.
- (26) Laursen, A. B.; Patraju, K. R.; Whitaker, M. J.; Retuerto, M.; Sarkar, T.; Yao, N.; Ramanujachary, K. V.; Greenblatt, M.; Dismukes, G. C. Nanocrystalline Ni<sub>5</sub>P<sub>4</sub>: A Hydrogen Evolution Electrocatalyst of Exceptional Efficiency in Both Alkaline and Acidic Media. *Energy Environ. Sci.* **2015**, *8*, 1027–1034.

- (27) Miyazaki, K.; Islam, N. Nanotechnology Systems of Innovation-An Analysis of Industry and Academia Research Activities. *Technovation* **2007**, *27*, 661–675.
- (28) Islam, N.; Miyazaki, K. An Empirical Analysis of Nanotechnology Research Domains. *Technovation* **2010**, *30*, 229–237.
- (29) Chen, Z.; Jaramillo, T. F.; Deutsch, T. G.; Kleiman-Shwarsstein, A.; Forman, A. J.; Gaillard, N.; Garland, R.; Takanabe, K.; Heske, C.; Sunkara, M.; et al. Accelerating Materials Development for Photoelectrochemical Hydrogen Production: Standards for Methods, Definitions, and Reporting Protocols. *J. Mater. Res.* **2010**, *25*, 3–16.
- (30) Chai, Z.; Zeng, T. T.; Li, Q.; Lu, L. Q.; Xiao, W. J.; Xu, D. Efficient Visible Light-Driven Splitting of Alcohols into Hydrogen and Corresponding Carbonyl Compounds over a Ni-Modified CdS Photocatalyst. *J. Am. Chem. Soc.* **2016**, *138*, 10128–10131.
- (31) Lewis, N. S.; Nocera, D. G. Powering the Planet: Chemical Challenges in Solar Energy Utilization. *Proc. Natl. Acad. Sci. U. S. A.* **2006**, *103*, 15729–15735.
- (32) McKay, I. S.; Schwalbe, J. A.; Goodman, E. D.; Willis, J. J.; Majumdar, A.; Cargnello, M. Elucidating the Synergistic Mechanism of Nickel-Molybdenum Electrocatalysts for the Hydrogen Evolution Reaction. *MRS Commun.* **2016**, *6*, 241–246.
- (33) Li, Y.; Wang, H.; Xie, L.; Liang, Y.; Hong, G.; Dai, H. MoS<sub>2</sub> Nanoparticles Grown on Graphene: An Advanced Catalyst for the Hydrogen Evolution Reaction. *J. Am. Chem. Soc.* **2011**, *133*, 7296–7299.
- (34) McKone, J. R.; Sadtler, B. F.; Werlang, C. A.; Lewis, N. S.; Gray, H. B.; J. R. McKone; B. F. Sadtler; C. A. Werlang; N. S. Lewis; H. B. Gray; et al. Ni-Mo Nanopowders for Efficient Electrochemical Hydrogen Evolution. *ACS Catal.* **2013**, *3*, 166–169.
- (35) Patil, R. B.; Mantri, A.; House, S. D.; Yang, J. C.; McKone, J. R. Enhancing the Performance of Ni-Mo Alkaline Hydrogen Evolution Electrocatalysts with Carbon Supports. *ACS Appl. Energy Mater.* **2019**, *2*, 2524–2533.
- (36) Nahar, L.; Farghaly, A. A.; Esteves, R. J. A.; Arachchige, I. U. Shape Controlled Synthesis of Au/Ag/Pd Nanoalloys and Their Oxidation-Induced Self-Assembly into Electrocatalytically Active Aerogel Monoliths. *Chem. Mater.* **2017**, *29*, 7704–7715.
- (37) Yu, F.; Yu, L.; Mishra, I. K.; Yu, Y.; Ren, Z. F.; Zhou, H. Q. Recent Developments in Earth-Abundant and Non-Noble Electrocatalysts for Water Electrolysis. *Mater. Today Phys.* **2018**, *7*, 121–138.
- (38) Hellstern, T. R.; Kibsgaard, J.; Tsai, C.; Palm, D. W.; King, L. A.; Abild-Pedersen, F.; Jaramillo, T. F. Investigating Catalyst-Support Interactions to Improve the Hydrogen Evolution Reaction Activity of Thiomolybdate [Mo<sub>3</sub>S<sub>13</sub>]<sup>2-</sup> Nanoclusters. *ACS Catal.* **2017**, *7*, 7126–7130.
- (39) McKone, J. R.; Sadtler, B. F.; Werlang, C. A.; Lewis, N. S.; Gray, H. B. Ni-Mo Nanopowders for Efficient Electrochemical Hydrogen Evolution. *ACS Catal.* **2013**, *3*, 166–169.
- (40) Metalary <https://www.metalary.com> (accessed Apr 14, 2019).

- (41) Schalenbach, M.; Speck, F. D.; Ledendecker, M.; Kasian, O.; Goehl, D.; Mingers, A. M.; Breitbach, B.; Springer, H.; Cherevko, S.; Mayrhofer, K. J. J. Nickel-Molybdenum Alloy Catalysts for the Hydrogen Evolution Reaction: Activity and Stability Revised. *Electrochim. Acta* **2018**, *259*, 1154–1161.
- (42) Zhang, J. G.; Zhang, S. M.; Li, S.; Dai, H.; Hu, Q.; Zhang, B.; Wang, L. M. Electrocatalytic Properties of Nickel Foam-Based Ni-Mo, Ni +Mo and Ni+Mo/Ni-Mo Electrodes for Hydrogen Evolution Reaction. *Mater. Sci. Forum* **2018**, *921*, 134–140.
- (43) Zhang, T.; Liu, X.; Cui, X.; Chen, M.; Liu, S.; Geng, B. Colloidal Synthesis of Mo–Ni Alloy Nanoparticles as Bifunctional Electrocatalysts for Efficient Overall Water Splitting. *Adv. Mater. Interfaces* **2018**, *5*, 1–6.
- (44) Highfield, J. Advances and Recent Trends in Heterogeneous Photo(Electro)-Catalysis for Solar Fuels and Chemicals. *Molecules* **2015**, *20*, 6739–6793.
- (45) Wang, T.; Wang, X.; Liu, Y.; Zheng, J.; Li, X. A Highly Efficient and Stable Biphasic Nanocrystalline Ni-Mo-N Catalyst for Hydrogen Evolution in Both Acidic and Alkaline Electrolytes. *Nano Energy* **2016**, *22*, 111–119.
- (46) Hao, J. Y.; Wang, Y. Y.; Tong, X. L.; Jin, G. Q.; Guo, X. Y. Photocatalytic Hydrogen Production over Modified SiC Nanowires under Visible Light Irradiation. *Int. J. Hydrogen Energy* **2012**.
- (47) Sharma, S.; Ghoshal, S. K. Hydrogen the Future Transportation Fuel: From Production to Applications. *Renew. Sustain. Energy Rev.* **2015**, *43*, 1151–1158.
- (48) Zhang, L.; Xiong, K.; Nie, Y.; Wang, X.; Liao, J.; Wei, Z. Sputtering Nickel-Molybdenum Nanorods as an Excellent Hydrogen Evolution Reaction Catalyst. *J. Power Sources* **2015**, *297*, 413–418.
- (49) Xiong, J.; Li, J.; Shi, J.; Zhang, X.; Suen, N.; Liu, Z. In-Situ Engineering of Double Phase Interface in Mo / Mo<sub>2</sub> C Heteronanoseets for Boosted Hydrogen Evolution Reaction. *430081*, 1–16.
- (50) Wang, S.; Wang, J.; Zhu, M.; Bao, X.; Xiao, B.; Su, D.; Li, H.; Wang, Y. Molybdenum-Carbide-Modified Nitrogen-Doped Carbon Vesicle Encapsulating Nickel Nanoparticles: A Highly Efficient, Low-Cost Catalyst for Hydrogen Evolution Reaction. *J. Am. Chem. Soc.* **2015**, *137*, 15753–15759.
- (51) Moni, T. P.; Splitting, W. Supplementary Information Three-Dimensional Porous MoNi<sub>4</sub> Networks Constructed by Nanosheets as Bifunctional Electrocatalysts for Overall. **2017**.
- (52) Mourdikoudis, S.; Simeonidis, K.; Vilalta-Clemente, A.; Tuna, F.; Tsiaoussis, I.; Angelakeris, M.; Dendrinou-Samara, C.; Kalogirou, O. Controlling the Crystal Structure of Ni Nanoparticles by the Use of Alkylamines. *J. Magn. Magn. Mater.* **2009**, *321*, 2723–2728.
- (53) Luo, X.; Chen, Y.; Yue, G. H.; Peng, D. L.; Luo, X. Preparation of Hexagonal Close-Packed Nickel Nanoparticles via a Thermal Decomposition Approach Using Nickel Acetate Tetrahydrate as a Precursor. *J. Alloys Compd.* **2009**, *476*, 864–868.

- (54) Zhang, H. T.; Wu, G.; Chen, X. H.; Qiu, X. G. Synthesis and Magnetic Properties of Nickel Nanocrystals. *Mater. Res. Bull.* **2006**, *41*, 495–501.
- (55) Carenco, S.; Boissière, C.; Nicole, L.; Sanchez, C.; Le Floch, P.; Mézailles, N. Controlled Design of Size-Tunable Monodisperse Nickel Nanoparticles. *Chem. Mater.* **2010**, *22*, 1340–1349.
- (56) Crist, V. Handbooks of Monochromatic XPS Spectra. *Phys. Status Solidi* **1999**, *198*, 5–21.
- (57) Wang, X.; Su, R.; Aslan, H.; Kibsgaard, J.; Wendt, S.; Meng, L.; Dong, M.; Huang, Y.; Besenbacher, F. Tweaking the Composition of NiMoZn Alloy Electrocatalyst for Enhanced Hydrogen Evolution Reaction Performance. *Nano Energy* **2015**, *12*, 9–18.
- (58) Zhang, Y.; Ouyang, B.; Xu, J.; Chen, S.; Rawat, R. S.; Fan, H. J. 3D Porous Hierarchical Nickel-Molybdenum Nitrides Synthesized by RF Plasma as Highly Active and Stable Hydrogen-Evolution-Reaction Electrocatalysts. *Adv. Energy Mater.* **2016**, *6*, 1600221.
- (59) Grosvenor, A. P.; Biesinger, M. C.; Smart, R. S. C.; McIntyre, N. S. New Interpretations of XPS Spectra of Nickel Metal and Oxides. *Surf. Sci.* **2006**, *600*, 1771–1779.
- (60) CHEN, X. Titanium Dioxide Nanomaterials and Their Energy Applications. *Chinese Journal of Catalysis*. 2009.
- (61) Liu, J.; Liu, Y.; Liu, N.; Han, Y.; Zhang, X.; Huang, H.; Lifshitz, Y.; Lee, S.-T.; Zhong, J.; Kang, Z. Metal-Free Efficient Photocatalyst for Stable Visible Water Splitting via a Two-Electron Pathway. *Science (80-. )*. **2015**, *347*, 970 LP – 974.
- (62) Andrews, J.; Shabani, B. The Role of Hydrogen in a Global Sustainable Energy Strategy. *Wiley Interdiscip. Rev. Energy Environ.* **2014**, *3*, 474–489.
- (63) Qadrdan, M.; Shayegan, J. Economic Assessment of Hydrogen Fueling Station, a Case Study for Iran. *Renew. Energy* **2008**, *33*, 2525–2531.
- (64) Pu, Z.; Liu, Q.; Tang, C.; Asiri, A. M.; Sun, X. Ni<sub>2</sub>P Nanoparticle Films Supported on a Ti Plate as an Efficient Hydrogen Evolution Cathode. *Nanoscale* **2014**, *6*, 11031–11034.
- (65) Feng, L.; Vrabel, H.; Bensimon, M.; Hu, X. Easily-Prepared Dinickel Phosphide (Ni<sub>2</sub>P) Nanoparticles as an Efficient and Robust Electrocatalyst for Hydrogen Evolution. *Phys. Chem. Chem. Phys.* **2014**, *16*, 5917–5921.
- (66) Rodene, D. D.; Eladgham, E. H.; Gupta, R. B.; Arachchige, I. U.; Tallapally, V. Crystal Structure and Composition-Dependent Electrocatalytic Activity of Ni-Mo Nanoalloys for Water Splitting to Produce Hydrogen. *ACS Appl. Energy Mater.* **2019**, *2*, 7112–7120.
- (67) Kucernak, A. R. J.; Naranammalpuram Sundaram, V. N. Nickel Phosphide: The Effect of Phosphorus Content on Hydrogen Evolution Activity and Corrosion Resistance in Acidic Medium. *J. Mater. Chem. A* **2014**, *2*, 17435–17445.
- (68) Callejas, J. F.; Read, C. G.; Popczun, E. J.; McEnaney, J. M.; Schaak, R. E. Nanostructured Co<sub>2</sub>P Electrocatalyst for the Hydrogen Evolution Reaction and Direct Comparison with Morphologically Equivalent CoP. *Chem. Mater.* **2015**, *27*, 3769–3774.
- (69) Popczun, E. J.; Read, C. G.; Roske, C. W.; Lewis, N. S.; Schaak, R. E. Highly Active

- Electrocatalysis of the Hydrogen Evolution Reaction by Cobalt Phosphide Nanoparticles. *Angew. Chemie - Int. Ed.* **2014**, *53*, 5427–5430.
- (70) Popczun, E. J.; Roske, C. W.; Read, C. G.; Crompton, J. C.; McEnaney, J. M.; Callejas, J. F.; Lewis, N. S.; Schaak, R. E. Highly Branched Cobalt Phosphide Nanostructures for Hydrogen-Evolution Electrocatalysis. *J. Mater. Chem. A* **2015**, *3*, 5420–5425.
- (71) Liyanage, D. R.; Danforth, S. J.; Liu, Y.; Bussell, M. E.; Brock, S. L. Simultaneous Control of Composition, Size, and Morphology in Discrete Ni<sub>2</sub>-XCox P Nanoparticles. *Chem. Mater.* **2015**, *27*, 4349–4357.
- (72) Henkes, A. E.; Schaak, R. E. Trioctylphosphine: A General Phosphorus Source for the Low-Temperature Conversion of Metals into Metal Phosphides. *Chem. Mater.* **2007**, *19*, 4234–4242.
- (73) Henkes, A. E.; Vasquez, Y.; Schaak, R. E. Converting Metals into Phosphides: A General Strategy for the Synthesis of Metal Phosphide Nanocrystals. *J. Am. Chem. Soc.* **2007**, *129*, 1896–1897.
- (74) Chiang, R. K.; Chiang, R. T. Formation of Hollow Ni<sub>2</sub>P Nanoparticles Based on the Nanoscale Kirkendall Effect. *Inorg. Chem.* **2007**, *46*, 369–371.
- (75) Ha, D. H.; Moreau, L. M.; Bealing, C. R.; Zhang, H.; Hennig, R. G.; Robinson, R. D. The Structural Evolution and Diffusion during the Chemical Transformation from Cobalt to Cobalt Phosphide Nanoparticles. *J. Mater. Chem.* **2011**, *21*, 11498–11510.
- (76) Li, J.; Yan, M.; Zhou, X.; Huang, Z. Q.; Xia, Z.; Chang, C. R.; Ma, Y.; Qu, Y. Mechanistic Insights on Ternary Ni<sub>2</sub>-xCoxP for Hydrogen Evolution and Their Hybrids with Graphene as Highly Efficient and Robust Catalysts for Overall Water Splitting. *Adv. Funct. Mater.* **2016**, *26*, 6785–6796.
- (77) Read, C. G.; Callejas, J. F.; Holder, C. F.; Schaak, R. E. General Strategy for the Synthesis of Transition Metal Phosphide Films for Electrocatalytic Hydrogen and Oxygen Evolution. *ACS Appl. Mater. Interfaces* **2016**, *8*, 12798–12803.
- (78) Huang, Z.; Chen, Z.; Chen, Z.; Lv, C.; Meng, H.; Zhang, C. Ni<sub>12</sub>P<sub>5</sub> Nanoparticles as an Efficient Catalyst for Hydrogen Generation via Electrolysis and Photoelectrolysis. *ACS Nano* **2014**, *8*, 8121–8129.
- (79) Mori, K.; Kakudo, H.; Yamashita, H. Creation of Nickel-Based Active Species within a Macroporous Acidic Resin: A Noble-Metal-Free Heterogeneous Catalyst for Visible-Light-Driven H<sub>2</sub> Evolution from Water.
- (80) Xu, M.; He, G.; Li, Z.; He, F.; Gao, F.; Su, Y.; Zhang, L.; Yang, Z.; Zhang, Y. A Green Heterogeneous Synthesis of N-Doped Carbon Dots and Their Photoluminescence Applications in Solid and Aqueous States. *Nanoscale* **2014**.
- (81) Han, X.; Xu, D.; An, L.; Hou, C.; Li, Y.; Zhang, Q.; Wang, H. Ni-Mo Nanoparticles as Co-Catalyst for Drastically Enhanced Photocatalytic Hydrogen Production Activity over g-C<sub>3</sub>N<sub>4</sub>. *Appl. Catal. B Environ.* **2019**, *243*, 136–144.
- (82) Dincer, I.; Zamfirescu, C. Sustainable Hydrogen Production. *Sustain. Hydrog. Prod.* **2016**,



305, 1–479.

- (83) Basha, S. A.; Gopal, K. R.; Jebaraj, S. A Review on Biodiesel Production, Combustion, Emissions and Performance. *Renew. Sustain. Energy Rev.* **2009**, *13*, 1628–1634.
- (84) Cho, K.; Kwon, D.; Hoffmann, M. R. Electrochemical Treatment of Human Waste Coupled with Molecular Hydrogen Production. *RSC Adv.* **2014**, *4*, 4596–4608.
- (85) Hasvold, L. A.; Wang, W.; Gwaltney, S. L.; Rockway, T. W.; Nelson, L. T. J.; Mantei, R. A.; Fakhoury, S. A.; Sullivan, G. M.; Li, Q.; Lin, N. H.; et al. Pyridone-Containing Farnesyltransferase Inhibitors: Synthesis and Biological Evaluation. *Bioorganic Med. Chem. Lett.* **2003**, *13*, 4001–4005.
- (86) Yavari, I.; Souiri, S. Efficient Synthesis of Functionalized 2-Pyridones from Malonyl Dichloride, Alkylamines and Dimethyl Acetylenedicarboxylate. *Synlett* **2007**, *2007*, 2969–2970.
- (87) Neo, A. G.; Carrillo, R. M.; Barriga, S.; Moman, E.; Marcaccini, S.; Marcos, C. F. Multicomponent Synthesis of Highly Substituted 2-Pyridones. *Synlett* **2007**, *2007*, 327–329.
- (88) McLafferty, F. W. Mass Spectrometric Analysis. Aliphatic Halogenated Compounds. *Anal. Chem.* **1962**, *34*, 2–15.
- (89) Petrovic, M.; Diaz, A.; Ventura, F.; Barceló, D. Simultaneous Determination of Halogenated Derivatives of Alkylphenol Ethoxylates and Their Metabolites in Sludges, River Sediments, and Surface, Drinking, and Wastewaters by Liquid Chromatography–Mass Spectrometry. *Anal. Chem.* **2001**, *73*, 5886–5895.
- (90) Vos, J. G.; Koper, M. T. M. Measurement of Competition between Oxygen Evolution and Chlorine Evolution Using Rotating Ring-Disk Electrode Voltammetry. *J. Electroanal. Chem.* **2018**, *819*, 260–268.
- (91) Maras, N.; Selic, L.; Cusak, A. Processes for Preparing Dolutegravir and Cabotegravir and Analogues Thereof. Google Patents July 2, 2019.
- (92) Boscha, M. E.; Sánchezb, A. J. R.; Rojasc, F. S.; Ojedac, C. B. Recent Developments in the Analytical Determination of Cefadroxil. *亚洲药物制剂科学* **2008**, *3*, 217–232.

## **Appendix**

**Appendix A1. Organic Oxidation – Tailoring the Photocatalytic Activity of Cerium Oxide and Zinc Oxide Modified Graphitic Carbon Nitride Nano-Composites Towards Indigo Carmine Degradation**

The photocatalytic activity of g-C<sub>3</sub>N<sub>4</sub> for the degradation of indigo carmine was enhanced through the preparation of CeO<sub>2</sub>/g-C<sub>3</sub>N<sub>4</sub> and ZnO/g-C<sub>3</sub>N<sub>4</sub> heterojunction composites. The preparation of composites was achieved through a facile thermal oxidation and condensation mechanism. A ratio of metal acetate precursors (0.136 mol%) to melamine gave the highest activity. XRD, FT-IR, and XPS analyses performed by the Dr. El-Shall group indicated that the crystal and chemical structures were unaltered and matched that of native g-C<sub>3</sub>N<sub>4</sub>. The composites showed improved optical properties over native g-C<sub>3</sub>N<sub>4</sub> for a lowered electron-hole recombination rate and increased the band gap (ca. 2.81) through photoluminescence and dr-UV-Vis analyses, respectively. The photocatalysts were created into electrode where photocurrent and charge generation were shown via a photoelectrochemical approach. A nearly full degradation of indigo carmine was reported after 60 min of photocatalysis.

## A.1 INTRODUCTION

The degradation of colored dyes is a direct and easy way to evaluate photocatalysts for water remediation applications such as oil spills and fertilizer pollutants.<sup>22,24,79,80</sup> The thermal condensation of powders containing melamine and cerium acetate or zinc acetate resulted in various g-C<sub>3</sub>N<sub>4</sub> composites for the improved photo-degradation of indigo carmine.<sup>81</sup> The condensation of melamine resulted pure g-C<sub>3</sub>N<sub>4</sub> confirmed by XRD and FT-IR analyses (Figure A.1). Cerium or zinc metal precursors were added to form metal oxide composites with various metal loadings (0–0.688 mol %). Single component metal oxides were also synthesized via a similar procedure without the addition of melamine. A physical mixture of native g-C<sub>3</sub>N<sub>4</sub> and the synthesized metal oxides was prepared to compare against the composite samples.

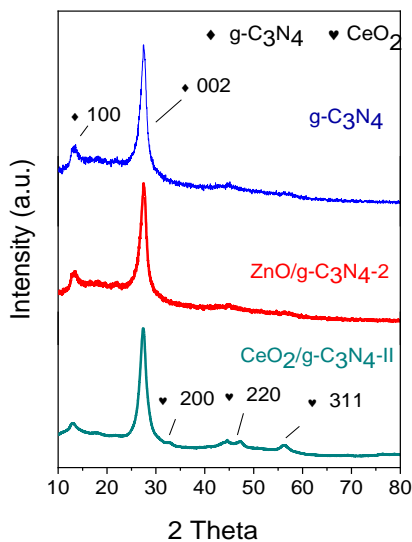


**Figure A.1** XRD patterns for cerium and zinc oxide carbon nitride composites with 0.136 mol% precursor ratios.

## A.2 EXPERIMENTAL SECTION

**A.2.1 Fabrication of Working Electrodes.** To prepare the working electrode catalyst slurry, 5 mg of catalyst was ground and dispersed in a mixture of water (18 M $\Omega$ ) and Nafion solution. To aid in creating a homogeneous distribution of Nafion solution, a portion of water was utilized to dilute the Nafion solution prior to addition with the bulk solution. The diluted Nafion solution was then added to the slurry mixture (8:2, v:v) and agitated by sonication for 30 min. The solution ratios may be altered by adding common organic solvents (e.g., 2-propanol, ethanol) to adjust for film adhesion, viscosity, hydrophobicity, and drying rate depending on the specific sample. The ratio provided gave the best films.

The fabrication of working electrodes was performed. A sheet of fluorinated-tin oxide on glass (FTO; 9–11  $\Omega$ /sq, Delta Technologies LTD) was broken to obtain pieces with the proper dimensions of an electrode. The FTO substrates were cleaned by sonication in a solution of ethanol and acetone (1:1, v:v). The FTO substrates were rinsed with water (18 M $\Omega$ ) and allowed to dry. Once dry, the FTO substrate was connected to a partially stripped silver coated copper wire (chemical-resistant wire, McMaster-Carr) via Ag paint (PELCO colloidal silver paint, Ted Pella). To strengthen and insulate the ohmic contact, an epoxy coating (Henkel Loctite Hysol 9462) was

applied to the contact. More epoxy was applied to insulate the FTO substrate; care was taken to leave an active area exposed as a templet for drop-casting the catalyst slurry. Once the epoxy hardened (12 h), the catalyst slurry was drop-casted onto the FTO electrode in 5-10  $\mu\text{L}$  aliquots. Each aliquot was allowed to dry completely before the next addition. A total of 50  $\mu\text{L}$  was added for each catalyst slurry and allowed to dry at 80  $^{\circ}\text{C}$  for at least 8 h. The area of the templated FTO electrodes was found to be 0.112  $\text{cm}^2$ . The fabricated FTO electrodes were cleaned and utilized for multiple catalyst slurries by dispersing the film and cleaning the FTO surface with ethanol.

**A.2.2 Photoelectrochemical Measurements.** Photoelectrochemical measurements were performed utilizing a CH Instruments electrochemical analyzer/workstation (CHI660E). All photoelectrochemical measurements were conducted in a quartz beaker utilized as a conventional three-electrode cell. The cell was designed to be irradiated from the bottom with a UVP compact UV lamp (UVGL-25 4W LW/SW) set to 365 nm. A platinum (Pt) wire and Ag/AgCl (1 M KCl) were utilized as the counter and reference electrodes (CH Instruments Inc.), respectively. A solution of aqueous 0.1 M  $\text{Na}_2\text{SO}_4$  was utilized as the electrolyte.

## **A.3 RESULTS AND DISCUSSIONS**

### **A.3.1 Photoelectrochemical Catalyst Characterization**

The interfacial charge separation dynamics of the generated photoactive species were measured by monitoring the photocurrent density of the catalysts immobilized on an FTO-based electrode. To determine if the composites had an increased ability to generate photo-current compared to a physical mixture of metal oxide powders and native carbon nitride, the photo-responses were recorded. The measured current was observed to change abruptly in response to the light source being switched on and off (Figure A.2). The high photocurrent responses for the  $\text{CeO}_2/\text{g-C}_3\text{N}_4\text{-II}$  and  $\text{ZnO}/\text{g-C}_3\text{N}_4\text{-2}$  composites, implies that there is a larger charge-transfer efficiency for the composites than  $\text{g-C}_3\text{N}_4$  and the physical mixtures. Moreover, the photo-currents of the  $\text{CeO}_2/\text{g-C}_3\text{N}_4\text{-II}$  composite were significantly higher than all samples including the ZnO composite. The current densities generated by the samples were consistent with the catalytic activities found in this study, where the composites that exhibited the highest photo-voltage degraded the dye with the highest efficiency (Figure A.2). Therefore, the photo-current measured

by a photoelectrochemical approach directly correlated to photocatalytic activity. Furthermore, incorporating metal precursors during the synthesis of the composites aided in boosting charge transfer over the addition of metal oxide powders with carbon nitride post synthesis.

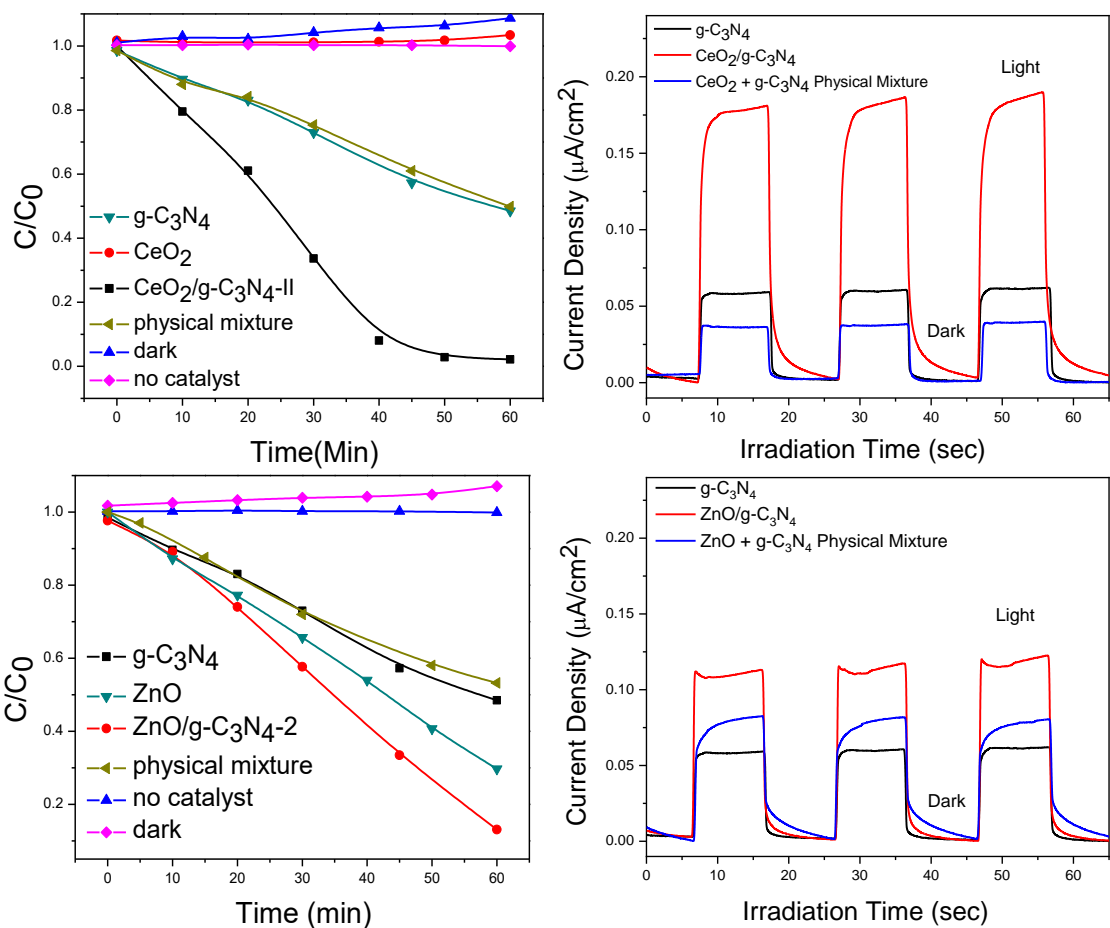


**Figure A.2** Transient photocurrent of g-C<sub>3</sub>N<sub>4</sub>, CeO<sub>2</sub>/g-C<sub>3</sub>N<sub>4</sub>, ZnO/g-C<sub>3</sub>N<sub>4</sub> and their physical mixture under the excitation of 365 nm UV light radiation in 0.1 M Na<sub>2</sub>SO<sub>4</sub> and the correlation to indigo carmine degradation.

## A.4 CONCLUSION

The photocatalytic efficiency of g-C<sub>3</sub>N<sub>4</sub> was improved through the formation of CeO<sub>2</sub>/g-C<sub>3</sub>N<sub>4</sub> and ZnO/g-C<sub>3</sub>N<sub>4</sub> composites. The composites were prepared by a 1-step thermal condensation reaction of melamine mixed with the respected metal acetates to give smooth aggregated morphologies. XRD, FT-IR, and XPS analyses confirmed that no change in the chemical structure of g-C<sub>3</sub>N<sub>4</sub> resulted from the formation of metal oxide composites. The incorporation of metal oxides into g-C<sub>3</sub>N<sub>4</sub> was proven to decrease the rate of charge recombination, further enhancing the degradation of model molecules representing key organic pollutants. Various amounts of metal acetate precursors were incorporated during composite synthesis. The metal acetate/melamine ratio of 0.136 mol % (samples II) showed the highest dye degradation efficiency. Separation of the excited electron-hole pairs was confirmed for all heterojunction composites by photoluminescence. The composites exhibited a good photo-response when deposited on FTO electrodes. The 1-step composites were compared against composites utilizing a physical incorporation of metal oxide particles into native g-C<sub>3</sub>N<sub>4</sub> and showed a better performance and properties over the physical composites. The proposed mechanism for the degradation of indigo carmine was confirmed to be facilitated by  $\cdot\text{O}_2^-$  through chemical charge scavenger reaction studies.



## **Appendix A2. Organic Chlorination – Electrochemical Chlorination of Heterocyclic Pyridones**

A shift towards sustainable chemical manufacturing practices has generated interest in direct electrochemical organic syntheses. Heterocyclic substrates, specifically pyridone-based compounds, are chemically relevant for their roles in biological systems and, therefore, pharmaceuticals. Herein, a facile bench-scale electrochemical-controlled chlorination scheme has been developed and demonstrated for three heterocyclic substrates: *n*-methyl-2-pyridone (2MP, compound A), 1-(2,2-dimethoxyethyl)-4(1*H*)-pyridinone (4P, compound B), and 1,6-dimethyl-4-oxo-1,4-dihydropyridine-3-carboxylic acid (XCA, compound C). A divided H-cell was implemented to separate any oxidative and reductive reactions. Cyclic voltammetry was utilized to gain an understanding of the electrochemical oxidation/reduction; however, the chlorination reactions were found to occur outside of the aqueous potential window. The substrate chlorination reactions were experimentally determined to follow a chlorine gas mechanism at the graphite anode (positive electrode) in 0.5 M HCl, and hydrogen was readily produced at the cathode (negative electrode) as a counter reaction. Various applied voltages were held over multiple periods of time as conversion parameters utilized to control the formation of chlorinated products. The formation of chlorination products was confirmed via GC-MS, <sup>1</sup>H-NMR, and LC-MS. Compounds A and B exhibited both mono- and di-chlorination additions to heterocyclic-carbons. For comparison, a gaseous cell was devised to elucidate the role of gaseous chlorine/oxygen in the conversion of substrates. It was found that the evolved gases can facilitate chlorine additions independently and play a role in the chlorine addition mechanisms. A high conversion was achieved (ca. 91–100 % starting materials), and the rate of conversion for each substrate was mostly linear. It is suggested here that a facile bench-scale apparatus can be utilized to electrochemically-facilitate chlorine additions to the heterocyclic organic substrates.

## A2.1 INTRODUCTION

Current fossil energy production is at the highest ever reported in history and is leading to climate change and sustainability concerns.<sup>82,83</sup> Therefore, energy production is shifting away from fossil fuel resources and towards solar energy.<sup>82</sup> While energy demands continue to grow, an interesting situation is developing, where the demand can be met by alternative energy sources before the end of this century. Simultaneously, chemical production schemes are continuously being reevaluated to meet changing policies and costs in the context of the new supply of renewable electricity. Subsequently, electrochemical driven reactions can provide a controllable chemical production scheme powered by the renewable electricity.<sup>84</sup> Furthermore, renewable-powered electrochemistry is proposed herein to facilitate electrochemical chlorine synthesis for scalable chemical production.

Heterocyclic chemical compounds occur naturally in biologic systems and have a wide range of applications.<sup>85-87</sup> Literature is scarce for the functionalization of pyridone and pyridone-based molecules. Pyridone-based molecules are relatively stable compounds. A facile electrochemical chlorination scheme is proposed to functionalize heterocyclic-carbon atoms for use as precursor molecules, synthesis-intermediates, or chemical products such as an active-ingredient for pharmaceuticals.

In this work, a bench-scale electrochemical scheme was developed as an alternative to wet-chemical chlorination processes, utilizing aqueous HCl and electricity to form an in-situ chlorinating agent. The chlorination reactions proceeded at various voltages and reaction times for the three heterocyclic substrates. Conversion efficiencies were recorded as the change in MS peak area with time as multiple intermediates/products were formed which further react into to form

sequential products. Chlorine gas was observed to be generated and found to actively participate in the conversion mechanism. The chlorinated substrates were confirmed through GC-MS, <sup>1</sup>H-NMR, and LC-MS. Further optimization and electrochemical characterization are needed to regulate the chlorine gas generation while maintaining a high conversion efficiency.

## A2.2 EXPERIMENTAL SECTION

**A2.2.1 Materials.** N-methyl-2-pyridone (2MP, >99%), 1,6-dimethyl-4-oxo-1,4-dihydropyridine-3-carboxylic acid (XCA, 95%), dichloromethane (DCM, GC grade), cesium carbonate (Cs<sub>2</sub>CO<sub>3</sub>), *N,N*-dimethylformamide (DMF), silica gel (40–60 μm), and deuterated chloroform (CDCl<sub>3</sub>) were purchased from Sigma Aldrich. KOH (reagent grade, 90%) was purchased from Acros Organics. Graphite rods (6.15 mm x 102 mm, 99.9995%) and chloroacetaldehyde dimethyl acetal were purchased from Alfa Aesar. Rectangular graphite electrodes (SK-50) were purchased from IKA. Henkel Loctite Hysol 9462 epoxy adhesives were purchased from Ellsworth Adhesives. Hydrochloric acid solution (HCl, 1 N), 0.2 μm filters (MDI, SY13TG), hexanes, ethyl acetate (EtOAc), methanol (MeOH), and dichloromethane (CH<sub>2</sub>Cl<sub>2</sub>) were purchased from Fisher Scientific. HCl solution was diluted with nano-pure water (ddH<sub>2</sub>O, 18 Ω) obtained from a Barnstead Diamond RO filtration system to obtain 0.5 M HCl and 0.1 M KOH. A simple electrochemical H-cell (RRPG060) was purchased from Pine Research Instrumentation. A Hg/HgSO<sub>4</sub> (Sat. Na<sub>2</sub>SO<sub>4</sub>) reference electrode (CHI151), platinum wire counter electrode (CHI115), and polishing kit (CHI120) were purchased from CH Instruments. 1,4-dihydro-4-pyridone was purchased from Milipore EMD. All reagents and solvents were used as received, unless otherwise specified.

**A2.2.2 Synthesis of 1-(2,2-Dimethoxyethyl)-4(1H)-Pyridinone.** 1,4-dihydro-4-pyridone (2.28 g, 24.0 mmol), CsCO<sub>3</sub> (12.84 g, 39.41 mmol), DMF (26 mL), and chloroacetaldehyde dimethyl acetal (4.60 mL, 40.4 mmol) were added to a round bottom flask while stirring under N<sub>2</sub> atmosphere. The reaction mixture was heated to 120 °C for 16 h and left to cool at room temperature. The solids were filtered via vacuum filtration. The filtrate was concentrated in vacuo and purified by flash column chromatography (SiO<sub>2</sub>; 50–100% EtOAc/hexanes, 0–20% MeOH/CH<sub>2</sub>Cl<sub>2</sub>) to yield 4P as a solid (3.46 g, 79%). TLC (SiO<sub>2</sub>, 10% MeOH/CH<sub>2</sub>Cl<sub>2</sub>): R<sub>f</sub> = 0.43. <sup>1</sup>H NMR (CDCl<sub>3</sub>, δ, ppm): 7.26 (d, *J* = 7.4 Hz, 2 H), 6.20 (d, *J* = 7.3 Hz, 2 H), 4.35 (t, *J* = 4.7 Hz, 1 H), 3.75 (d, *J* = 4.8 Hz, 2 H), 3.28 (s, 6H).

**A2.2.3 Electrochemical Characterization.** An electrochemical workstation (CH Instruments, CHI660E) was utilized to perform cyclic voltammetry sweeps for the various substrates dispersed in 0.5 M HCl. A conventional electrochemical H-cell was utilized in a three-electrode configuration. A templated graphite electrode and a Hg/HgSO<sub>4</sub> (Sat. Na<sub>2</sub>SO<sub>4</sub>) electrodes were utilized as the working and reference electrodes, respectively. To template the graphite rectangular electrodes (IKA), epoxy (Hysol 9462) was applied with care taken to leave an exposed active surface area of 0.510 cm<sup>2</sup>. Pt wire was utilized as the counter electrode. The anodic side of the H-cell contained the working and reference electrodes while the counter was located on the cathodic side of the H-cell. The electrodes were cleaned before each trial utilizing an electrode polishing kit (CH Instruments). The cleaning of the electrodes was performed between each

experiment to refresh the surface of the electrodes. Cyclic voltammetry was performed under stirring (500 rpm) at room temperature.

**A2.2.4 Simple Electrochemical Chlorination H-Cell.** A two-electrode configuration in a conventional electrochemical H-cell (Pine Instruments) attached to a DC Power Supply (Tektronix, PWS4305) was utilized for all electrochemical conversions (Figure A2.1A). Templated graphite electrodes were utilized as an anode in the oxidative compartment of the H-cell for all experiments. The electrodes were cleaned following the method above to remove accumulated products and to refresh the surface of the electrodes between experiments. A platinum (Pt, CH Instruments) wire counter electrode was implemented for the cathode (ca. 0.013 cm<sup>2</sup>). The electrolyte utilized was either 0.5 M HCl or 0.1 M KOH, with 20–30 mL contained within each compartment of the H-cell. Varying concentrations of the organic substrates were added to the anodic chamber (table 1). A set potential of 2.5–10 V was applied to the H-cell for 2–60 min under continuous stirring (500 RPM). Depending on the characterization technique, independent experiments or sub-sampling was utilized per time. Sub-sampling occurred at a given time interval (0.5–10 min) where 200  $\mu$ L of electrolyte was sampled during electrochemical conversion. Temperature dependent experiments for 2MP were conducted in an ice- (0 °C) or water-bath (50 °C) at 2.5 V for 10–30 min.

**Table A2.1** Table of experimental concentrations for the various substrates with applied potentials over the time performed.

| H-Cell |   | 0.5 M HCl   |               |            |  |
|--------|---|-------------|---------------|------------|--|
| Sub.   | Conc. (mM)  | Volume (mL) | Potential (V) | Time (min) |  |
| 2MP    | 20 $\mu$ L Substrate Directly Suspended in 1 mL DCM |             |               |            |  |
| 2MP    | 10.0  | 20.0        | 2.5           | 20.0       |  |
| 2MP    | 10.0  | 20.0        | 2.5           | 30.0       |  |
| 2MP    | 10.0  | 20.0        | 2.5           | 40.0       |  |
| 2MP    | 10.0  | 20.0        | 3.0           | 3.0        |  |
| 2MP    | 10.0  | 20.0        | 4.0           | 9.0        |  |
| 4P     | 16.6 mg Substrate Directly Suspended in 1 mL DCM    |             |               |            |  |
| 4P     | 3.8   | 20.0        | 3.5           | 3.0        |  |
| 4P     | 7.1   | 20.0        | 6.0           | 60.0       |  |
| 4P     | 7.5   | 20.0        | 7.5           | 60.0       |  |
| 4P     | 7.7   | 20.0        | 10.0          | 10.0       |  |
| XCA    | 1.34  | 30          | 6.0           | 60.0       |  |

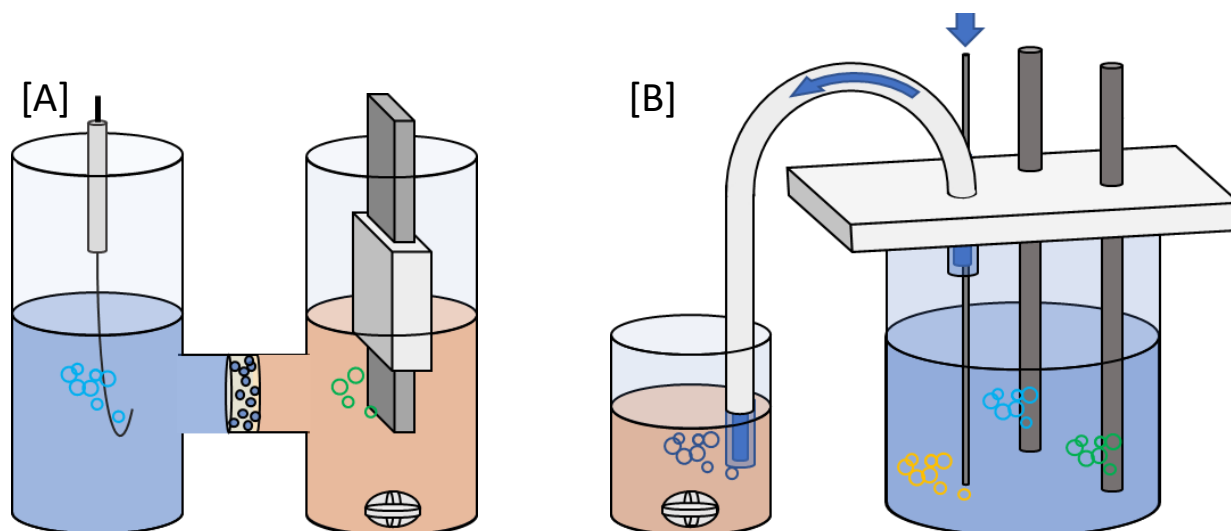
  

| Gas Cell |            | 0.5 M HCl      |             |               |            |
|----------|------------|----------------|-------------|---------------|------------|
| Sub.     | Conc. (mM) | Sub. Cell (mL) | E-Cell (mL) | Potential (V) | Time (min) |
| 2MP      | 10.0       | 20.0           | 40.0        | 4.0           | 20.0       |
| 4P       | 4.0        | 20.0           | 40.0        | 4.0           | 10.0       |

**A2.2.5 Electrochemically-Generated Chlorine Gas Facilitated Cell.** Non-electrochemical conversion of the substrates via an electrochemically-generated chlorine gas cell was explored. An electrochemically-generated chlorine gas cell was fabricated where the organic substrates were dispersed in a solution located separate from the electrochemical cell, connected

via FEP tubing (Figure A2.1B). The tubing allowed for gas to be bubbled from the chlorine generation cell. The electrochemical chlorine gas cell was constructed from a 50 mL borosilicate beaker capped with a piece of acrylic sealed and coated with epoxy (Hysol 9462). Two graphite rods (Alfa Aesar) extended through the lid and were fixed into place with epoxy. The graphite rods extended into the 0.5 M HCl electrolyte (ca. 3.11 cm<sup>2</sup> each) and allowed for contacts to connect to the power supply. The chlorine gas cell was filled with 0.5 M HCl (ca. 40 mL). A separate port in the cell was utilized for the simultaneous injection and removal of N<sub>2</sub> gas and electrochemically-generated gases, respectively. A potential of 4.0 V was applied from 10–20 min. Under operation, the chlorine-rich stream flowed through the FEP tubing and was bubbled in the separate 50 mL cell containing a substrate dispersed in 20 mL of 0.5 M HCl.





**Figure A2.1** A visual depiction of a [A] simple electrochemical H-cell and [B] fashioned gas-generating electrochemical cell, utilized to chlorinate organic substrates dispersed in 0.5 M HCl (orange). The blue represents 0.5 M HCl without any organic substrate. Gas generation is depicted by bubbles: chlorine (green), hydrogen (light blue), nitrogen (yellow), and the mixture of gases (dark blue).

**A2.2.6 GC-MS Analysis and LLE Substrate Isolation.** Gas chromatography mass spectrometry (GC-MS) was collected on a Hewlett Packard Agilent 6890 series G1530A GC with an Agilent Technologies column (19091S-433, HP-5MS, 0.25 Micron, 30 m x 0.250 mm) fed into a Hewlett Packard Agilent G1098A MSD. The GC-MS was not compatible with acidic media and therefore a liquid-liquid extraction (LLE) was performed. Electrolyte containing post-conversion organic substrates was added to a separatory funnel and extracted with two portions of DCM (20 mL total). The post extraction DCM was combined and concentrated to 1–2 mL utilizing a modified rotary evaporator. The concentrated solutions were passed through a 0.2  $\mu\text{m}$  syringe filter (MDI) and then analyzed via manual injection (1  $\mu\text{L}$ ). A GC heating protocol was developed as

follows: 1) 31.5 °C/min to 200 °C held for 2.57 min, 2) 30 °C/min to 250 °C held for 5.00 min, 3) 30 °C/min to 300 °C held for 5.00 min, and 4) 30 °C/min to 320 °C. All post-conversion electrolytes containing organic substrates were analyzed on GC-MS.

**A2.2.7 NMR and TLC Plate Isolation.** Proton nuclear magnetic resonance ( $^1\text{H}$  NMR) spectra and proton-decoupled carbon nuclear magnetic resonance ( $^{13}\text{C}$  NMR) spectra were recorded on a Bruker 600 MHz spectrometer. To perform the  $^1\text{H}$  NMR analysis, the electrochemical conversion products were separated by prep-TLC. Electrolytes containing multiple conversion products were placed on silica coated TLC plates. An eluting solvent of DCM and Ethyl Acetate (4:1, respectively) was utilized and the plate was viewed under UV light (254 nm) to identify the elution bands. The desired band was isolated and analyzed by NMR in  $\text{CDCl}_3$ . Proton resonances are referenced to residual protium in the NMR solvent. Carbon resonances are referenced to the carbon resonances of the NMR solvent. Data are represented as follows: all chemical shifts ( $\delta$ ) in parts per million (ppm), multiplicity (br = broad, s = singlet, d = doublet, t = triplet, q = quartet, m = multiplet, o = overlap), coupling constants ( $J$ ) in Hertz (Hz), integration.

**A2.2.8 LC-MS Analysis.** Liquid chromatography mass spectrometry (LC-MS) was recorded on an Agilent 6135 single quad (LCMS-ESI) with a Phenomenex Gemini C18 110Å LC column (50 x 3 mm). An LC-MS gradient of 95:5-5:95  $\text{H}_2\text{O}$  with 0.1% formic acid/acetonitrile was utilized.

## A2.3 RESULTS AND DISCUSSION

### A2.3.1 Substrate Selection, System Constraints and Characterization

To chlorinate heterocyclic pyridone-based substrates, a direct electrochemical-conversion method was developed. Each chlorination experiment was carried out in aqueous hydrochloric acid (0.5 M HCl). Under electrochemical conditions, HCl has been reported to act as an electrolyte and chlorine donor for similar systems. [1] Specific pyridone-based substrates were selected owing to specific functional groups attached to the heterocyclic ring. Electrochemical conversion conditions were modified for each substrate to obtain varying degrees of chlorination. To the best of our knowledge, the functionalization of carbonyl-type heterocyclic substrates is not readily reported.

N-methyl-2-pyridone (2MP, compound A), 1-(2,2-dimethoxyethyl)-4(1*H*)-pyridinone (4P, compound B), and 1,6-dimethyl-4-oxo-1,4-dihydropyridine-3-carboxylic acid (XCA, compound C) were selected for unique functional groups and possible resemblance of constituents in active ingredients and other biological molecules (Figure A2.2). Furthermore, the assortment of functional groups located on the pyridone-ring of the three substrates was expected to affect the reactivity of each molecule. To avoid the influence of nitrogen-based reactions, the substrates listed were previously N-methylated, or equivalent, increasing substrate stability and preventing Lewis acid formations. Compound A presents a simple molecule with functional groups limited to a carbonyl and methylated hetero-atom on the cyclic carbon ring. Compound B was synthesized from 1,4-dihydro-4-pyridone to add an acetaldehyde group to the N-heteroatom. Compound C was the most functionalized, with additional methyl and carboxylic acid groups present. The carbonyl group on the heterocyclic-substrates adds electronegativity and polarity, aiding the formation of

resonance structures. The resonance structures originating about the carbonyl allow for both ortho- and para- additions. However, the para- position is blocked by a heteroatom located on compound B and C allowing only for ortho-additions. Compound A exhibits the greatest number of cyclic atoms unblocked by constituents and therefore allows for the greatest number of chemical additions and configurations. Post-conversion, the chemical structures of proposed reactants and products are shown in Figure A2.2, exhibiting mono- and di-chloro- products.

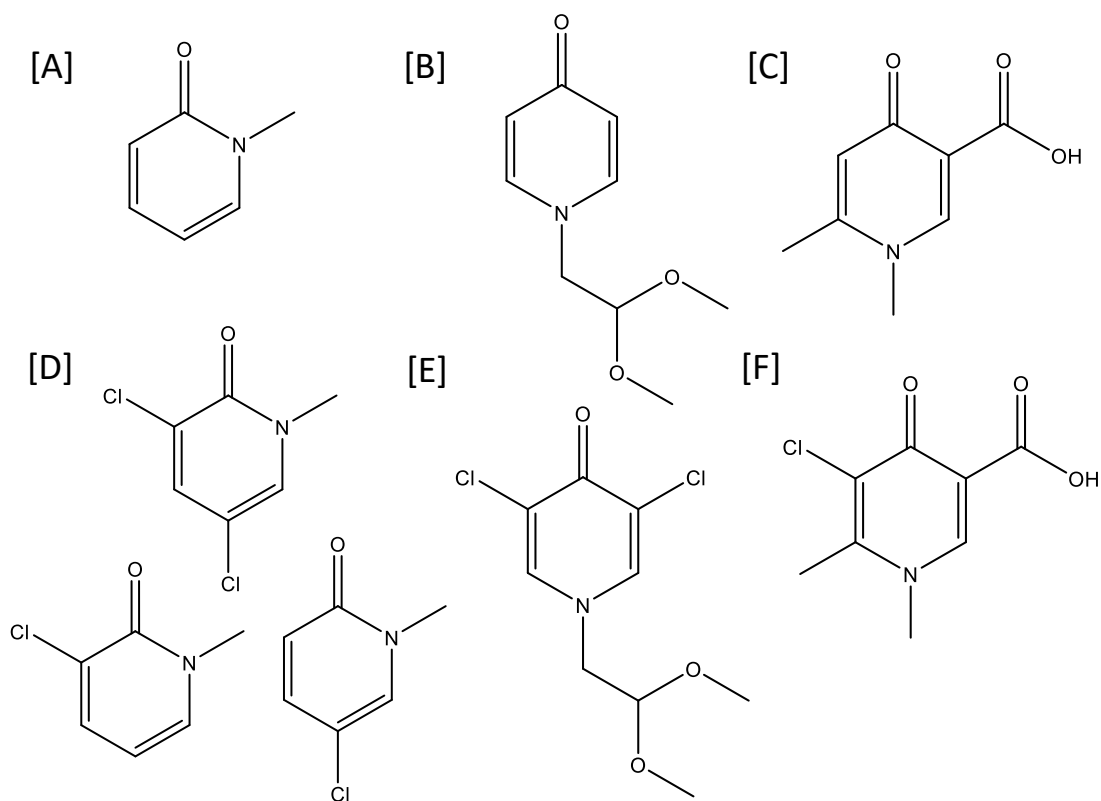


**Figure A2.2** The chemical structures for the [A-C] heterocyclic substrates and [D-F] major chlorinated products: [A] n-methyl-2-pyridone, [B] 1-(2,2-dimethoxyethyl)-4(1*H*)-pyridinone, [C] 1,6-dimethyl-1,4-oxo-1,4-dihydropyridine-3-carboxylic acid, [D] 3-chloro-1-methyl-2(1*H*)-pyridone, 5-chloro-1-methyl-2(1*H*)-pyridone, and 3,5-dichloro-1-methyl-2(1*H*)-pyridone; [E] 3,5-dichloro-1-(2,2-dimethoxyethyl)-4(1*H*)-pyridinone; and [F] 5-chloro-1,6-dimethyl-4-oxo-1,4-dihydropyridine-3-carboxylic acid.

To characterize the starting material (SM, compounds A–C) and chlorinated-products of the substrates (compounds D–F), the organic compounds were separated from aqueous electrolyte via a liquid-liquid extraction (LLE) and were analyzed using GC-MS. With greater than 10 mM initial concentrations of compound A, the SM was not fully extracted from the aqueous layer. Therefore, 10 mM or less were utilized throughout. Compound B was not readily extracted from aqueous

solution regardless of initial concentration. Therefore, quantification of compound B via GC-MS was not reported. However, GC-MS confirmed that the chlorinated products for compound B were extracted and observed. To confirm the GC elution peaks for compounds A and B, the substrates were directly dispersed in dichloromethane (DCM) and analyzed. The polarity and the degree of functionalization affected the solubility of molecules in DCM. The solubility of the compounds in DCM was observed to increase after conversion owing to the addition of an extra chlorine atom. Furthermore, the carboxylic acid functional group of both chlorinated and non-chlorinated XCA substrates prevented dissolution into carrier solvents. Therefore, compound C was not analyzed via GC-MS.

A temperature ramping protocol was utilized with three steps holding at 200, 250 and 300 °C to yield sharp elution peaks for the GC-MS chromatographs. Peaks were determined for the SM of compounds A and B at 5.12 and 9.80 min, respectively. The MS spectra was utilized to provide quantification to the number of chlorine additions. For example, the peaks at 5.77 and 6.23 min gave a mass of 143  $m/z$ , a difference of one chlorine atom from the 5.12 min compound. The dichlorination product was observed at 6.80 min with 177  $m/z$ , indicating an addition of 68  $m/z$ . Chlorinated molecules were observed to exhibit MS characteristics specific for chlorine, representing the various isotopes of chlorine as additions of 35, 37, and 36  $m/z$ .<sup>88,89</sup>

To gain insight on the electrochemical activity of the substrates, cyclic voltammetry (CV) was utilized to measure the current evoked while sweeping voltage. A background CV was performed to understand the behavior of 0.5 M HCl electrolyte with a graphite working and Pt counter electrodes. Once the electrolyte background was plotted, compound A was added to form a 10 mM solution. Compound A was selected for its significant activation energy and number of addition sites available. A slight shift to more positive currents was observed for the cathodic potential

ranges after the addition of compound A (Figure A2.3). No significant peak was observed, indicating that 2MP is primarily electrochemically inert inside of the aqueous potential window. The tail of the CV at positive anodic voltages suggests that the potential window of the electrolyte was reached ca. 1.35 V vs. Hg/HgSO<sub>4</sub>. Most likely, indicating the start of the gaseous evolution reactions at the carbon electrode.<sup>90</sup> A slight decrease in current was observed with the addition of compound A at the anode, suggesting to slightly inhibiting the gaseous evolution reactions.

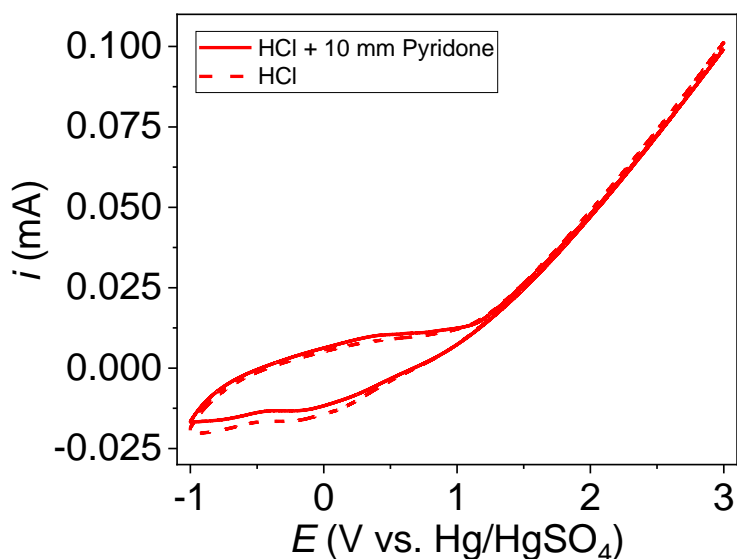


**Figure A2.3** Cyclic voltammogram for 0.5 M HCl with (solid) and without (dashed) 10 mM 2MP at 0.1 V/sec.

### A2.3.2 GC-MS Characterization Conversion for Compound A and B

The chlorine-evolution reaction (CER) has been performed electrochemically over the past decades at an industrial-scale, indicating the scalability of electrochemistry.<sup>90</sup> Large-scale electrochemical production can be correlated to the bench-scale utilizing an electrochemical H-

cell. Although H-cells are not implemented at the industrial-scale, they may be utilized to elucidate chemical reactions and mechanisms. Here HCl is used to facilitate both the CER ( $2\text{Cl}^- \rightarrow \text{Cl}_2 + 2\text{e}^-$ ,  $E^\circ = 1.359 \text{ V}$ ) and hydrogen evolution reaction (HER,  $2\text{H}^+ + 2\text{e}^- \rightarrow \text{H}_2$ ,  $E^\circ = 0.000 \text{ V}$ ).<sup>90</sup> Furthermore, traditional wet-chemical schemes would utilize halogenating agents, such as n-bromosuccinimide in place of HCl.<sup>91,92</sup>

A simple electrochemical H-cell was utilized with two compartments separated by a porous frit, preventing fast crossover and diffusion of reactants and products between chambers. Voltage ranges of 2.5–4.0, 3.5–10.0, and 2.5–6.0 V were applied to compounds A, B, and C, respectively. The voltage ranges were determined experimentally and to allow for adequate conversion to be observed over a reasonable time periods (2–60 min). SM conversion was determined based upon the MS peak area of the SM. The peak for compound A (5.12 min, GC) was observed to decrease proportionally with the peak formation of chlorinated products (Figure A2.4). Time was observed to affect the formation of products observed, chronologically forming mono- and then di-chloro-products. With enough time and at a voltage of 2.5 V or greater, compound A (10 mM) was able to reach near 100% conversion (Figure A2.4F). Therefore, selectivity between the mono- and di-chloro- products can be controlled by time and voltage if the products form at different times and energies. The 6.23 min mono-chloro- 2MP product may be observed to be converted to the di-product (Figure A2.4F).



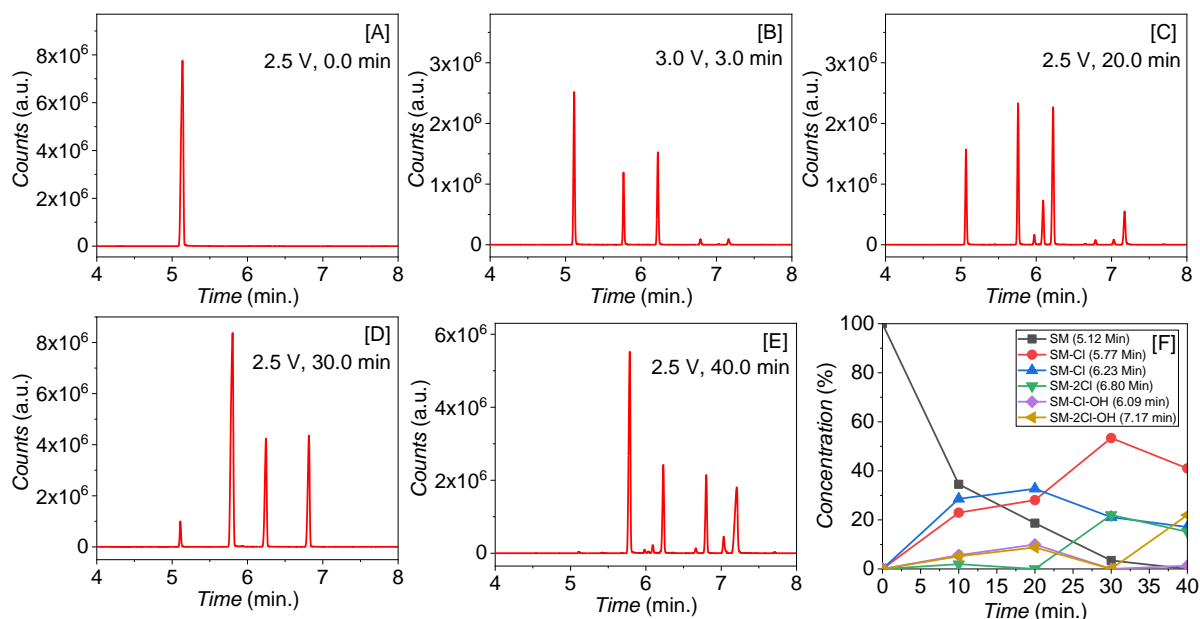


**Figure A2.4** [A-E] GC-MS chromatographs depicting the conversion of compound A to form chlorinated products over time (0—40 min) at 2.5—3.0 V. The SM (5.12 min) was observed to decrease over time forming major and minor products. [F] GC-MS peak area-based conversion for 2MP highlighting the major products. Each data point represents an independent experiment, i.e., no sub-sampling.

Compound B exhibited GC-MS chromatograph peaks at 9.80, 11.10, and 12.68 min post-conversion and LLE correlating to the SM (183  $m/z$ ), mono- (183 + 35 - 1 = 217  $m/z$ ), and di-chloro- (251  $m/z$ ) products, respectively. The peak at 9.80 min was observed with unproportionally low counts resulting from the LLE not sufficiently extracting compound B (SM). The 4P di-chloro-product was found as a major product at 12.65 min and 251  $m/z$ . A minor GC-MS peak was observed as a mono-chloro- product at 11.09 min (183 + 35 - 1 = 217), most likely present as an intermediate for the formation of the di-chloro-product. The applied voltages for all substrates did not yield significant selectivity between the formation of the mono-chlorinated

products, di-chlorinated products and chlorinated byproducts, indicating that the specific voltages for preferred reactions were not elucidated.

Chlorination products were found to be predominant thus far for the chlorination of both compounds A and B. However, minority peaks were occasionally observed and attributed to competing side reactions. The minority peaks for compound A, were located at 5.94, 6.09, 7.00, and 7.17 min corresponding to 161, 161, 195, and 195  $m/z$ , respectively. The mass charges of 161 and 195  $m/z$  were cross referenced against the molar masses of possible side reactions and were assumed to be mono-chloro- and di-chloro-mono-hydroxyl-products, respectively. However, NMRs were not performed to confirm this addition and therefore byproducts will be referred as a general term, “oxygenated”. The oxygenated additions were considered to be meta- additions with respect to the carbonyl, owing to that two peaks were observed for both the mono-chloro- and di-chloro-mono-oxygenated-products. It is notable that the mass charges do not identically match a straight forward oxygenated addition, i.e., for the di-chloro-  $177 + 17 - 1 \neq 195 m/z$ . It is speculated that the oxygenated addition can stabilize one of the chlorines to measure 35 and 37 for the di-chloro-product where only two of the four chlorine isotopes were observed for the 161 and 195  $m/z$  products. NMRs are necessary to determine the specific chemical structures, as there may be deviations in the instrumentation and analysis by GC-MS. Chromatographs displaying the peaks of interest with correlating MS spectra are represented in Figure A2.5.

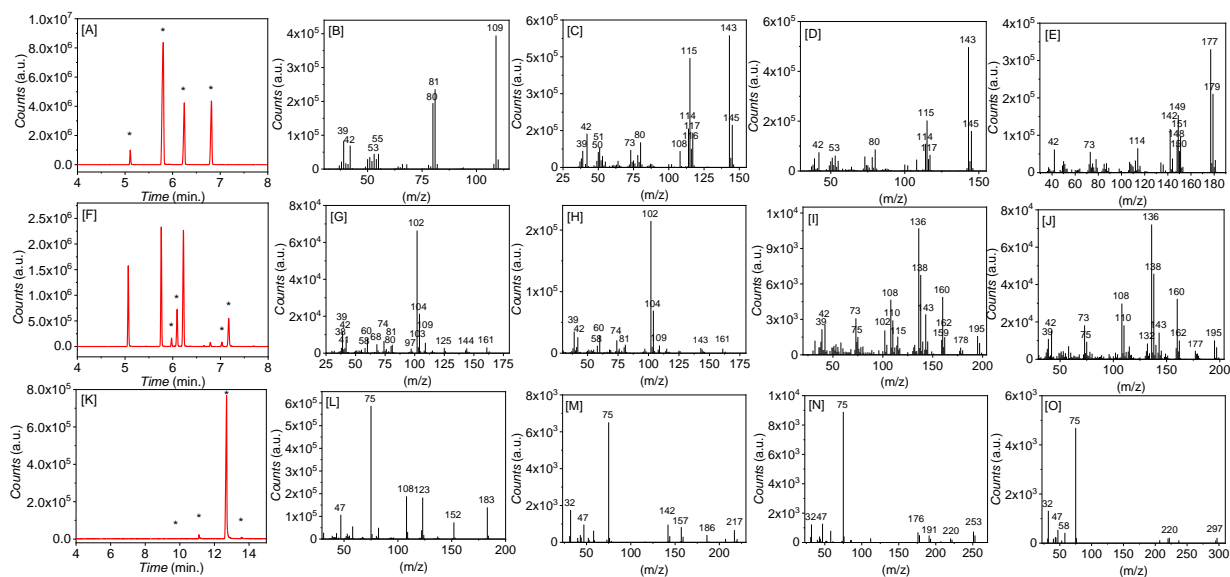


**Figure A2.5** Chromatograms for [A] compound A without byproducts, [F] compound A with byproducts and [K] compound B conversion products. MS spectra correlating to the observed chromatograph peaks of [B-E] 2MP (5.12 min, 109 m/z), 2MP-Cl (5.77 min, 143 m/z), 2MP-Cl' (6.23 min, 143 m/z), 2MP-2-Cl (6.80 min, 177 m/z); [G-J] 2MP-OH-Cl (5.94 min, 161 m/z), 2MP-OH-Cl' (6.09 min, 161 m/z), 2MP-2-Cl-OH (7.00 min, 195 m/z), 2MP-2-Cl-OH' (7.17 min, 195 m/z); [L-O] 4P (9.80 min, 183 m/z), 4P-Cl (11.10 min, 217 m/z), 4P-2-Cl (12.68 min, 253 m/z), and an unknown minor byproduct (13.55 min, 297 m/z), respectfully.

The observed mono-chloro- oxygenated-2MP products were hypothesized to be produced as an intermediate of the di-chloro-product formation and typically appeared as a minority product. Furthermore, it was observed that the chlorinated product has to form first to allow for the oxygenated- addition meta- to the carbonyl. The oxygenated- products were not observed as a predominant peak exceeding the formation of the chloro- products. The di-chloro-oxygenated-

products were present as an end product, mainly observed post-chlorination when the SM was exhausted by continual energy being supplied.

Furthermore, similar to the formation of the di-chloro-product, the di-chloro-mono-oxygenated-products were formed over time. Without the presence of chlorine in the electrolyte, no chemical additions were observed for 0.1 M KOH at similar voltages. A 102 m/z product was observed at 3.08 min but was not further investigated due to interest specifically for addition chemistries. Randomly assorted low (less than SM) molar masses were found to elute at short time scales on the GC-MS correlating to ring-opening/cleaving reactions in 0.5 M HCl at high voltages and long time, i.e., compound A at 10.0 V for 40 min.

### **A2.3.3 Gas Cell Experiments**

During the direct electrochemical synthesis reported above, a significant generation of gaseous products were observed. Therefore, an electrochemical cell was devised to evaluate the interactions of electrochemically-generated gaseous products with the organic substrates (Figure A2.1). The evolved gaseous products from HCl were carried by an inert gas to a separate cell containing a suspension of either compound A or B in solution (0.5 M HCl). By separating the substrates in a different cell, substrate-electrode interactions and reactive intermediate reactions were prevented. A constant generation of gaseous products was utilized by applying 4.0 V for 20 min, to correlate with the previous reactor scheme.

The gaseous cell resulted in similar addition reactions as the direct electrochemical method for compound A, where compound A was converted into both mono-chloro- products. A di-chloro-peak was detected at 6.78 min and was consider to be minimal compared to the direct method after

a 20 min conversion. However, the concentration of mono-chloro- products was significantly high with relatively small amounts of other products present, including the SM. Therefore, the gaseous cell for compound A was found to yield high conversion and selectivity for the mono-chloro-products with few byproducts after 20 min. Noteworthy, was that the oxygenated byproducts were still present on the GC-MS at 6.09 and 7.17 min, suggesting that the chlorination reaction initiates a consequential oxygenated reaction or that the competing oxygen evolution reaction (OER) products are also contributing in some way. It has been reported that the CER is in competition with the oxygen evolution reaction (OER,  $2\text{H}_2\text{O} \rightarrow \text{O}_2 + 4\text{H}^+ + 4\text{e}^-$ ,  $E^\circ = 1.229 \text{ V}$ ).

Compound B exhibited a different phenomenon in the gaseous cell, resulting in a messier conversion compared to the direct electrochemical method. Compound B already exhibited a messy chromatograph compared to A on GC-MS, owing to solubility issues. When reacting with the evolved gases, a large broad peak was observed on GC-MS at long elution times correlating to an assortment of molar masses 207–399 m/z, possibly correlating to polymerization products. The presence of hydrogen gas being bubbled in addition to the anodic formed gases may have aided in the formation of products present in this broad peak. It cannot be ruled out that the generation of chlorine gas plays a role in the chlorination of organic substrates giving similar GC-MS spectra peaks (Figure A2.6).

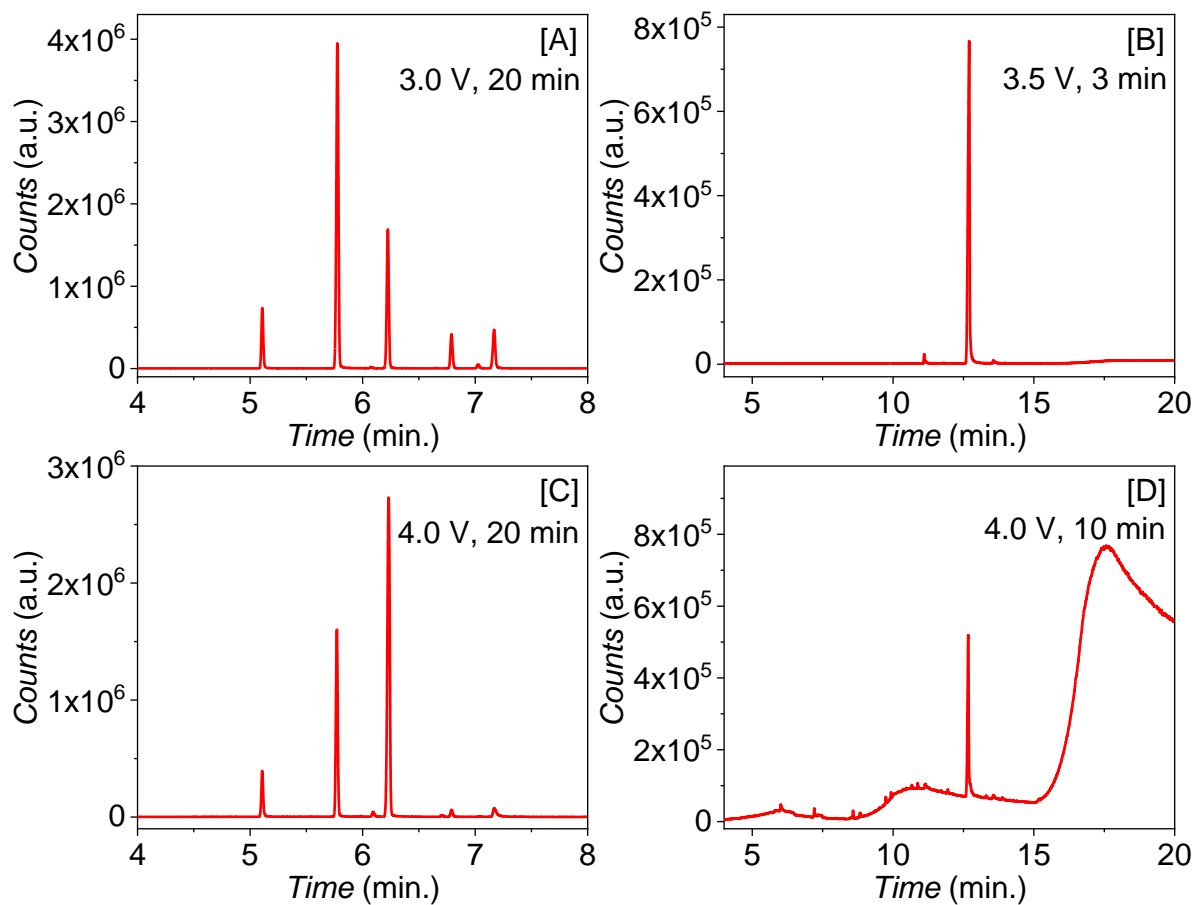


**Figure A2.6** GC chromatographs for the conversion of compounds A and B via an [A, B] H-cell and a [C, D] gaseous-cell, respectively.

### A2.3.4 LC-MS Characterization and Conversion Rates for Compounds A, B and C

LC-MS characterization was carried out for the conversion of compounds B and C. LC-MS was utilized to complement the reported GC-MS chromatographs without solubility constraints, owing to the robustness of the column and detector. Direct sampling of the electrolyte was utilized without introducing error from extraction procedures. A complete solvent system with SM and

products was analyzed to give accurate conversion efficiencies. Therefore, LC-MS data was collected for samples sub-sampled over time. When compared with the GC-MS chromatographs of compound B, conversion may not have proceeded as initially detected, where 2.5–3.5 V at 3 min previously gave near 100% conversion to di-chloro- product. No conversion was observed on LC-MS for compound B at 3–5 V for 5.0 min. However, 6.0 V and 7.5 V provided low conversion (15–32 %) to the di-chloro-4P product, even after 60 min (Figure A2.7). Increasing the applied voltage to 10 V, decreased the conversion time to just 10 min, reaching 91 % conversion for 28.18 mg of compound B, ~3 mg/min.

The conversion of compound C proceeded in 0.5 M HCl at an applied voltage of 6.0 V, sub-sampled over time. The area of the LC-MS peak at 1.723 min was utilized for the conversion measurement for XCA SM. The applied voltage of 6.0 V facilitated the conversion of compound C to the mono-chlorinated product observed with nearly 100% conversion efficiency after 30 min via LC-MS. The reaction of compound C was allowed for 60 min with no additional organic byproducts reported. Confirmation of a mono- chlorine addition to the ortho- position of XCA was observed via LC-MS and <sup>1</sup>NMR. 3,5-dichloro-1-(2,2-dimethoxyethyl)-4(1*H*)-pyridinone and 5-chloro-1,6-dimethyl-4-oxo-1,4-dihydropyridine-3-carboxylic acid are currently unavailable commercially and were not found in a SciFinder publication search.

LC-MS was able to detect conversion products for compound A isolated with a prep-TLC plate method. Compound A displayed a 1.647 min peak with 111.1 and 110.1 *m/z* corresponding to the molecular mass of 109 g/mol (SM). Compound A mono-chloro-products correlating to 5-chloro-2MP and 3-chloro-2MP were observed at 3.927 and 2.948, respectively, with 145.1 and 144.1 *m/z* observed for both samples. The 3,5-chloro-2MP was observed at 6.007 min with 179.1 and 180.0 *m/z*. A dichloro-2MP-byproduct was observed at 6.010 min with 181.0, 180.0, and 199.9

$m/z$  predominant MS peaks. The 181.0 and 180.0  $m/z$  correlate to the di-chloro-product, whereas 199.9  $m/z$  correlates with a speculated a di-chloro- oxygenated- product.

The conversion voltages for compound A were significantly lower than B and C. Conversion at 2.5–3.0 V gave nearly 100 % conversion for compound A after 40 min, based upon the remaining % SM on GC-MS. The rate of formation was loosely fitted for each substrate. The data presented over time for compound A displays an exponential decay of A over time. This can be attributed to the mono- products forming the sequential products over time. Compounds B and C exhibited a linear behavior, attributed to the relatively direct formation of conversion products (Figure A2.7). Compound C was thought and found to be more reactive than B, owing to the additional functional groups present, decreasing the activation energy of the  $sp^2$  carbon sites. Compound A was studied at low (0 °C) and high (50 °C) temperatures at 2.5 V over time. The high temperature reaction exhibited an expected behavior, which facilitate the conversion quickly giving an onset formation of di-chloro-products faster than at higher voltages. The di-chloro- and di-chloro- oxygenated-products were the predominant peaks observed after 30 min. The low temperature reaction displayed a slightly unexpected result where conversion was higher than anticipated, attributed to Henry's constant correlating to a higher retention of the chlorine gas products in solution allowing for more reactions.



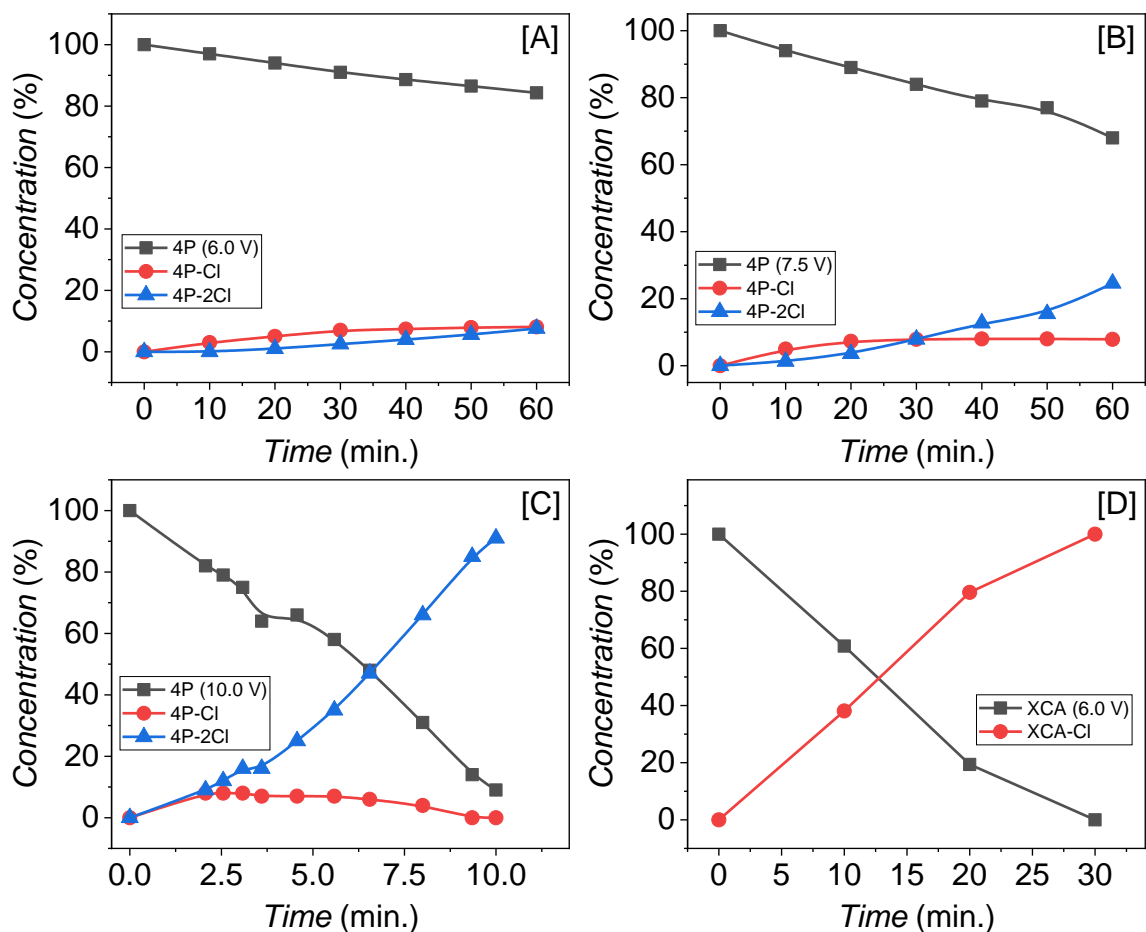


**Figure A2.7** Conversion of compound B in 0.5 M HCl at [A] 6.0V (25.99 mg), [B] 7.5V (27.53 mg), and [C] 10.0V (28.18 mg). Conversion of 1,6-dimethyl-4-oxo-1,4-dihydropyridine-3-carboxylic acid (compound C) at [D] 6.0V (6.72 mg). Data was collected from the peak areas found on LC-MS without an extraction procedure, all results are shown as %SM.

<sup>1</sup>H-NMR confirmed the location and addition of chlorine after conversion. TLC plate extractions were utilized to isolate chlorination products found to have high conversion on GC-MS. The TLC eluting solvent was assumed to have similar product separation compared to the GC-MS chromatographs. Therefore, the 2MP chloro-products observed on GC-MS at 5.12, 5.77,

6.23, and 6.80 min were correlated to TLC plate *R<sub>f</sub>* values of 0.087, 0.130, 0.196, and 0.362, respectively. The 2MP GC-MS chromatograph peaks at 5.12, 5.77, 6.23, and 6.80 min were found to be 2MP, 5-chloro-2MP, 3-chloro-2MP, and 3,5-chloro-2MP, respectively. As expected, the 4P and XCA substrates were confirmed to exhibit ortho- additions about the carbonyl. No byproducts were analyzed via NMR. Impurities were not isolated or characterized by NMR to reveal the chemical structures. <sup>13</sup>C NMR was only performed to verify the 4-pyridone synthesis as a SM. <sup>13</sup>C NMR was not performed for the chlorination products.

### **A2.3.5 Limitations of this work**

Without the high concentration experiment, enough evidence was found to indicate that the byproducts produced were oxygenate pyridone-based derivatives, from comparing the gas and direct experiments. However, a gap in the experimental work is the full product confirmation and scalability. A TLC extraction for carbon and hydrogen NMR characterization from an experiment with a high initial substrate concentration (200 mM) and long run time could fill any remaining gaps in the analysis section by confirming the identity of all synthesized, intermediates, products and byproducts. Furthermore, isolated yields are necessary to compare to the conversion efficiencies to the traditional wet-chemical schemes.

## **A2.4 CONCLUSION**

Anodic electrochemical reactions can open the possibility of alternate pharmaceutical synthesis schemes. Halogenated organic precursors/intermediates were successfully synthesized

via an electrochemical chlorination method. The chlorination of n-methyl-2-pyridone (2MP, compound A), 1-(2,2-dimethoxyethyl)-4(1*H*)-pyridinone (4P, compound B), and 1,6-dimethyl-4-oxo-1,4-dihydropyridine-3-carboxylic acid (XCA, compound C) substrates have been developed and verified by GC-MS, <sup>1</sup>H-NMR, and LC-MS. The chlorine addition was observed to preferentially bind ortho- and para- to the carbonyl, indicating that the carbonyl group was necessary in activating the cyclic-ring. Furthermore, oxygenated- byproducts were observed after the chlorination reactions for compound A. An electrochemical gas evolution cell was developed and utilized to understand the role of gaseous products in the conversion process. The gaseous products (chlorine and oxygen gas) were found to aid and facilitate conversion independently. However, the gaseous cell had mixed results, producing only mono-products for compound A and random products for compound B. The observation of an oxygenated- byproduct during the gaseous experiment for compound A, further indication that competing gas evolution reaction are occurring in the electrolyte. Applied voltage and time were evaluated to tune a high conversion to chlorinated products. Compound A formed mono- and a di-chloro- products in various ratios for given time periods under applied potentials. Compound B formed 3,5-dichloro-1-(2,2-dimethoxyethyl)-4(1*H*)-pyridinone with 91 % conversion at 10.0 V in 10.0 min. Compound C formed 5-chloro-1,6-dimethyl-4-oxo-1,4-dihydropyridine-3-carboxylic acid with near 100 % conversion at 6.0 V after 30.0 min. Furthermore, a facile electrochemical method was readily utilized to chemically produce the di-chloro-4P and mono-chloro-XCA substrates for the first time, which are not commercially available or registered in journal articles on SciFinder.

## VITA

Dylan Daniel Rodene was born on July 11, 1992, in Grand Island, Nebraska, and is an American citizen. He graduated from Powhatan High School, Powhatan, Virginia in 2010. He received his Bachelor of Science with a double major in Chemical & Life Sciences Engineering and Chemistry from Virginia Commonwealth University 2014 and subsequently started graduate school.

## PUBLICATIONS

1. **DD Rodene**, EH Eladgham, RB Gupta, IU Arachchige, V Tallapally, Crystal Structure and Composition-Dependent Electrocatalytic Activity of Ni–Mo Nanoalloys for Water Splitting To Produce Hydrogen, *ACS Applied Energy Materials*, **2019**, 2, 7112-7120.
2. SK Saraswat, **DD Rodene**, RB Gupta, Recent advancements in semiconductor materials for photoelectrochemical water splitting for hydrogen production using visible light, *Renewable and Sustainable Energy Reviews*, 89, **2018**, 228-248.
3. E Nyankson, **D Rodene**, RB Gupta, Advancements in crude oil spill remediation research after the Deepwater Horizon oil spill, *Water, Air, & Soil Pollution*, 227 (1), **2015**, 29
4. Patent Application – IU Arachchige, RB Gupta, **DD Rodene**, EH Eladgham, Pure-Phase Cubic Ni<sub>1-x</sub>Mo<sub>x</sub> Alloy Nanoparticles as Low-Cost and Earth Abundant Electrocatalysts for Water Splitting to Produce Hydrogen, **2019**.
5. *Under Preparation* – Amr A. Hassan, Atanu Giri, **Dylan D. Rodene**, Ram B. Gupta, M. Samy El-Shall, Tailoring the Photocatalytic Activity of Cerium Oxide and Zinc Oxide Modified Graphitic Carbon Nitride Nano-Composites Towards Atrazine Degradation. *J. Nanoparticle Research*.
6. *Under Preparation* – Ebtessam H. Eladgham, **Dylan D. Rodene**, Ram B. Gupta, and Indika U. Arachchige. Stable and Efficient Electrocatalytic Hydrogen Production Cathodes: Phase, Morphology, and Composition Dependent NiMoP. *ACS Appl. Mater. & Inter.*
7. *Under Preparation* – Ahmed A. Abdelkader, Nazgol Norouzi, Ahmed Alzharani, Muslum Demir, **Dylan Rodene**, Kayesh M. Ashraf, Ram B. Gupta, Hani M. El-Kaderi Atomic Cobalt Catalysis in Nitrogen-Doped Porous Carbon in Advanced Lithium-Sulfur Batteries.

8. *Under Preparation* – Ahmed Alzharani, Ayyob Bakry, **Dylan Rodene**, Ram B. Gupta, Hani M. El-Kaderi, Azo-benzene Functionalized Graphene Oxide as a Cathode Material for Na Batteries.
9. *Under Preparation* – Ahmed A. Abdelkader, Ahmed Alzharani, **Dylan Rodene**, Nazgol Norouzi, Ram B. Gupta, Hani M. El-Kaderi, Synthesis of Ultrafine Cobalt Phosphide/Nitrogen Doped Carbon Composite as a Sulfur Host for Advanced Lithium Sulfur Batteries.
10. *Under Preparation* – **Dylan D. Rodene**, Matthew Glace, Jo-Ann Jee, Narendar Gade, Thomas Roper, Ram B. Gupta. Electrochemical-Controlled Chlorination of Heterocyclic Pyridone-Based Substrates with Investigation into Mechanism. *Ind. Eng. Chem. Res.*

## PRESENTATIONS

1. ECS – Presentation, Crystal Phase Dependence on HER Water Splitting Performance of Earth-Abundant Electrocatalysts, **DD Rodene**, EH Eladgham, I Arachchige, RB Gupta, Meeting Abstracts, **2019**, 1630-1630.
2. ISCAN – Poster, Crystal Phase Dependence on the Hydrogen Evolution Reaction (Water Splitting) Performance of Earth-Abundant Ni<sub>1-x</sub>Mo<sub>x</sub> Electrocatalysts., **Dylan D. Rodene**, Ebtessam H. Eladgham, Indika U. Arachchige, and, Ram B. Gupta.
3. ISCAN – Poster, Colloidal Synthesis of Efficient Binary Ni-Mo Nanoalloys Catalysts and their Phosphides for Electrochemical Hydrogen Evolution Reactions Ebtessam H. Eladgham, **Dylan D. Rodene**, Indika U. Arachchige, and, Ram B. Gupta.
4. ECS – Presentation, Binary and Ternary Earth-Abundant Transition Metal Phosphides As Electrocatalysts and Photocatalysts for Water Splitting, **DD Rodene**, SK Saraswat, V Tallapally, I Arachchige, RB Gupta, Meeting Abstracts, **2018**, 1546-1546.
5. AiChE – Presentation, Production of Value Added Co-Products from the Hydrothermal Liquefaction of Unhydrolyzed Solids, Vinod S Amar, Bharat Maddipudi, Anuj Thakkar, Katelyn Shell, **Dylan Rodene**, Tylor Westover, Sandeep Kumar, Ram B Gupta, Rajesh Shende. *AiChE Annual Meeting*, **2019**.

6. AiCHE – Presentation, Catalytic Hydrothermal Treatment (CHT) of Lignocellulosic Biomass Anuj Thakkar, Katelyn Shell, Martino Bertosin, **Dylan Rodene**, Vinod S. Amar, Bharat Maddipudi, Tylor Westover, Sandeep Kumar, Alberto Bertuccio, Ram B. Gupta and Rajesh Shende, *AiChE Annual Meeting*, **2019**.

## **PROPOSALS**

1. NSF Graduate Research Fellowship Program – **D Rodene**, R Gupta. Landfill Biogas to Jet Fuel, One Step Closer to Creating a Sustainable City. **2015**
2. Ph. D. Qualifier Examination – **D Rodene**. Self-Healing “Smart” Materials to Repair Microstructure Defects. **2015**
3. NSF Graduate Research Fellowship Program – **D Rodene**, R Gupta. Hydrogen Fuel from Sun and Water via Visible-light Photocatalysis. **2016**
4. Department of Energy Office of Science Graduate Student Research (SCGSR) Program – **D Rodene**, T Deutsch (NREL), R Gupta. Binary and Ternary Earth-Abundant Transition Metal Phosphide Electrocatalysts to Enhance Photoelectrodes for Water Splitting. **2017**
5. Ph. D. Dissertation Proposal – **D Rodene**, R Gupta. Nanostructured Earth-Abundant Metal Alloys for Electrochemical Catalysis. **2018**
6. ACS Initiative Proposal – Thomas D. Roper, Ram B. Gupta, Narendar Reddy Gade, Stanley E. Gilliland, **Dylan D. Rodene**, Jo-Ann Jee. Solid Supported Electrochemical Oxidative C-H Functionalization and C-C Bond Forming Reactions. **2017**
7. Department of Energy Office of Science Graduate Student Research (SCGSR) Program – **D Rodene**, T Deutsch (NREL), R Gupta. In-Situ Characterization of CO<sub>2</sub> Reduction Electrocatalysts in a Flow Electrolyzer. **2018**